Horizontal Non-Contact Slumping of Flat Glass

by

Edward Sung

B.S. Mechanical Engineering
Massachusetts Institute of Technology, 2011

Submitted to the Department of Mechanical Engineering
in Partial Fulfillment of the Requirements for the Degree of
Master of Science in Mechanical Engineering

at the

Massachusetts Institute of Technology

June 2013

Signature of Author.....
Department of Mechanical Engineering
May 7, 2013

Certified by.....
Mark Schattenburg
Senior Research Scientist
KAVLI Institute for Astrophysics and Space Research
Thesis Supervisor

Accepted by.....
David E. Hardt
Professor of Mechanical Engineering
Graduate Officer

Horizontal Non-Contact Slumping of Flat Glass

by

Edward Sung

Submitted to the Department of Mechanical Engineering
on June, 2013 in Partial Fulfillment of the
Requirements for the Degree of Master of Science in
Mechanical Engineering

ABSTRACT

This paper continues the work of M. Akilian and A. Husseini on developing a non-contact glass slumping/shaping process. The shift from vertical slumping to horizontal slumping is implemented and various technologies required for the horizontal slumping process are developed. In the horizontal slumping process, a thin sheet of glass is placed in between two horizontal ceramic air bearings with a bearing to glass gap of about 50 μm, and the assembly is heated up to 600°C. The glass is unconstrained in the horizontal plane and must be positioned without any solid contact.

Specifically, the technologies developed are: an optical distance sensor for positioning of the glass, glass position control via air bearing fluid shear force and tilt of device, and device mechanisms for operation in 600°C.

Glass was slumped horizontally with bearing-to-glass gaps of >50 μm, 36±2.5 μm, and 30.5±2.5 μm. The best flatness achieved was 6.7/3.6±0.5 μm for front/back of the glass sheet, with a gap of 36±2.5 μm.

It was discovered that 600°C is hotter than necessary and that 550°C is still too hot for optimal slumping conditions. In addition, an important shift is made from using an oven, which heats the entire device, to using in-line pipe heaters, which supply heated air. This allows for much quicker heating and cooling times, which decreases slumping time to less than 30 minutes (10 minutes heating, 5 minutes slumping, 10 minutes cooling).

Thesis Supervisor: Mark Schattenburg
Title: Senior Research Scientist at KAVLI Institute of Astrophysics and Science

ACKNOWLEDGEMENTS

Foremost, I would like to express my sincere gratitude to my research advisor Mark Schattenburg for giving me an opportunity at an awesome project. His knowledge is quite astounding, as is his motivation and enthusiasm towards research. For someone like myself who has a bunch of hands-on experience but not nearly enough knowledge, I could not have had a better advisor and mentor for my graduate studies.

I would like to thank my academic advisor, Prof. Sang-Gook Kim, for his encouragement and insightful comments. Every discussion I've had with him has given me much food for thought. It has been a pleasure to be privy to his thoughts and views on the engineering sector.

I would like to thank my research group – Ralf Heilmann, Jay Fucetola, and Brandon Chalifoux. Thanks, Ralf, for your weekly input, for brainstorming with us, and for proofreading everything I write. Thanks, Jay, for your controls help and sharing enthusiasm about my project. Thanks, Brandon, for taking over the Shack-Hartmann when you did. I wouldn't have been able to complete my research without it.

Also, thanks goes to the MIT Kavli Institute staff for their administrative help. Our research wouldn't go as smoothly without their work. Jean, thanks for expertly dealing with some of those companies with me.

Thanks to Mark Belanger of the Edgerton machine shop for putting up with me and giving help while I filled up his shop with fumes (not really) from endless hours of machining stainless steel.

Funding from NASA has made this thesis possible.

CONTENTS

FIGURES

TABLES

CHAPTER

1

INTRODUCTION

This paper continues the work of Mireille Akilian [1] and Abdul Husseini [2], who did their doctoral and masters work, respectively, at the Space Nanotechnology Lab at the Massachusetts Institute of Technology. Their theses detail the initial development of a novel non-contact glass slumping technology, the purpose of which is to manufacture precision thin optics for x-ray telescopes.

1.1 Motivation and Purpose

X-rays must be reflected at low incidence angles (less than 5^{o}) in order to avoid photoelectric absorption. X-ray telescopes focus x-rays by using nested shells of first parabolic mirrors and then hyperbolic mirrors as is shown in Figure 1.1. The total number of mirrors is in the thousands, so the mirrors must be thin and light, and able to be manufactured quickly and cheaply.

Thin optics can be ground to a uniform thickness, but cannot be ground to a precise shape. A warped glass will deform to become flat during the grinding process, but will spring back into the warped shape when pressure is removed. Thermal shaping processes must be used to relax the internal stresses of the glass.

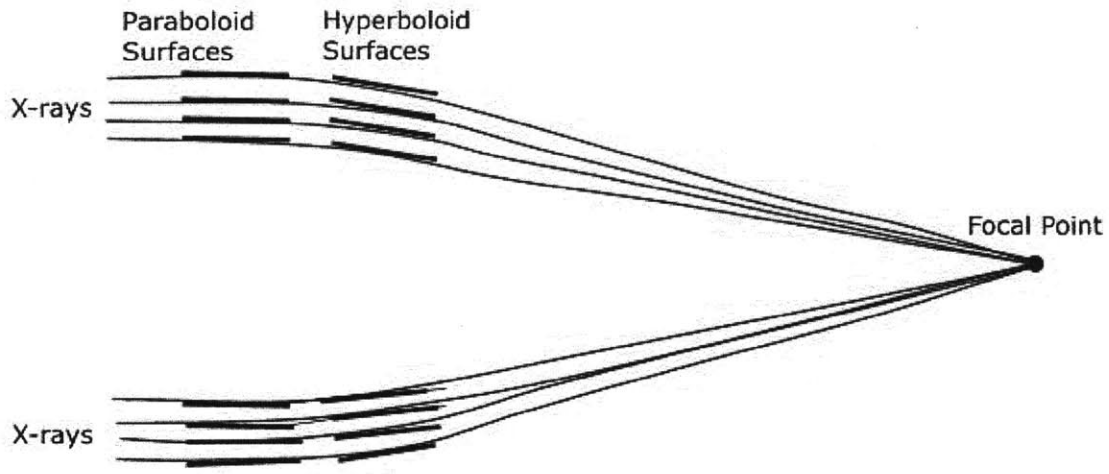

Figure 1.1: Schematic of x-ray telescope mirrors in Wolter-1 configuration [3].

1.2 Slumping Methods

The Goddard Space Flight Center uses a conventional slumping process where a thin glass sheet is balanced on top of a half-cylindrical mandrel inside of an oven. The oven is heated up to above the transformation temperature of the glass, which is around 600°C. This allows the glass to relax and take the shape of the mandrel, as is illustrated in Figure 1.2. The oven must then be cooled very slowly before the glass can be removed. If the oven is not cooled very slowly, then a thermal gradient will form across the thickness of the glass, which, in combination with the mismatch of CTE's of the mandrel and glass, will result in distortions in the glass. GSFC's slumping cycles therefore take several days, which is a large limitation on the mass production of x-ray telescope mirrors. [4][5]

Without any improvements, the conventional slumping process also runs into the problem with dust particles being caught in between the glass and the mandrel. Dust particles create mid-frequency spatial errors, which are visible as ripples on the surface of the glass on the order of millimeters. The dust can be eliminated through cleansing of the mandrel and glass and control of air quality, but results in the contacting surfaces fusing together. It is observed that dust particles aid in preventing stiction and allow for easy removal of glass from mandrel [6].

One method to get around the issue of dust particles is to use a multistep process in which the glass is slumped normally without removal of dust particles. Then the mandrel is coated with a bilayer consisting of first gold and then epoxy. The epoxy conforms to the gold and the glass with its high spatial frequency errors. After curing, the assembly is pulled off the mandrel. However, this method creates two major additional problems. One issue is the shrinkage of epoxy as it cures. The second issue is the mismatch in CTE's of all three materials. Either causes stresses which result in the glass warping. [7]

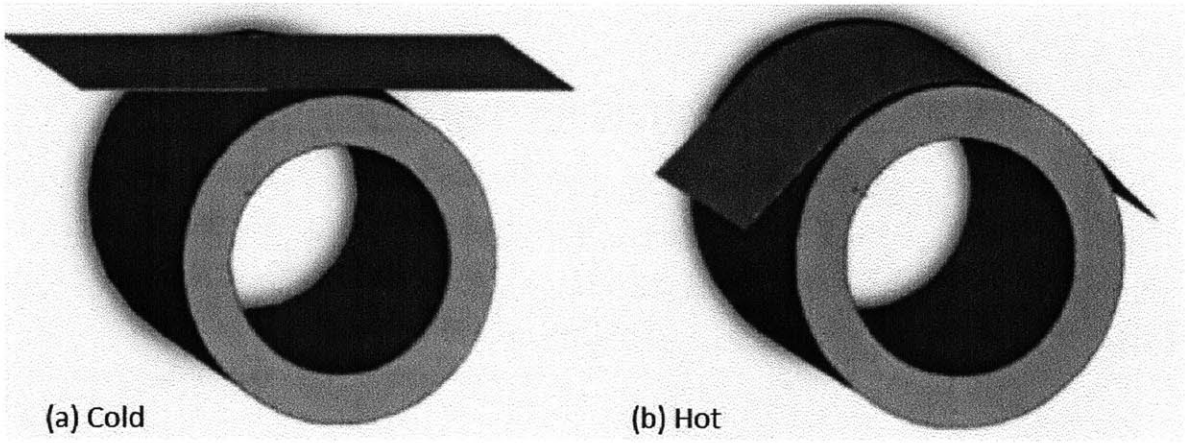

Figure 1.2: Solid mandrel slumping [3].

The widely used approach is to apply a non-stick coating onto the mandrel after removal of dust particles. GSFC uses a boron nitride slurry to coat their mandrels. The coating must be made as uniform as possible, which is a non-trivial process. The coating can have non-uniform mixtures of micro-particles and larger contaminant particles. Additionally, the boron nitride tends to clump and results in non-uniform layers. Slumped optics exhibit mid spatial frequency dimples and valleys [3]. Figure 1.3 illustrates the problems generally run into with mandrels.

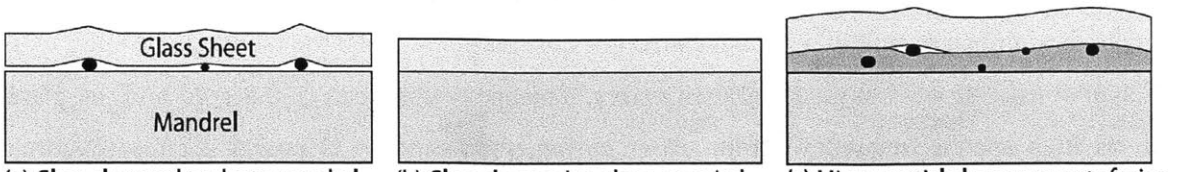

(a) Glass slumped to dusty mandrel results in surface errors but fusion is prevented.

(b) Glass slumped to clean mandrel results in fusion.

(c) Micro-particle layer prevents fusion but results in surface errors

Figure 1.3: Common issues with solid mandrel slumping [2].

1.3 Proposed Technology and Progress

In order to avoid the issues of cooling and dust particles, it was proposed that the glass sheets be shaped using air bearings as mandrels. The glass would be sandwiched in between two ceramic air bearings with a gap of 40 μm in between glass and each bearing. The pressure in the gaps would push the glass flat while the assembly is heated up to 600°C.

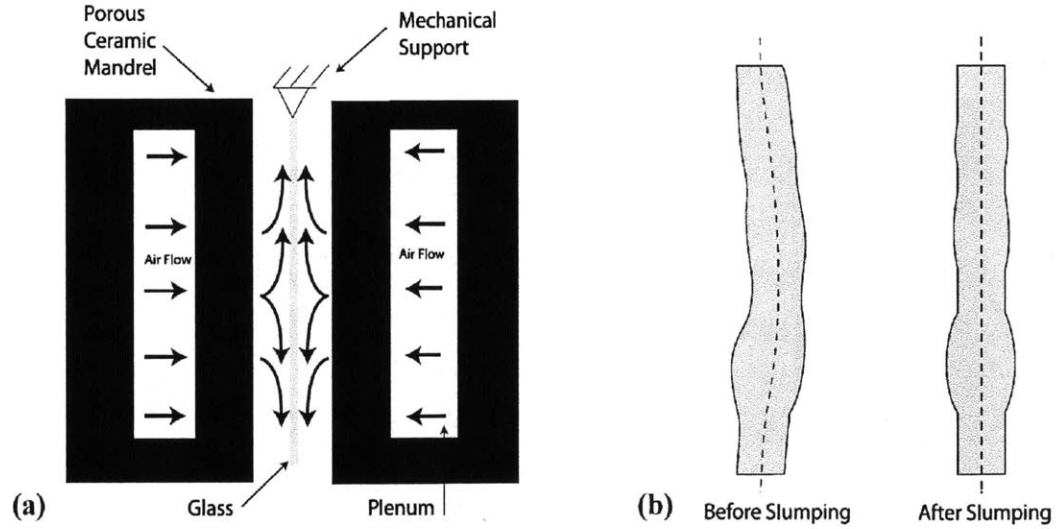

Figure 1.4: (a) Glass sheet with thickness variation in between two air bearings. (b) Glass sheet before and after thermal cycling. [2]

It should be noted that this process places an additional requirement on the thickness variation of the glass. Using a conventional mandrel does not require uniformity in thickness, but the process of using two air bearings on either side of the glass sheet will result in flatness errors of half the variation in thickness. This occurrence is illustrated in Figure 1.4. Glass sheets to be slumped must therefore first be polished to have a low thickness variation.

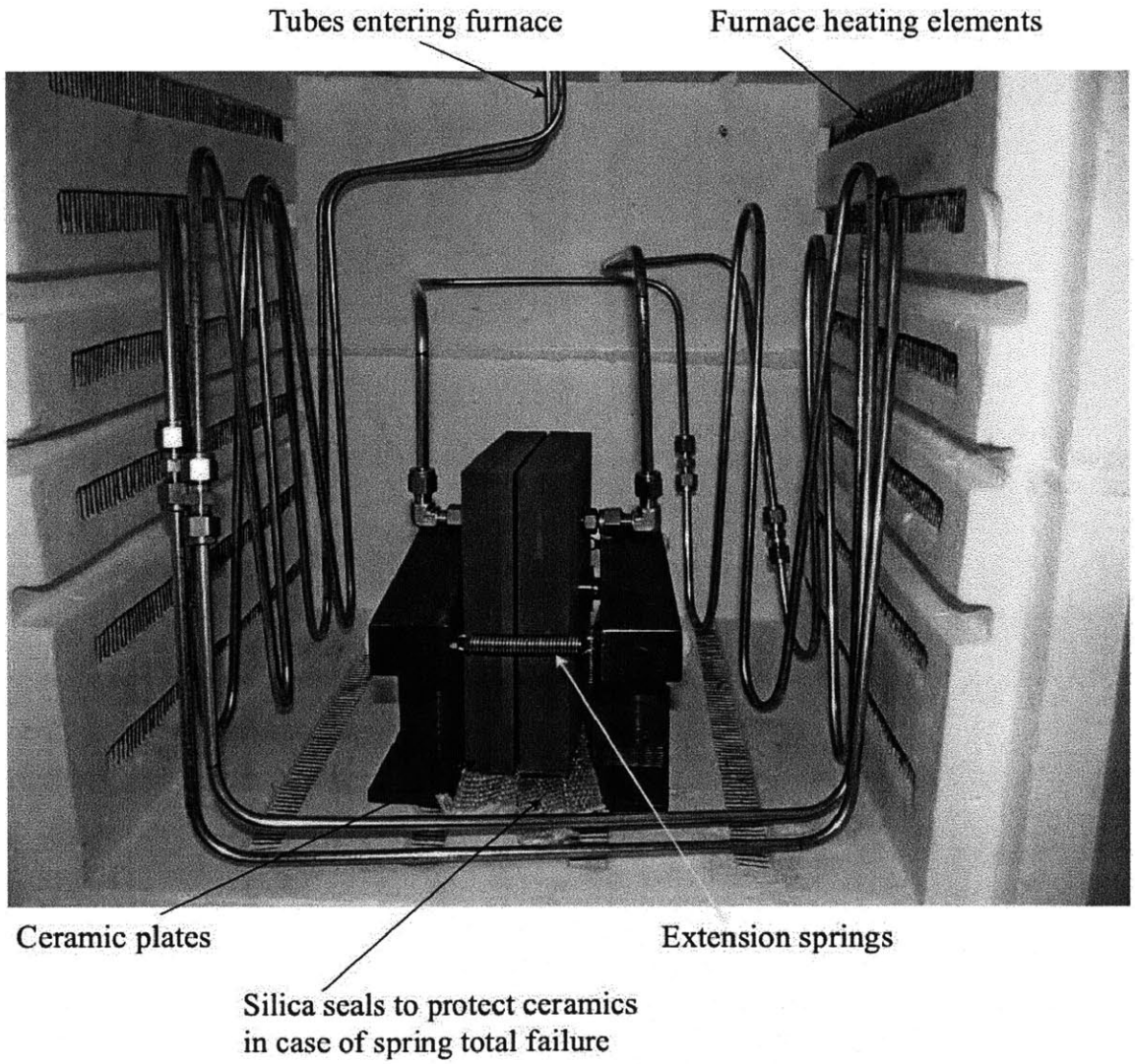

Figure 1.5: Device created by Akilian [1].

Although paraboloid and hyperboloid mirrors are the end goal, it was decided to pursue flat glass as a proof of concept and an initial step, the presumption being that the same technology for flat glass is applicable to more complex shapes by changing the bearing shape. Akilian created the first such non-contact slumping device, which is shown in Figure 1.5. In this device, silicon carbide bearings, and matching silicon carbide plenums are clamped together and held in a vertical configuration.

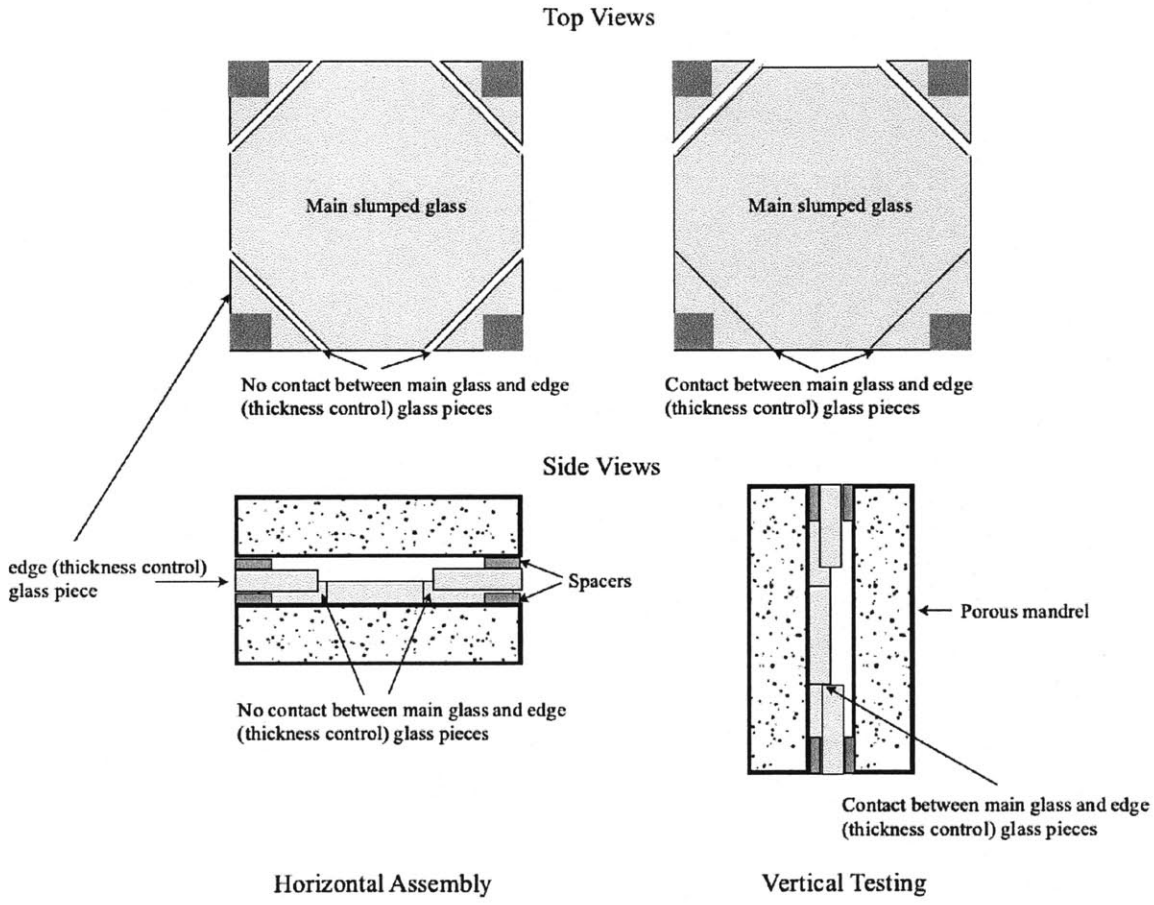

Figure 1.6: Glass edge constraint schematic [1].

To maintain a precise gap and constrain the glass, small triangular pieces of glass were sandwiched between two 50 μm thick tantalum shims and placed at the corners in between the air bearings. The glass sheets to be slumped were cut into a hexagonal shape by cutting off the

corners. The resultant diagonal corner edges rested against the two small triangular glasses on the bottom of the assembly. The configuration is illustrated in Figure 1.6.

1.3.1 Akilian's vertical slumping results with edge constraints

Two sheets of glass were slumped, the results of which are shown in Figure 1.7. The glass used started with a peak-to-valley (P-V) warp of 400 μm. After slumping, the P-V was about 15 μm.

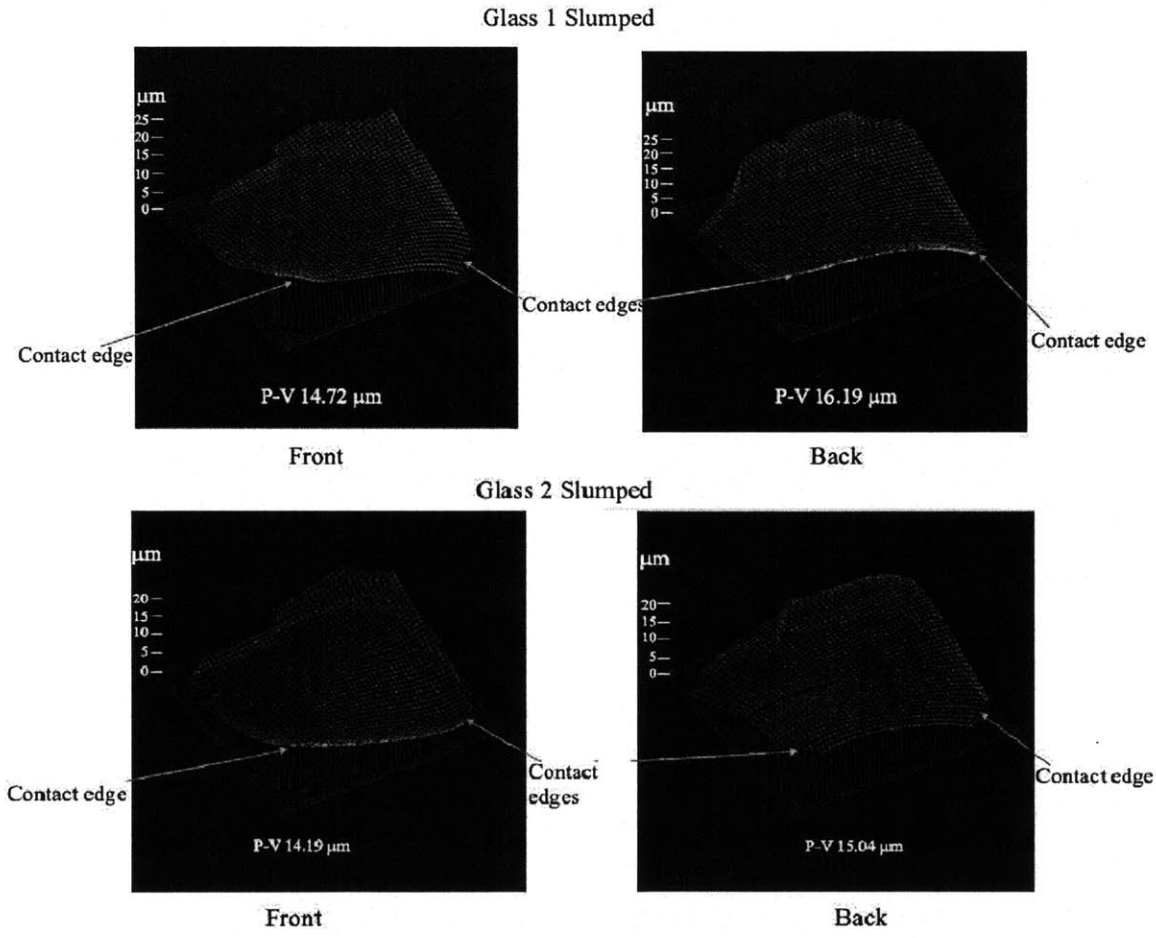

Figure 1.7: P-V plots of vertically slumped glass edge constrained at corners [1].

1.3.2 Akilian's vertical slumping results with point constraints

It was hypothesized that the edge constraints were causing the P-V errors seen in the results. To verify this, the constraints were changed from edge contacts to point contacts, by changing the shape of the corner constraint glass pieces to squares, as illustrated in Figure 1.8.

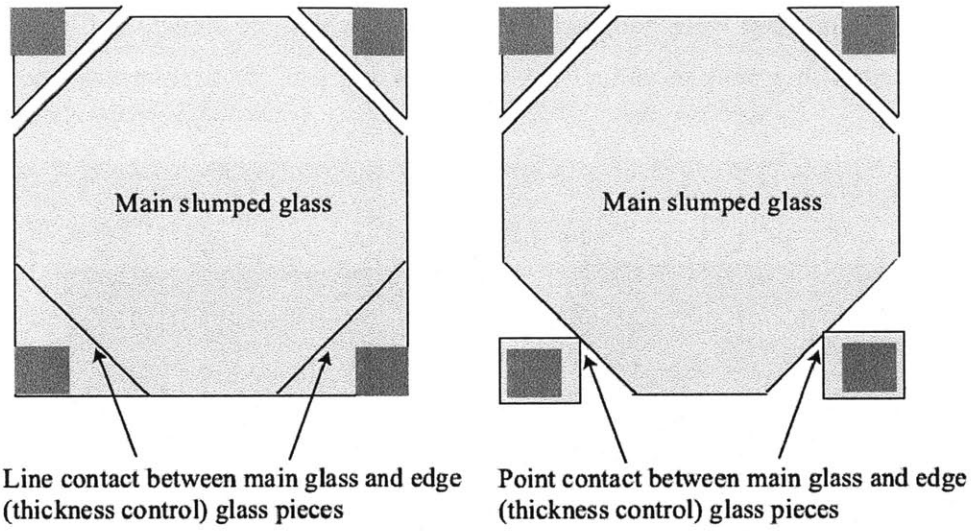

Figure 1.8: Glass point constraint schematic [1].

Again, two sheets of glass were slumped, the results of which are shown in Figure 1.9. The P-V improved to about 11 μm, but the shape of the warp became less repeatable. Akilian concluded that the method of constraint was affecting the shape of the glass.

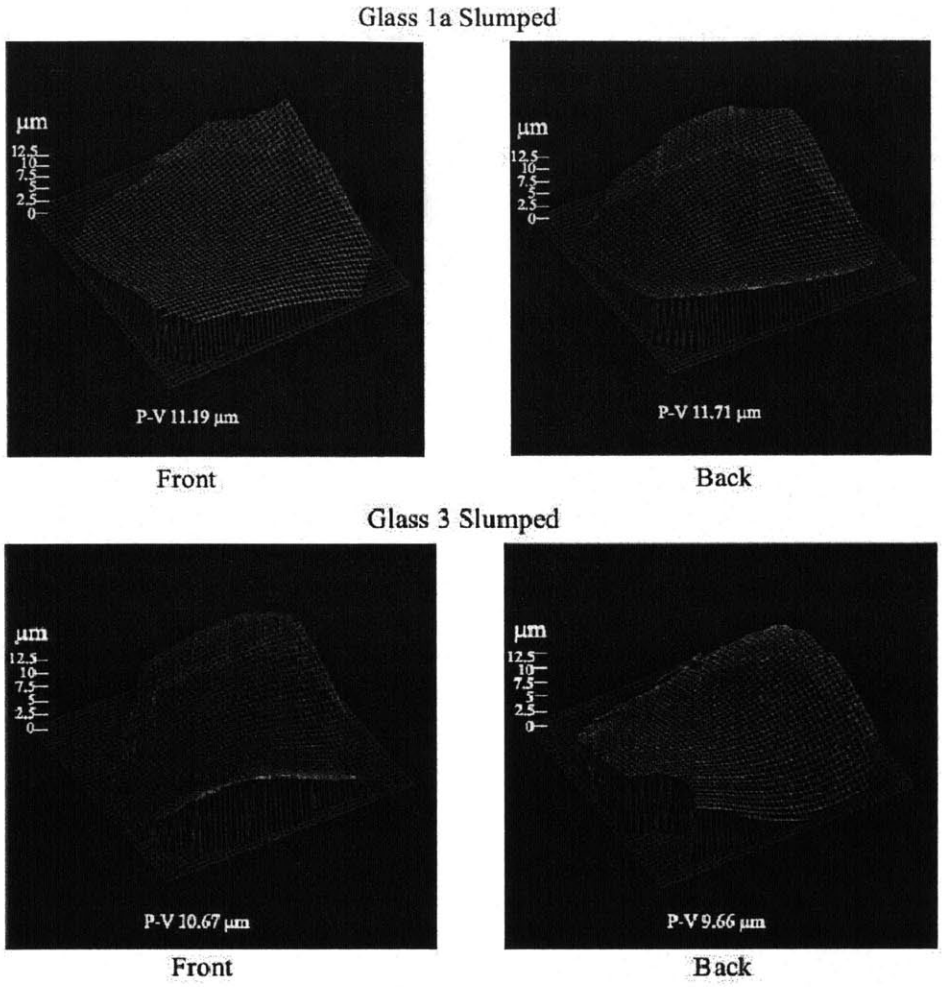

Figure 1.9: P-V plots of vertically slumped glass point constrained at corners. Glass 1a is glass 1 slumped a second time [1].

1.3.3 Husseini's vertical slumping results with hook constraints

To reduce the effect of constraint fixtures on slumped glass, Akilian attempted hanging the glass from two hooks. Two holes were cut in the topmost section of the glass and the glass was hung as in the illustration in Figure 1.10. This method was continued by Husseini, who's results are shown in this section.

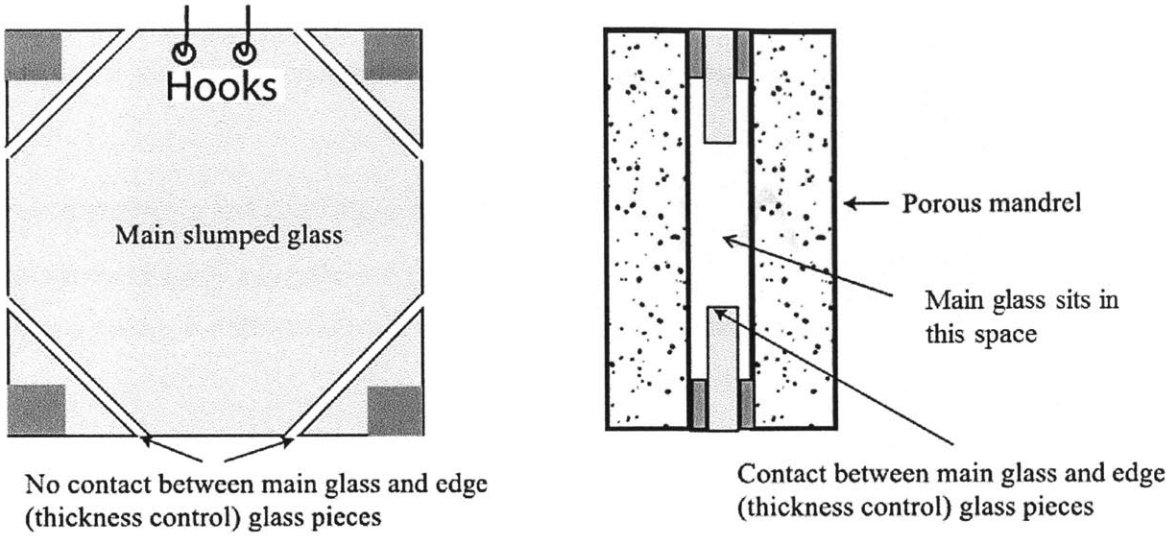

Figure 1.10: Glass hook constraint schematic [2].

Two sheets of glass were slumped, the results shown in Figure 1.11. The P-V was significantly improved to less than 3 μm.

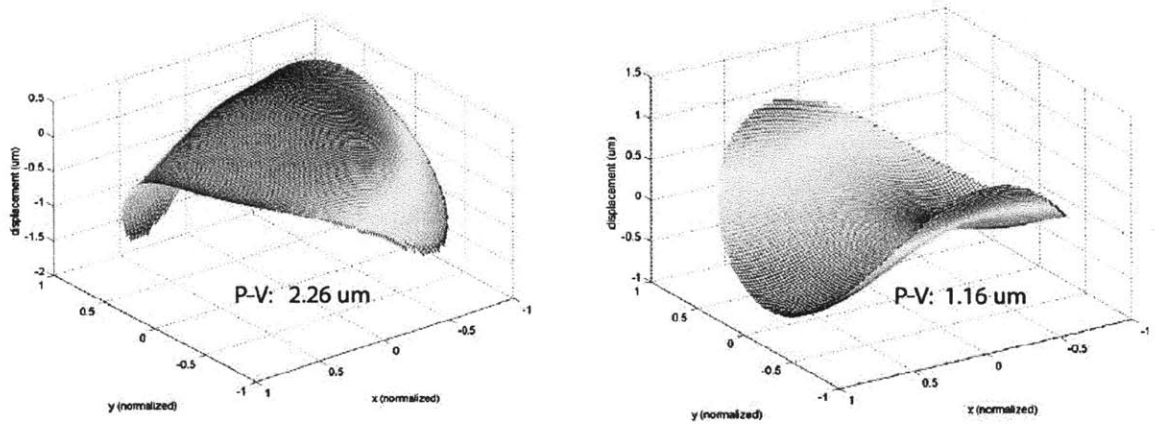

Figure 1.11: (left) Surface of glass H1; (right) difference map between Glass H1 and H2 [2].

The results suggested that the two hooks were a source of error in the slumping process, just as the corner constraints were a source of error in Akilian's experiments. Since a vertical configuration must have some sort of contact with the glass, it was decided to alter the slumping process from a vertical to a horizontal configuration. A. Husseini worked on the design of a second generation device that would slump glass horizontally. However, he graduated before his

device could be built and tested. J. Ma, a summer intern at the Space Nanotechnology Lab, ordered and assembled most of Husseini's design. This paper picks up the development of non-contact slumping technology.

CHAPTER

2

CONTINUATION OF A. HUSSEINI'S DESIGN

2.1 Design Overview

Husseini's design uses a combination of coarse and fine movement actuators to control the top ceramic bearing position while the bottom bearing remains stationary. The actuators are placed on top of the oven so as to isolate them from the heat, and are connected through the roof to the top bearing through long flexural rods. The course movement is actuated by a stepper motor from Anaheim Automation while the fine movement is actuated by three piezo stacks from Piezojena. The three actuators are placed in an equilateral triangle configuration and have a maximum range of 100 μm.

Gap feedback is achieved through three high temperature capacitance sensors from Capacitec, which are also placed in an equilateral triangle configuration aligned with the three piezo actuators. The capacitance sensors have a maximum range of 2.5 mm. The design is illustrated in Figure 2.1.

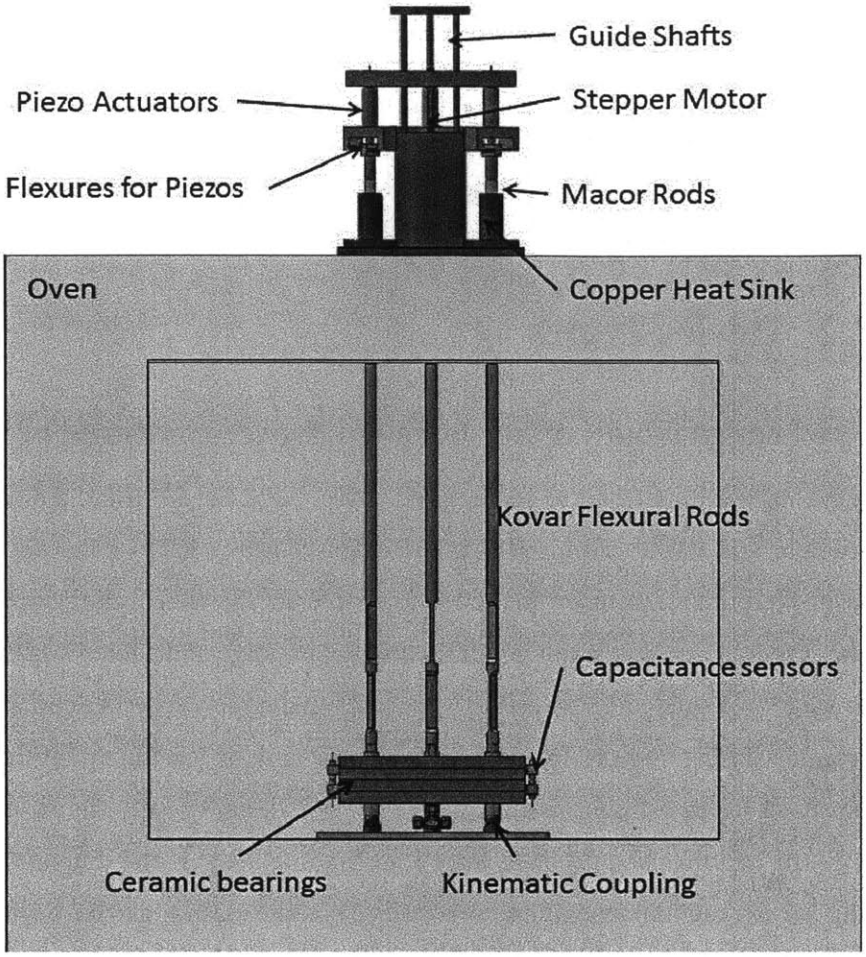

Figure 2.1: Schematic of design by Husseini. [2]

The flexural rods are essentially two blade flexures stacked axially. This allows for rotation about two axes. Each flexural rod is pulled up against a piezo stack using another preloaded flexure. The Macor rod in between the rod and piezo stack is for heat isolation of the piezo, which is susceptible to heat damage.

A single bearing assembly (two such assemblies are required) consists of a flat ground ceramic plate, a plenum plate of the same ceramic, three Kovar inserts to hold the capacitance sensors, and one Kovar insert to hold a thermocouple to monitor plenum temperature. Alumina oxide, procured from Refractron, was chosen as the ceramic material, and the two ceramic pieces were to be bonded using an adhesive with alumina oxide filler. Any metal pieces that go inside the oven were machined out of Kovar due to the fact that Kovar has a similar CTE to alumina

oxide at 600°C according to manufacturer specifications [2]. The Kovar pieces were to be brazed to the ceramic.

Because the glass sheet is floating on air, it can fall out of the bearings. A metal retainer was to be placed at the periphery of the bearings to keep the glass in between the bearings.

2.2 Device Issues

2.2.1 Movement issues: driver burn-out & over-constraint of top stage

The stepper motor driver had to be replaced twice. After the 2nd time, a closer look was taken at the problem and it was surmised that the constant heavy load of the upper assembly might be at cause. To fix this, springs were added to counteract the weight of the upper assembly. Additionally, the motor driver was taken out of its original package and cooled with air flow.

The top stage was guided by three 3/8" diameter shafts placed in an equilateral triangle, which overconstrains sliding motion. In addition, 3/8" proved to be too flimsy for the application, and the bearings used for the sliding motion were only 3/4" long. A well-known design rule is that the length of the bearings should be at least four times as long as the diameter of the shaft that it is sliding on for smooth operation; otherwise, binding occurs as the bearing becomes angularly misaligned with the shaft. As a result, a stuttering effect was produced while moving the top stage with the stepper motor. That is, the assembly would continue to bind and release throughout the movement, which resulted in non-repeatable tilts of the top stage. The piezo stacks only had a maximum range of 100 μm, which was insufficient to correct for the tilting of the top stage. In addition, the usual methods of preloading, such as springs or uneven weight distribution, could not correct the tilting either because of the overconstraint.

Eventually, the 3/8" diameter shafts were removed and replaced with two 3/4" shafts. In order to remove overconstraint, the top stage was altered as shown in figure 11. The two disjoint coaxial bushings were epoxied in for alignment purposes, and the third bushing was mounted on a flexure for exact constrainment.

The springs were removed and replaced with a pneumatic cylinder.

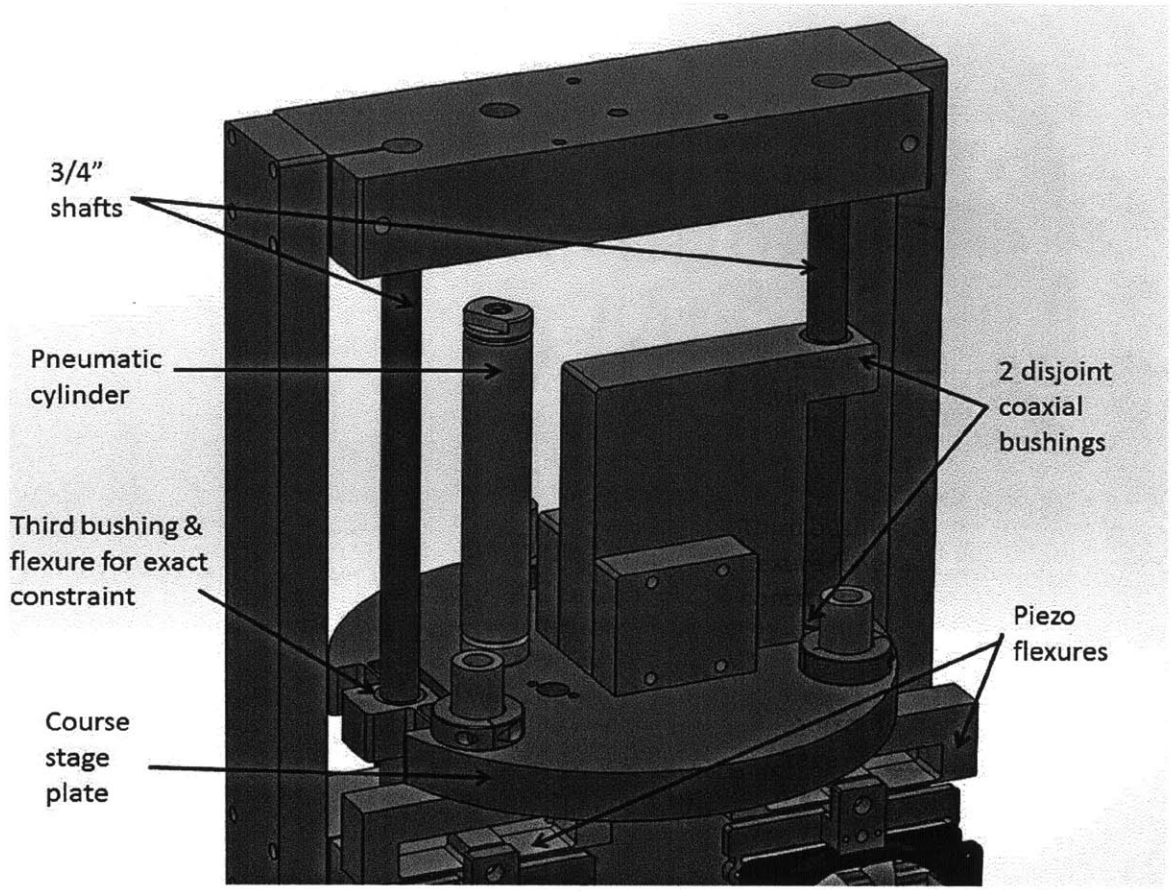

Figure 2.2: Modification of Husseini's design – guide rail replacement

2.2.2 Macor rods

The Macor rods used to thermally isolate the piezo stacks from the oven proved to be too brittle. The Macor rods connect to both the flexural Kovar rods and the piezo flexures via threads, which constantly chipped and broke away. Thus the threads could not be tightened enough for preloading. In addition, this has the disadvantage of not allowing clocking of the components, which became an issue because the piezo flexure is a rectangular block and hits other components.

The Macor rods were replaced with stainless steel heat grids that were cooled with air. The threaded connections were replaced with c-clamp style connectors, which allow for clocking of the components. The alterations are shown in Figure 2.3.

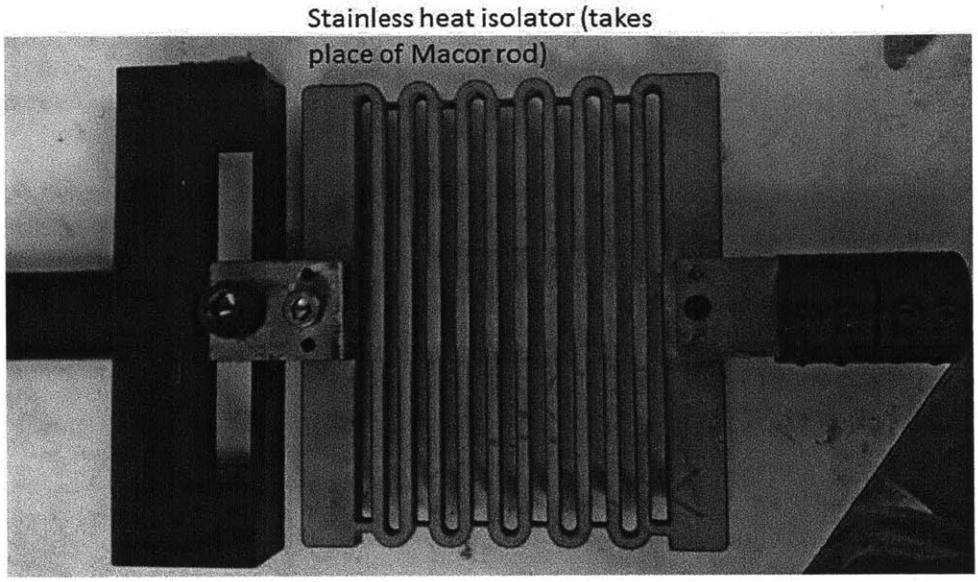

Figure 2.3: Modification of Husseini's design – replacement of Macor rods with heat isolators.

2.2.3 Bearing assembly issues: brazing alloy & Kovar CTEs, Vacuum methods

The first set of alumina oxide plates as designed in Husseini's thesis cracked in half during shipping, bringing to light a structural flaw. In the plenum piece, the groove for the Kovar insert for a thermocouple ran across the entire side wall, which reduced the effective area moment significantly and allowed for stress concentrations. After graduation, Husseini redesigned the plenum plate such that the Kovar insert becomes smaller and no longer extends across the entire side wall.

It should be noted as well that the alumina oxide was extremely brittle and rough. Running a finger across the surface resulted in loose particles. Additionally, the plates were 0.75" x 12" x 12", which is too thin to be held properly without causing warp during grinding processes. Although flatness measurements were not made, it is highly doubtful that the flatness tolerance was better than 10 μm.

A quick check of the chosen brazing alloy, Incusil, shows that the CTE is much larger than that of the ceramics [8]. It was not tested whether or not this would cause failure due to

uneven thermal expansions. However, it was decided to replace the brazing process with a ceramic to metal adhesive from the supplier Aremco.

Ceramabond 503 was used in bond strength tests. The alumina oxide plates bonded strongly and attempts to separate the parts resulted in the plates themselves breaking apart. The Kovar to ceramic bond was weaker, allowing separation, but was strong enough for the application, requiring about 10 psi to break the bond.

After ceramic adhesive testing, adhesive was applied to the bearing assemblies and the assemblies were cured in an oven as per manufacturer's instructions. This turned out to be disastrous as it was discovered after the curing process that the ceramic plates were cracked in the middle. The fractures started exactly where the Kovar pieces were fitted in, showing that Kovar is thermally ill matched to alumina oxide. A study done on Kovar-alumina joints shows that Kovar has a similar CTE to alumina oxide until 450°C, but expands much more rapidly at temperatures greater than 450°C [9]. The graph in Figure 2.4 compares the CTEs of Kovar and alumina oxide. In addition, different suppliers post different CTE values for Kovar, one of which says that the CTE of Kovar at 600°C is as high as 14ppm [10][11] as opposed to the 5ppm for alumina oxide. It appears that every supplier manufactures a significantly different Kovar. Even if failure had not occurred, the CTE mismatch would have resulted in distortions of the bearing.

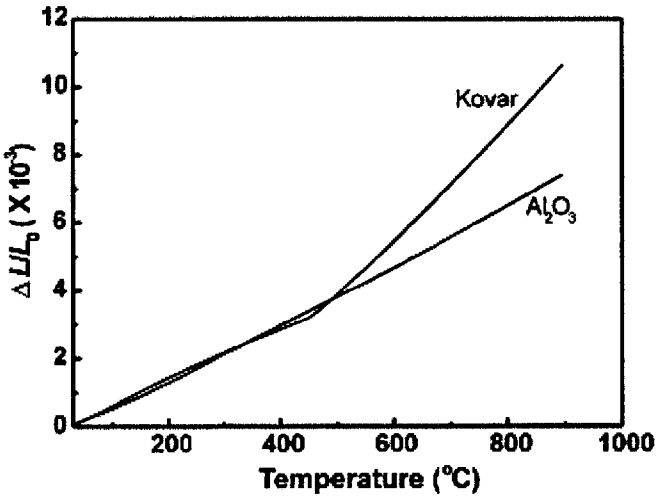

Figure 2.4: Coefficients of Thermal expansion of Kovar and alumina oxide [9].

Because the alumina oxide bearings were unusable, it was decided to make an adapter for the old silicon carbide bearings used in the first generation device made by Akilian. Graphibond from Aremco was used to bond the flat silicon carbide pieces to the plenum pieces.

The issue with metal to ceramic bonding remained unsolved, so a new way to hold the bearing assemblies using vacuum pressure was devised. Since the silicon carbide pieces were porous, adhesive was rubbed into the back of the plenum piece to form a solid surface. Then a metal cup with vacuum pressure was placed on the solid section of the plenum piece, thus forming a strong but non-bonded connection. This method also has the advantage in that the friction force is weak enough to allow lateral slippage so that CTE mismatch is not an issue. The metal cup can expand more than the ceramic bearing, and since the connection is non-bonded, the rim of the cup can shift on the ceramic surface without causing distortions. A Solidworks model of this setup is shown in Figure 2.5.

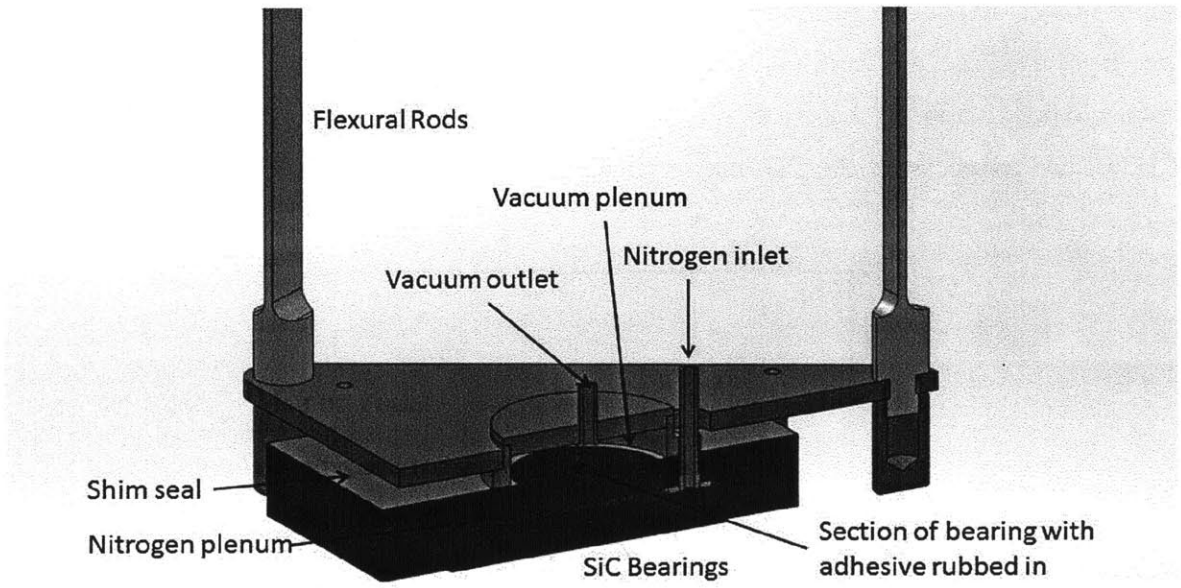

Figure 2.5: Vacuum holder for ceramic bearings.

2.2.4 Drift: zero-ing and expansion of bars

The proposed method for zero-ing, or aligning the bearing gap, was to lower the top bearing assembly using the stepper motor until it hit the lower bearing surface. Then the

capacitance sensor values would be recorded and subtracted from future values to create a zero reference. The issue found was that every time the top bearing assembly was raised and then lowered again, the zero reference was shifted by a significant amount, sometimes greater than 100 μm. Many factors could have contributed to this error, including tilt of the top stage plate, complexity of design/number of components, and that the lower and top assemblies were not fixed with respect to each other.

The flexural Kovar bars are 1 meter long. The equation for thermal expansion is as follows:

$$\Delta L = L\alpha\Delta T \tag{2.1}$$

Using L = 1 m, α = 15 μm/m-K, and ΔT = 600°, ΔL comes out to be about 10 mm. This further complicates procedures and ensures that there will always be gap error because it cannot be guaranteed that the conditions for all three bars will be exactly the same. For example, the bars cannot be clamped perfectly evenly at the top, or the bars will protrude into the oven unevenly due to floor or oven tilt. To estimate the error that these and other factors might introduce, equation 2.1 is used again, but this time using L = 0.01 m. In this case, L is the maximum difference in bar protrusion length into the oven (starting from the oven ceiling). The error ΔL is then 0.09 mm, or about 100 μm. This is very large because the selected piezos only have a range of 100 μm.

Combining this new thermal expansion error with the zero-ing error, the maximum error is much larger than the error budget of 100 μm, and the design becomes unviable. At this point the device was discarded, and slumping was attempted with shims for gap constraint. Chapter 3 discusses the results.

CHAPTER

3

COMPLICATIONS OF HORIZONTAL SLUMPING

3.1 Simplest setup

After discarding Husseini's design (tool generation 2.1), it was decided to return to the simplest possible design, which is two bearings clamped together and separated by precision shims. The shims were placed on three of the four sides of the bearings, and the bearings were tilted slightly at an angle of about 10° so that the edge without any shims had the highest altitude. Gravity ensured that the glass sheet would not fall out of the open side and the shims acted as a retainer, keeping the glass piece in between the bearings. The gap between glass and bearing was set at 50±100 μm, and the glass was 400±25 μm thick, for a total of 500±125 μm of separation between bearings. The large uncertainty is due to the unevenness of the outer recess machined into the bearings. The setup is shown in Figure 3.1.

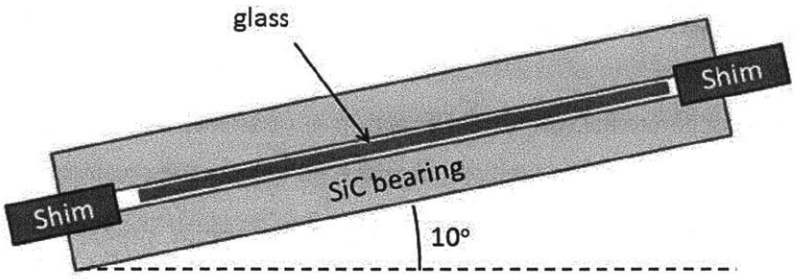

Figure 3.1: Schematic of setup.

A variation on the setup was also attempted, where a small clip was placed on the upper section of the glass, preventing the glass from sliding in between the bearings completely. This is, in effect, the same procedure as Akilian's vertical slumping device, which held the glass with two hooks, only it is rotated 80°.

3.2 Results

A rectangular glass sheet was slumped in the described setup three times: first at 0.5 psi, then at 1 psi, and last at 5 psi plenum pressures. After the first slump, the glass formed slight ripples at the two edges that rested against the shims. From a side view, the ripples cannot be ascertained with just eyesight, but from a top view, the distortions in light reflections made the waviness of the glass sheet easy to see. The ripples along the x-axis were hardly noticeable, since the tilt along the x-axis was close to 0°, but the ripples along the z-axis were much more pronounced.

It was concluded that gravity was causing the ripples by forcing the glass sheet to press up against the shims with more force than the air bearing pressure could compensate for. To try to overcome the gravity force, the pressure was increased to 1 psi, and the glass was slumped again. The result was largely the same, with no significant differences. The pressure was then increased to 5 psi, and the glass was slumped a third and final time. This time, the ripples were much larger, to the point that they were visible to eyesight from a side view. Figure 3.2 illustrates the type of deformation seen.

Figure 3.2: Exaggerated sketch of deformation in glass sheets after thermal cycling.

If just the gravity force were at work, then the ripples probably should have been eliminated at higher pressures. However, since higher pressures exacerbated the issue, it was hypothesized that fluid sheer force might also be at work. If the gap is not exactly the same all around the bearing, then the two bearings are at a slight angle to each other, which would create a low pressure zone where the gap is largest and a high pressure zone where the gap is smallest. The nitrogen flowing through the air bearing would flow from the high pressure zone to the low pressure zone, resulting in a shear force in the same direction. A higher plenum pressure would increase the flow rate and therefore increase the shear force as well. If there was a gradient in gap between the bearings, and, by chance, that gap was aligned in the same direction as the gravity vector, then it would explain why the increase in pressure actually made the waviness in the glass worse.

To confirm the effect of sheer force, the gap was purposely increased on one side of the bearing. The bottom bearing was leveled to be horizontal to a tolerance of 0.03° using a Starrett level. Then the gap was set at 50 ± 50 μm at one edge and 200 ± 50 μm at the opposite edge. Inserting a glass sheet from the side resulted in the glass sheet moving from the small gap side to the high gap side. To be certain, the bottom bearing was slightly tilted, with the gravity vector opposing the shear vector. The side with 50 μm gap was elevated by 100 μm, and the procedure was repeated. Again, the glass sheet moved from the small gap side to the high gap side, confirming our hypothesis.

3.2.1 Clamping

The variation with the clip, as mentioned previously, was only attempted once at 1psi plenum pressure. While the lower and side edges now stayed ripple free since they no longer contacted any shims, the top part became a problem. As the glass heated up and reached the softening point, the part of the glass that was not sandwiched in between the bearings sagged and tilted downwards, forming an L-shape. This in turn induced propagated ripples along the length

of the glass, as illustrated in Figure 3.3. The ripples are strongest at the glass bend and decrease in amplitude as they go away from the bend.

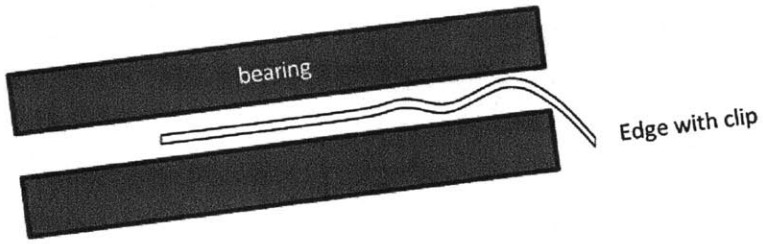

Figure 3.3: Illustration of ripple propagation due to gravity.

The explanation for this is that the glass sagging down creates a low pressure zone above the bend and a high pressure zone below the bend. Therefore the section of the glass with the bend gets pushed upwards to compensate and balance forces. That in turn causes a difference in pressure to the side of the bend, only this time the high pressure zone is above the glass and the low pressure zone is below the glass. Then that section of the glass gets pushed downward, and so on, creating a propagation of ripples.

3.3 Conclusions drawn

Using a solid retainer to hold the glass piece in between the bearings will result in ripples along the contacting edges. Even if nothing solid were contacting the glass edge, and the glass were kept from falling out from in between the bearings by blowing air against the edge of the glass, the result will likely resemble what was seen in the experiment. That is, any lateral force applied to the edge of the glass will result in unwanted waviness after slumping.

The only way to passively keep the glass in place without resulting in waviness is to perfectly level the bottom bearing and to make the bearing gap perfect. However, neither of these is feasible, and in addition the glass sheets themselves have warp and thickness variation.

To achieve the goal of horizontal slumping, the device must be able to sense the position of the glass and affect that position without using lateral forces against the edges. The technologies to do so were developed and are presented in chapters 4 and 5, respectively.

It is also conceivable that a clamping method could be devised that would not induce the ripples as described in section 3.2.1. For example, instead of clamping the glass such that there is a part sticking out of the bearings, one could place the entire glass in between the bearings, but place a 25 micron (0.001") shim on either side of the glass at the top edge and clamp the layers together using the bearings. The rest of the glass would be floating. Then two other shims that are the thickness of the glass plus the two 25 micron shims would be placed in a triangular configuration to set the gap of the bearing. This hypothetical setup is shown in Figure 3.4.

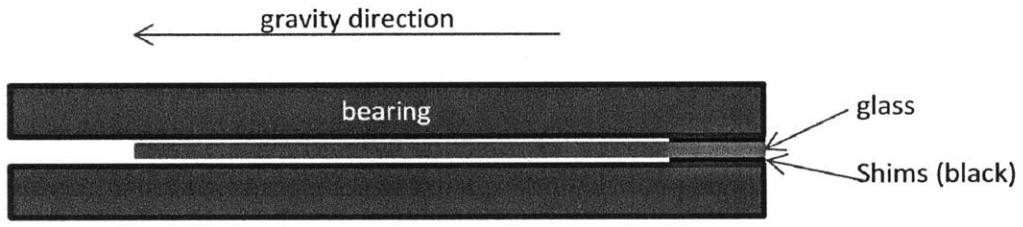

Figure 3.4: Concept of slumping with a clamped sheet of glass (rotated 90° from vertical)

The bearings would have to be clamped with minimal force so as to not deform the glass excessively. It is also not certain what effects this type of clamping would have on the glass while slumping. This method was conceptualized much later on, which is why it was not attempted in the early stages of the research.

CHAPTER

4

OPTICAL DISTANCE SENSING

4.1 Silica fibers

Not many sensors can operate in a 600°C environment, fit into a 500 micron gap, and give position data over a semi-large range (~10 mm) without affecting the actual position of a thin light glass piece. The capacitance sensors purchased from Capacitec can operate in a high temperature environment, but would not be applicable unless the edges of the glass were coated with a metal. Even then, position data would be limited to 2 mm at best, data would be significantly distorted due to the thinness of the glass, and fitting the sensor within the bearing assemblies would be a nontrivial task. Instead, it was decided to build a custom optical sensor using high temperature silica fibers from IVG Fibers.

4.1.1 Copper sheath oxidation

Although the fibers themselves suffer no damage at high temperature, the chosen fibers come clad in a copper sheath, which oxidizes far below the required temperature of 600°C. A simple heat test of fiber samples confirmed the issue, as the copper turned dark brown and extremely brittle. The fibers snap too easily and become impossible to work with after oxidation. A higher temperature metal coating such as nickel would be able to prevent oxidation from happening. Unfortunately, IVG Fibers only offers copper and aluminum sheaths due to limitations of their extrusion process.

Fiberguide Industries offers a gold plated silica core fiber that can be heated up to 700°C. However, the quoted price per meter was upwards of $600, which was deemed too expensive at the time.

The chosen solution to the above issue was to put the fibers inside stainless steel tubes, which would be flooded with nitrogen. Testing revealed that even the smallest flows of nitrogen are enough to purge the vicinity of the fibers of oxygen, preventing oxidation from occurring. The copper cladding does still anneal and becomes very malleable, as the nitrogen flow is not enough to cool the entire fiber along its length.

The preferred solution would be to add a second coating of nickel through an electroless nickel plating process. This process works the same way as anodizing or galvanizing. This will be the method of choice in the future.

Another solution would be to completely strip the fibers of their copper sheathing using ferric chloride, a well-known copper etchant. The fibers would have to be handled with care, but they would not turn brittle. It should be noted that this would only work with step-index fibers, since the entire fiber would be exposed.

4.1.2 Fiber aperture blockage

Through testing with the final device, it was found that very low pressures had to be used to float the glass. Control became more difficult with higher pressures. 0.01 psi was used for the plenum pressure. At this low pressure, there is not enough nitrogen flow through the ceramic bearings to prevent oxidation of the fiber lengths (~1") that are inserted in between the bearings. More specifically, it is suspected that the fiber holders restrict the flow of nitrogen, guiding the flow around the fibers.

Because of the presence of ambient air, the copper sheathing at the tips of the fibers oxidizes, releasing debris. The particles get in front of the fiber apertures, forming an opaque cover and blocking light. When this happens, the sensors cannot send and receive light, and the device loses control of the position of the glass.

To prevent this from happening, the fibers were mechanically stripped at the tips (~2mm). A blade is used to cut into the copper circumferentially, stopping short of the fiber core. Then the copper at the tip is pulled off.

A second nickel plating as discussed in the previous section would remove the need to mechanically strip the fibers.

4.2 Custom optical setup

The custom optical sensor has two silica fibers juxtaposed together and directed orthogonally to the sensing surface, which, in this case, is the thin edge of the glass. Light from a laser comes through one fiber, reflects off the edge of the glass, and is received by the second fiber, which is connected to an amplified photodiode. The closer the glass edge is to the fibers, the higher the photodiode voltage. The distance correlates to a nonlinear voltage that can be computed to a best-fit line. The optical setup is illustrated in Figure 4.1.

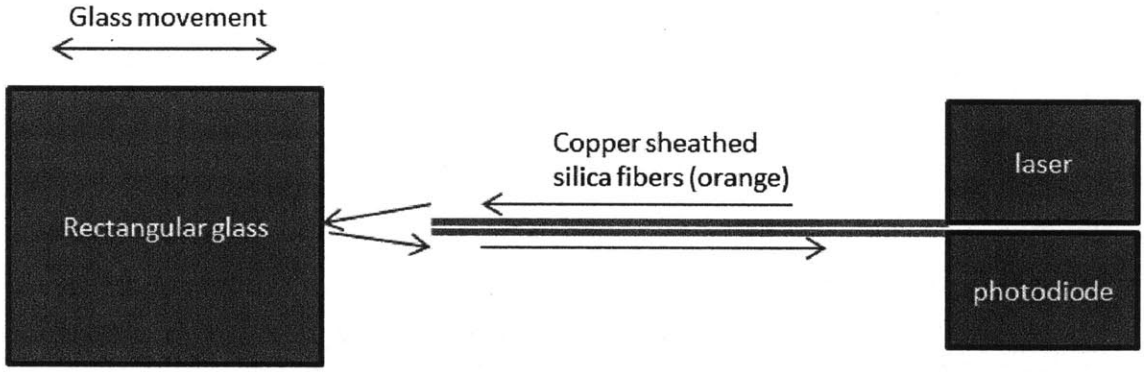

Figure 4.1: Schematic of optical sensor.

4.2.1 Limitations

There are four limitations to the optical setup. These limitations are illustrated in Figure 4.2. The first is that the edge of the glass must be as smooth as possible to eliminate sensor noise. Unfortunately, most commercially available glasses do not come with polished edges. The Schott D263 glass used in our experiments had a rough edge with many facets instead of one smooth surface. It is still possible to estimate the position of the glass to an acceptable degree, but the signal must be smoothed through a low-pass filter or moving averages. Disregarding the high

frequency spikes that get through the low-pass filter, the sensor was found to have a tolerance of about +/- 1mm, which is accurate enough for the purposes of the device.

The second limitation is simply a range limitation. At distances greater than 20mm, the light bouncing off the edge of the glass and being read by the second fiber is too miniscule to fit to the best-fit equation.

The third limitation is due to the juxtaposition of two fibers that have significant thicknesses. Because we are using one fiber to send out light and the other to receive it, the light being sensed is actually at an angle to the fibers. Therefore as the edge of the glass gets closer and closer to the fibers, there is a point at which the photodiode voltage starts to decrease. This critical distance was determined to be 2mm during the calibration process described in section 4.2.2.

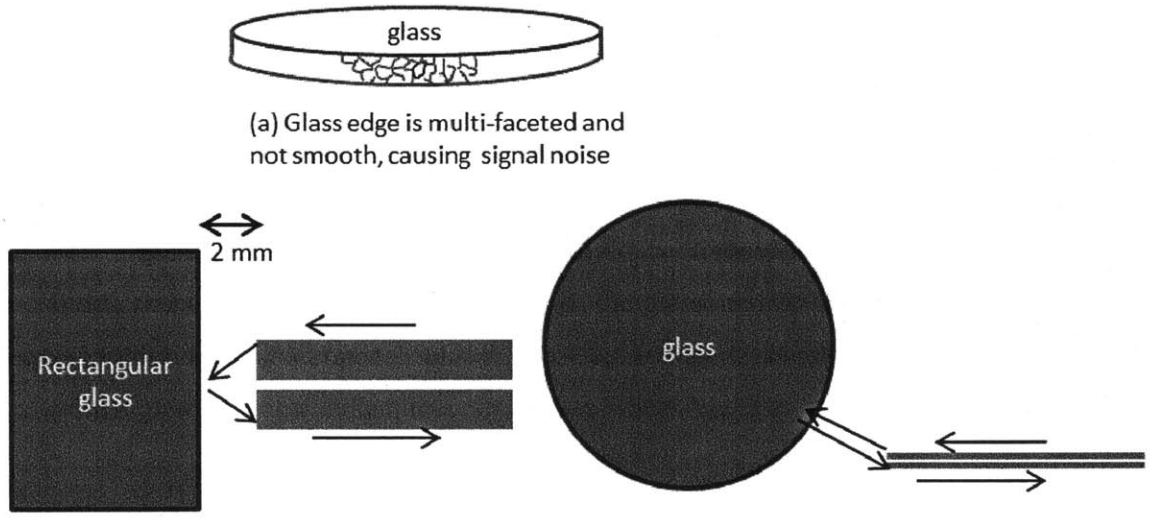

(a) Glass edge is multi-faceted and not smooth, causing signal noise

(b) At close distances, the light must reflect at a large angle from perpendicular and the voltage starts decreasing when closer than 2 mm

(c) When a round glass moves off-axis, the photodiode voltage starts decreasing due to the curvature of the edge

Figure 4.2: Limitations of custom optical sensor.

The last limitation has to do with the shape of the glass. The sensor works best if the glass has a rectangular shape and is oriented such that the fibers are perpendicular to the reference edge. However, it is difficult to maintain the rotational orientation of a glass piece without contacting it. Therefore the rectangular sheets were switched out for round sheets.

Although this removes the rotational orientation issue, it adds another variable since the edge is not straight. That is, for control of a glass round in two orthogonal axes x and y, the distance data is parasitic. When the glass moves a large amount in the direction of the x-axis, it moves off -axis in the y-direction, which decreases the light received by the second y-axis fiber since the light is bouncing off the edge at an angle instead of perpendicularly. This causes the sensor to think that the glass has moved in the y-direction, which it hasn't. More on two-dimensional position sensing with round glass is discussed in section 4.3.

4.2.2 Calibration

Calibration was initially done with a rectangular glass sheet, which was mounted on a movement stage with a precision fine thread adjustment screw. Two fibers were setup in the manner described previously. Using the adjustment screw, the distance from the fibers to the reference edge of the glass was increased in discrete increments. The photodiode voltage was recorded at each increment. The calibration plot is shown in Figure 4.3 along with the best-fit curve.

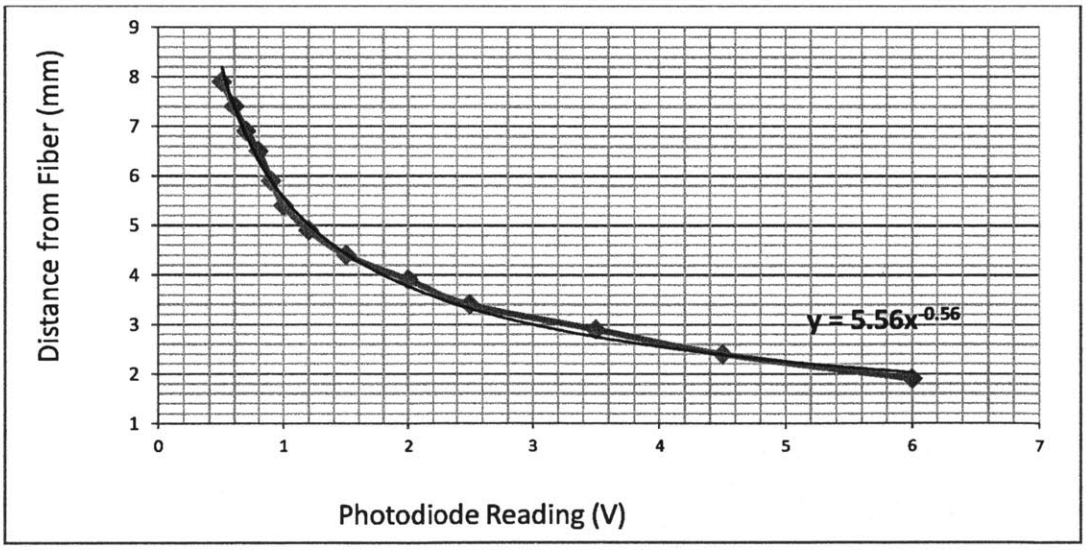

Figure 4.3: Optical sensor calibration plot.

A power curve approximates the data best. The calculated best-fit curve is

$$x = 5.56 * V^{-0.56} \tag{4.1}$$

where x is the distance from the fiber tips and V is the photodiode voltage.

4.3 Two-dimensional optical sensing

For two-dimensional position sensing, the laser is split into two using a fiber splitter and is directed into two identical fiber assemblies. The fiber assemblies are situated 90 degrees apart. The diagram in Figure 4.4 shows the optical circuit.

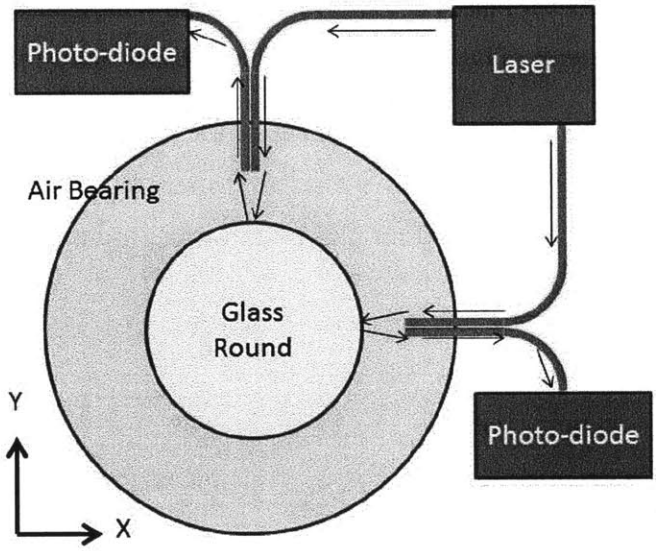

Figure 4.4: Schematic of two dimensional optical sensing configuration.

4.3.1 More calibration

As mentioned previously, the round shape of the glass results in a parasitic error between the two orthogonal axes. Therefore, although the sensor has a range that is close to 20 mm, it is best to stay in a range that is well below that, where the curvature of the glass does not have such a large effect and can be roughly approximated as a straight edge. For a 100mm diameter glass round, this range appears to be less than 5mm offset from either axis direction. The larger the glass sheet, the larger the range will be since the curvature is smaller.

It is also helpful to add two constants c_1 and c_2 to equation 4.1 as adjustment constants for the curvature, resulting in the following equation.

$$x = c_1 * 5.56 * V^{-0.56*c_2} \quad (4.2)$$

These constants are obtained experimentally. The proper way to calibrate for two axes would be to create a grid and record the photodiode voltages for every point on the grid that the center of the glass can be placed on. However, this is difficult and extremely tedious. Since a high accuracy is not required for the device, it was decided to forgo this process.

4.3.2 Position uncertainty

While controlling the position of the glass in the final device, it was discovered that there is now position uncertainty due to the parasitic error of the two axes. Position uncertainty means that, for a given set of photodiode output voltages, there may be multiple possible glass positions. For example, when the x and y-axis sensors read a "middle" and a "high" position value, the glass may actually be in a "middle" and "low" position value, only the glass has moved so far off axis of the y-axis sensor that it reads it as a high value. Or if both sensors read a "high," the glass may actually be at a "low-low" position, stuck in between the two sensors. This effect is illustrated in Figure 4.5.

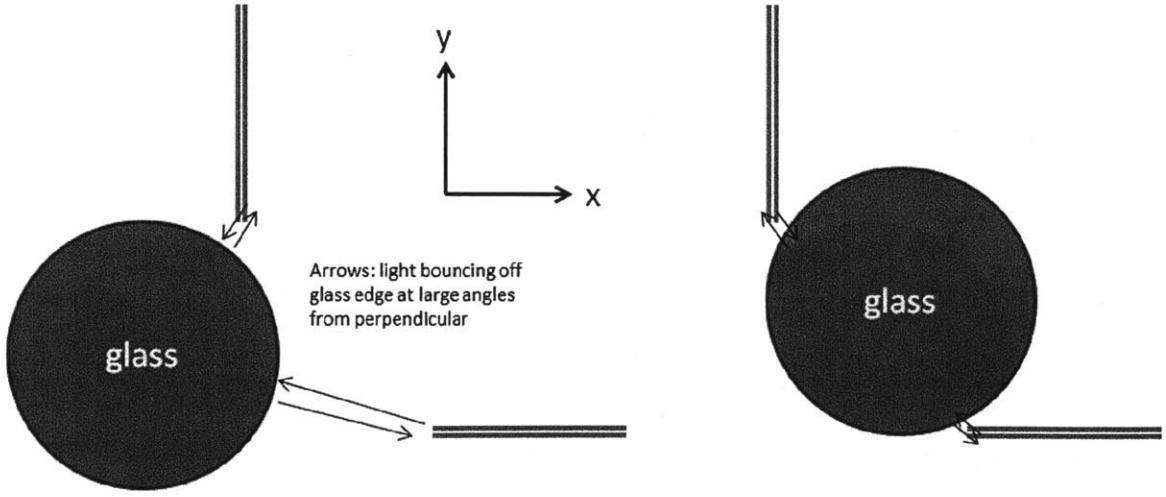

Figure 4.5: Position uncertainty effect.

To mitigate this effect, two solutions are possible: a physical limiting retainer and additional optical sensors. As was ascertained earlier in chapter 3, the glass cannot touch the physical retainer, so the retainer must be large enough to accommodate the movement of the glass, but still be small enough so that if the glass does move off-axis, it is not enough to throw off the sensors. Additional optical sensors add redundancy and significantly improve the position certainty of the sensors. The more sensors there are, the more accurately the position can be known.

This position uncertainty was not an issue in the initial development of position control technology perhaps because a much larger sheet of glass was used (150 mm diameter as opposed to 100 mm diameter for the final device). With larger diameters, the glass edge has a lower curvature and can therefore move farther off-center before the parasitic error becomes significant enough to cause position uncertainty. Therefore the cold version prototype (non-oven version) only used two optical sensors.

CHAPTER

5

NON-CONTACT POSITION ACTUATION

5.1 Is there a passive method to position the glass?

As discussed earlier in section 3.3, the glass must be positioned without using any physical contact or any forces on the edges. The ideal method would be some passive way that does not require active control. However, the system is unstable and the slightest tilt in the device will cause the glass to fall out of the bearings. In addition, the glass will always want to follow the flow of nitrogen (the fluid used with the air bearings), which is always directed radially outwards.

Three types of forces come to mind which could possibly provide a passive centering force. The first would be gravity, which would work well with a convex shape (the lower bearing would be bowl-shaped). This does not work for a flat shape, but would help greatly later on, when the switch is made from flat glass to cylindrical and hyperbolic glass. With glass sheets with curvature, one of the axes would be stable, which means only the position in the other axis would have to be controlled. This would not run into the issues of two-dimensional position control discussed in chapter 4.

The second force that could provide a restoring force would be magnetism. However, this is impossible or at least extremely difficult at 600°C due to the Curie temperature of magnetic materials.

The third approach would be to manipulate the flow of nitrogen itself. If a vacuum were placed in the center of the bearings via a multi-sectioned plenum chamber, the flow of the nitrogen would be directed inward, thus creating a restoring force. However, while this would probably work at room temperature, it is doubtful that the glass would remain floating when the temperature is raised to beyond the annealing point. The two opposing vacuums at the centers of the bearing assemblies are an unstable force. For example, if a particle were initially located exactly in between two vacuums, once it deviated slightly from the center, it would get sucked into the vacuum that it is closer to. The same principle applies to the glass because, when the glass loses its rigidity, the center will likely be sucked towards one of the vacuums. It is also possible that with a high fluid flow, the fluid would provide a physical barrier between the glass and the vacuum since the flow can still be considered incompressible. However, even in such a case, there should still be some warp in the center of the glass that would not be repeatable and correctable for.

Another flow manipulation method that was considered was to create a high pressure rim around the glass via a multi-sectioned plenum chamber. The section of the bearings within the rim would be operated with a significantly lower pressure. The issue with this concept is that the high pressure rim would squeeze the glass radially inwards, which would again create ripples.

It was concluded that, at least for flat glass, a passive method of restoring the glass to the center is difficult to conceive.

5.2 Shear force equations

Since there does not seem to be a passive way to position the glass, force must actively be exerted on the glass without physical contact or forces on the edges. There are only two known methods of doing so: using fluid shear force on the flat surface of the glass, and using gravity tilt.

The equation for wall shear stress is

$$\tau_{wall} = \mu \frac{\partial u}{\partial z}\Big|_{z=0} \tag{5.1}$$

where μ is the dynamic viscosity of the fluid, u is the velocity of the fluid along the boundary, and z is the height above the boundary. Thus the shear force is actually dependent on three factors. First, since the dynamic viscosity of gases increases as the temperature increases, there is a temperature dependency. Second, the higher the pressure in the plenum, the more air flow there

will be, which will increase the fluid velocity given a set gap. And lastly, an angle in between the bearings will add another component to the fluid velocity. This third factor is the only relevant parameter since the other two factors do not offer a way to direct the fluid flow.

Since there is always fluid flow radially outwards from the center of the bearing, there is always a symmetrical fluid shear force acting on the glass. This is an unstable force, and once the glass leaves the center in a certain direction, the total shear force acting on the glass will increase in that same direction, adding to the instability.

To create a nonsymmetrical fluid shear force that can be used to position the glass, the bearings must be held at angles to each other. This creates a low pressure zone where the gap is largest and a high pressure zone where the gap is smallest, thus creating a flow from the small gap to the large gap. The direction of the flow is the direction of the shear force and the magnitude of the angle is proportional to the magnitude of the shear force. To calculate the shear force, the flow velocities must be integrated in two dimensions over the area of the glass sheet.

To calculate the velocities, Husseini's thesis [2] gives us the following equations, which are derived from the Navier-Stokes equations and Darcy's Law:

$$u = \frac{1}{\mu}\left(\frac{z^2}{2} - \frac{D+B}{2}z + \frac{D*B}{2} + \frac{k_x(z-D)}{D-B}\right)\frac{\partial p}{\partial x} \tag{5.2}$$

$$v = \frac{1}{\mu}\left(\frac{z^2}{2} - \frac{D+B}{2}z + \frac{D*B}{2} + \frac{k_y(z-D)}{D-B}\right)\frac{\partial p}{\partial y} \tag{5.3}$$

where k is the permeability constant, B is the off-nominal bearing imperfection, and D is the distance from nominal bearing surface to the glass. The relationship between h, D, and B is:

$$h = D - B \tag{5.4}$$

For convenience, a function $F(z)$ is introduced.

$$F(z) = \frac{z^2}{2} - \frac{(D+B)}{2}z + \frac{D*B}{2} + \frac{k_x(z-D)}{D-B} \tag{5.5}$$

$$u = \frac{1}{\mu}\mathrm{F(z)}\frac{\partial p}{\partial x} \tag{5.6}$$

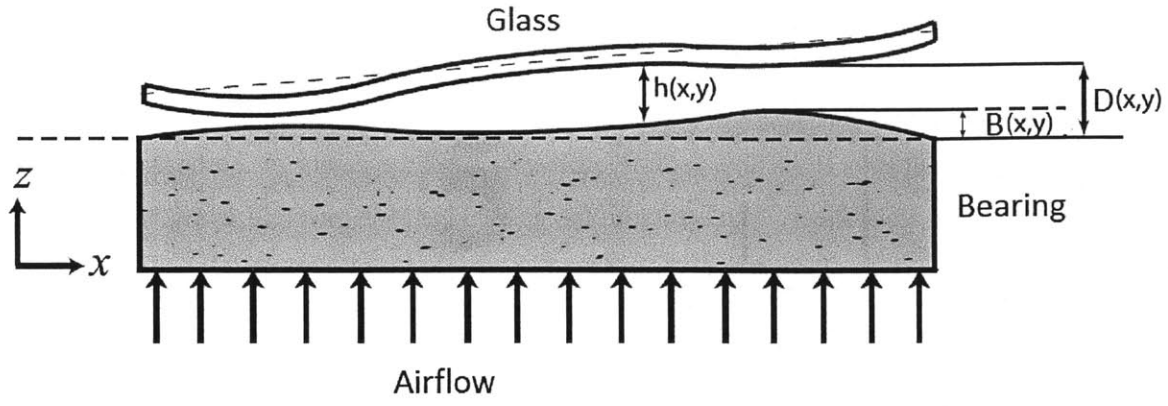

Figure 5.1: Porous air bearing with non-uniform gap.

Pressure p(x,y) is computed through FDM using the equation [2]:

$$p_{i,j,k_H} = \Bigg[\left(p_{i+1,j,k_H} + p_{i-1,j,k_H}\right) + \left(\frac{L}{W}\right)^2 \left(p_{i,j+1,k_H} + p_{i,j-1,k_H}\right) + \frac{3}{4h}\left(p_{i+1,j,k_H} - p_{i-1,j,k_H}\right)\left(h_{i+1,j,k_H} - p_{i-1,j,k_H}\right) + \frac{3}{4h}\left(\frac{L}{W}\right)^2 \left(p_{i,j+1,k_H} - p_{i,j-1,k_H}\right)\left(h_{i,j+1,k_H} - h_{i,j-1,k_H}\right) - \frac{\Delta}{2a}\left(p_{i,j,k_{H+1}} - p_{i,j,k_{H-1}}\right)\Bigg] / \left(2 + 2\left(\frac{L}{W}\right)^2\right) \tag{5.7}$$

which is also taken from Husseini's thesis. The Matlab code to compute pressure, written by Akilian, is attached in Appendix A.

Returning to shear force, equation (5.6) is inserted into equation (5.1), giving

$$\tau_x(z=0) = \left[\frac{\partial F}{\partial z}\frac{\partial p}{\partial x} + F\frac{\partial}{\partial z}\frac{\partial p}{\partial x}\right]_{z=0} \tag{5.8}$$

where τ_x is the x-component of the shear force.

The second term of the above expression becomes

$$\frac{\partial}{\partial z}\frac{\partial p}{\partial x} = \frac{\frac{\partial p_{i,j,k+1}}{\partial x} - \frac{\partial p_{i,j,k}}{\partial x}}{\Delta z} \tag{5.9}$$

However, the assumption of the model is that Δp is negligible across the gap, so the second term is zero, leaving just

$$\tau_x(z=0) = \frac{\partial F}{\partial z}\frac{\partial p}{\partial x_{z=0}} \tag{5.10}$$

Taking the partial derivative of $F(z)$ and substituting, the resulting equation is

$$\tau_x(z=0)|_{i,j} = \left(\frac{k_x}{D-B} - \frac{D+B}{2}\right)\left(\frac{p_{i+1,j,k_H} - p_{i,j,k_H}}{\Delta x}\right) \tag{5.11}$$

Similarly, for the y-axis,

$$\tau_y(z=0)|_{i,j} = \left(\frac{k_y}{D-B} - \frac{D+B}{2}\right)\left(\frac{p_{i+1,j,k_H} - p_{i,j,k_H}}{\Delta y}\right) \tag{5.12}$$

Since equations (5.11) and (5.12) are shear forces at finite element patches, they must be integrated over the entire glass surface to calculate the total shear force acting on the glass.

5.3 Gravity force equations

To use gravity as an actuation method, the entire bearing assembly must be clamped together and tilted as a whole. Since the gravity vector is always downward, the lateral force exerted on the glass sheet is

$$F_{lateral} = m_{glass} * \sin\theta \tag{5.13}$$

which, for small angles, can be simplified to

$$F_{lateral} = m_{glass} * \theta \tag{5.14}$$

Although a proper comparison and study should have been done of the two actuation methods, the gravity method was not conceived until the final device (version 2.2). Hence all prototypes up to that point were focused on developing shear force actuation.

5.4 1D shear testing device

The first step in developing position control with shear force was to attempt position control in only one dimension. A simple device, shown in Figure 5.2, was created for this purpose.

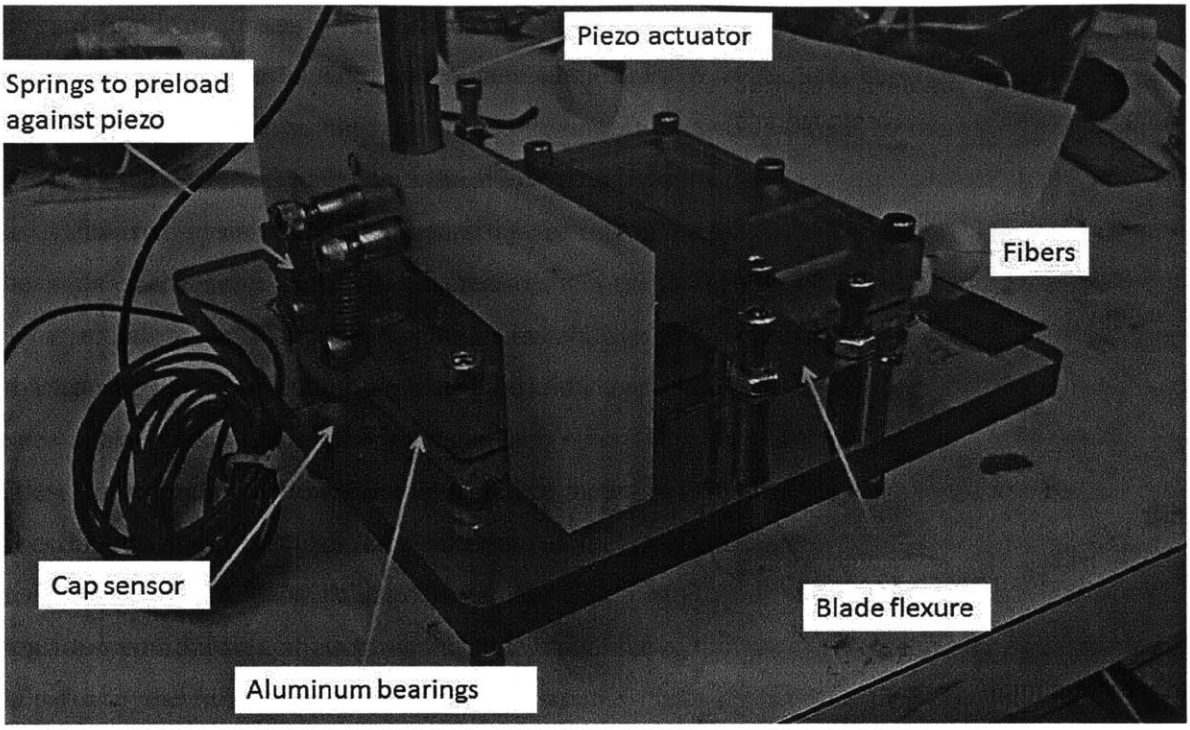

Figure 5.2: 1D shear testing device

For these experiments, a 120 mm x 100 mm x 0.46 mm rectangular sheet of glass was used, and was physically constrained to move in only one dimension, the x-axis (the z-axis is vertical). The bearings were machined out of porous aluminum. The top bearing is held by a blade flexure that allows rotation about the y-axis and translation along the z-axis. Adjustment screws tune the translation along the z-axis, thereby also setting the bearing gap. The same piezo actuator used in Husseini's design is reused to actuate the rotation of the bearing about the y-axis. A cross-sectional view of the device is shown in Figure 5.3.

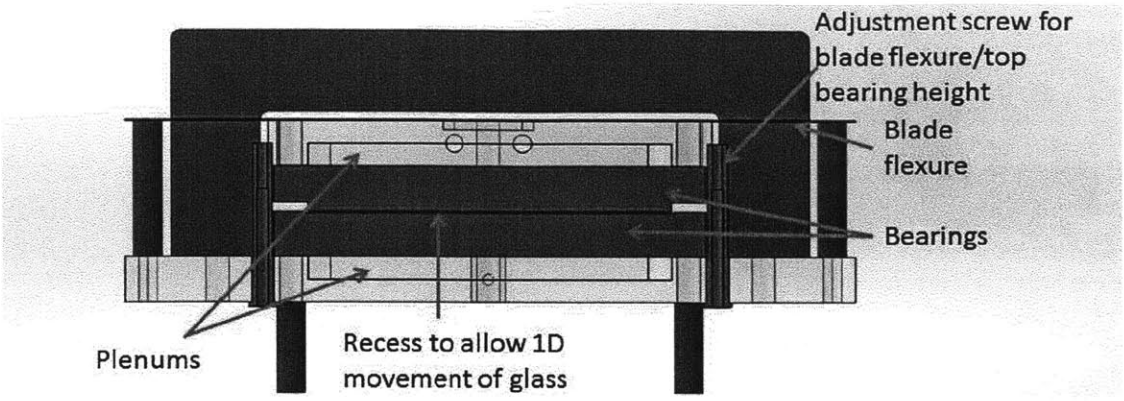

Figure 5.3: Solidworks cross-sectional view of 1D shear testing device

A single fiber assembly as described in chapter four is used to sense the position of the glass. The position data is fed to a simple PI controller, which outputs to the piezo actuator. The same National Instruments Data Acquisition devices used in Husseini's design are reused to input and output data.

The tests were a success, as the device was able to position the glass to +/- 2mm of the desired position. There was some stiction since the glass was scraping along the guide walls as it slid back and forth along the x-axis. Additionally, the sensor was very noisy due to the non-uniformity of the glass edge. The program was run at 5Hz in order to average samples over a large period. This helped reduce the noise, but did not eliminate it enough to be able to add a differential component to the controller.

5.4.1 Attempting to empirically determine angle-shear relation

Experiments were done to try to determine the relationship between angle and magnitude of shear force. This was done with the same 1D shear testing device with a simple add-on for force measurement, which consisted of a thin strip of sheet metal with a strain gauge glued on using a cyanoacrylate adhesive, as shown in Figure 5.4.

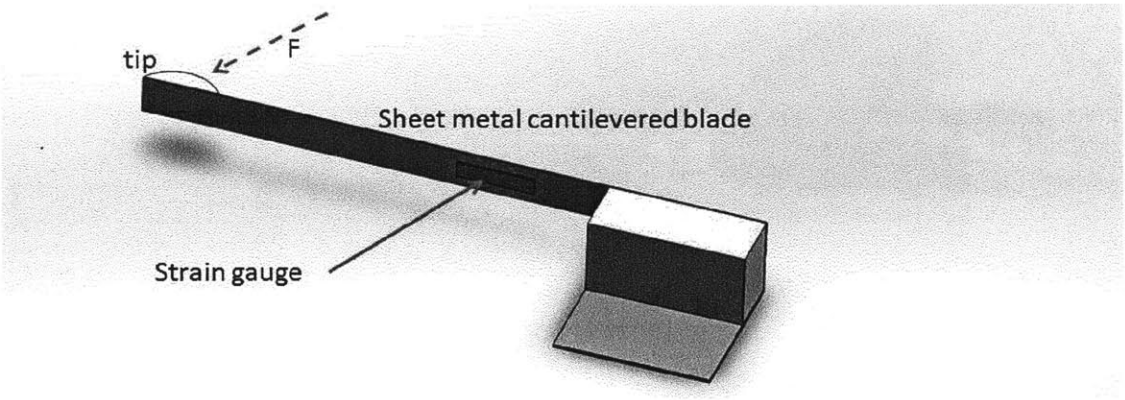

Figure 5.4: Force measurement add-on.

This add-on uses the same principle as a load cell. As force on the tip of the sheet metal forces the strip to bend, the strain gauge stretches and changes resistance. The strain gauge is used as part of a Wheatstone bridge, which is configured as in Figure 5.5. As the resistance of the strain gauge changes, the voltage across it also changes, creating a voltage difference across the bridge. The greater the force on the tip, the greater the voltage difference is seen across the bridge. This relationship is linear and can easily be calibrated by incrementally loading the sheet metal strip with larger weights and recording the voltage.

Load cells are meant to measure relatively large weights. Because fluid shear force is expected to be small, the force sensor had to be made to be able to detect very small changes. Various thicknesses of aluminum were tried for the sheet metal strip, eventually settling on 0.254mm (0.01"). Any thinner thicknesses resulted in the strip flexing under the weight of its own tip, which was only 0.5g in weight.

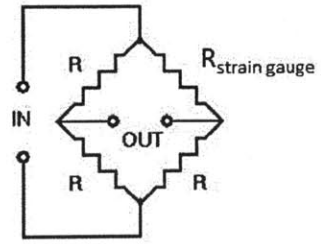

Figure 5.5: Wheatstone bridge configuration.

The force sensor was attached to the device and the angle between the aluminum bearings was actuated to produce increasingly large shear forces. However, the force was so miniscule that only a 0.1mV difference registered on the multimeter at the highest angle possible, which was close to 1°. At that scale, the uncertainty of the force sensor is on the same order (due to buckling under its own weight), and therefore connecting the sensor to a more sensitive data acquisition device would not help much. Further pursuit of the experiment was deemed impractical and the focus shifted to the next step, which is the 2D shear testing device.

The experiments did provide a general sense of the scale of the shear force, which was important in limiting what was thought to be possible with shear force. For example, one concept for non-contact slumping was to place the glass in between two angled but near-vertical bearings. The vertex of the angle would point downwards, thus providing a shear force upwards. If the shear force proved to be strong enough, the shear force on the glass would balance the gravitational force on the glass, keeping it afloat. However, the experiments proved that shear forces are miniscule in comparison.

5.5 2D shear testing device

As was mentioned in section 4.3, for two-dimensional position control, the glass shape was changed from a rectangular to a round shape of 150 mm diameter and 0.5 mm thickness. Two optical sensors placed orthogonally measure the rough location of the glass in the x and y axes. This position data is fed into PI controllers that control two separate piezo actuators, one for each axis.

The device, shown in Figure 5.6, is divided into two subassemblies, top and bottom. The bottom subassembly holds the fibers for the optical sensors, the bottom bearing, three capacitance sensors, and the bottom halves of a three groove kinematic coupling. The three capacitance sensors are placed at the vertices of an equilateral triangle and provide the bearing-to-bearing gap data.

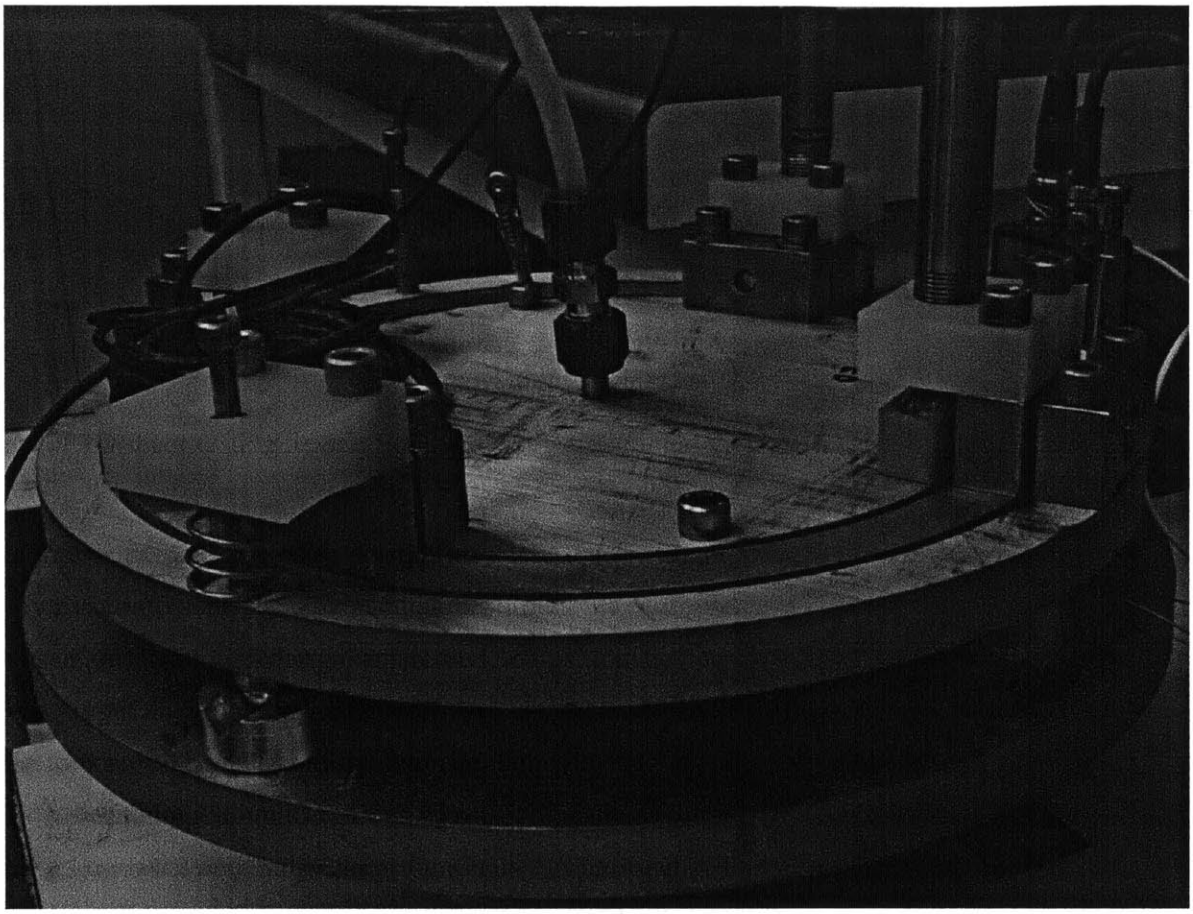

Figure 5.6: 2D shear testing device.

The top subassembly uses two nested rotary shafts and ball bearings, similar to a gyroscope toy, to provide the degrees of freedom necessary. The outermost ring of the top subassembly holds the top halves of the kinematic coupling, which are screws with acorn nuts screwed onto the ends. Turning the screws provides adjustability of bearing-to-bearing gap. While the bottom bearing is just round, the top bearing is round with three tabs spaced equally around its circumference to provide reference surfaces for the capacitance sensors. The bearings are again machined out of porous aluminum. Figure 5.7 illustrates exaggerated kinematics of the top subassembly, while Figure 5.8 shows a Solidworks cross-sectional view of the complete assembly.

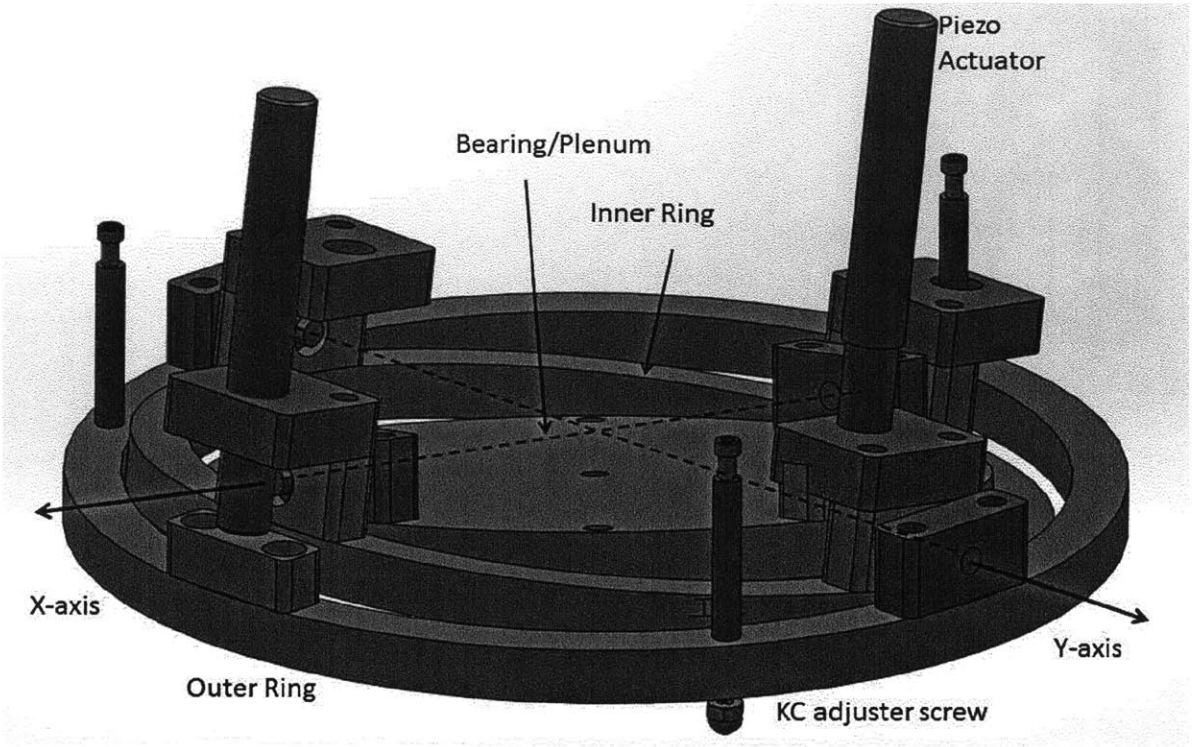

Figure 5.7: Top sub-assembly with exaggerated motions.

To set the bearing-to-bearing gap, the screws with the acorn nuts are adjusted until the acorn nuts no longer contact the groove kinematic couplings, at which the two bearings are flush with each other. The readings from the capacitance sensors are used as the "zero" offset. Then the screws are adjusted until all three capacitance sensors read close to 550 μm, which is the bearing thickness (400 μm) plus 100 μm between the glass and each bearing. Then the glass is inserted and the PI controller takes over.

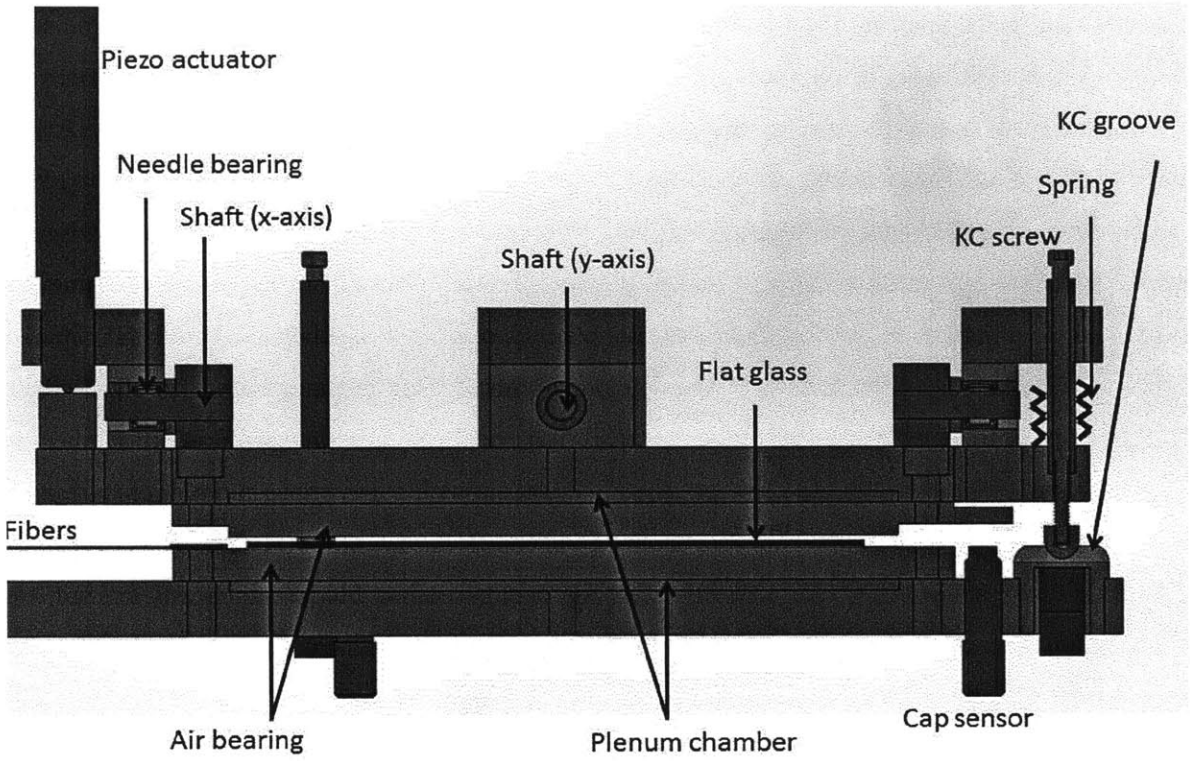

Figure 5.8: Solidworks cross-sectional view of 2D shear testing device.

5.6 Control and System identification

For the PI controller to be at its most effective, the bottom bearing must be leveled to be close to perfectly horizontal. Otherwise, there is always a relatively large gravity force component affecting the glass. This is done with a precision Starrett level before the top subassembly is placed on top.

Again, due to a noisy signal, the system was run at 5 Hz with sample averaging. The optical sensors had more noise than with the 1D shear testing device due to the curvature of the edge of the glass. It is easier to make better quality straight edges than it is to make curved edges. The differential term for the controller was again omitted. Attempts to control the system at 10 Hz and 20 Hz were unsuccessful due to the signal noise.

5.6.1 Frequency Response

System identification, or measuring the frequency response, was done on one of the axes of the device. System identification is the process of adding a sinusoidal input to the output of the PI controller and measuring the magnitude and phase of the response of the system. A 3 micron-amplitude sinusoidal signal applied to one piezo actuator, while the other axis was undisturbed. The measured transfer function is the ratio of the total signal (sinusoid plus PI compensation) to the piezo, to the distance from the glass edge to the fibers. Since the PI output to the piezo is directly related to the bearing-to-bearing angle, the measured transfer function can also be considered as the ratio of the bearing-to-bearing angle to the distance of the glass edge from the fibers. The transfer function of the controller was divided out from the measured transfer function to produce the Bode magnitude and phase plots shown in Figure 5.9.

Because of the slow loop time of 5 Hz, there is a large time delay, which acts as the following equation:

$$G'(s) = e^{-sT}G(s) \tag{5.15}$$

Where *G'(s)* is the measured transfer function, *G(s)* is the transfer function of the system, and T is the loop delay. In the case of 5 Hz, $T = 0.2$ s.

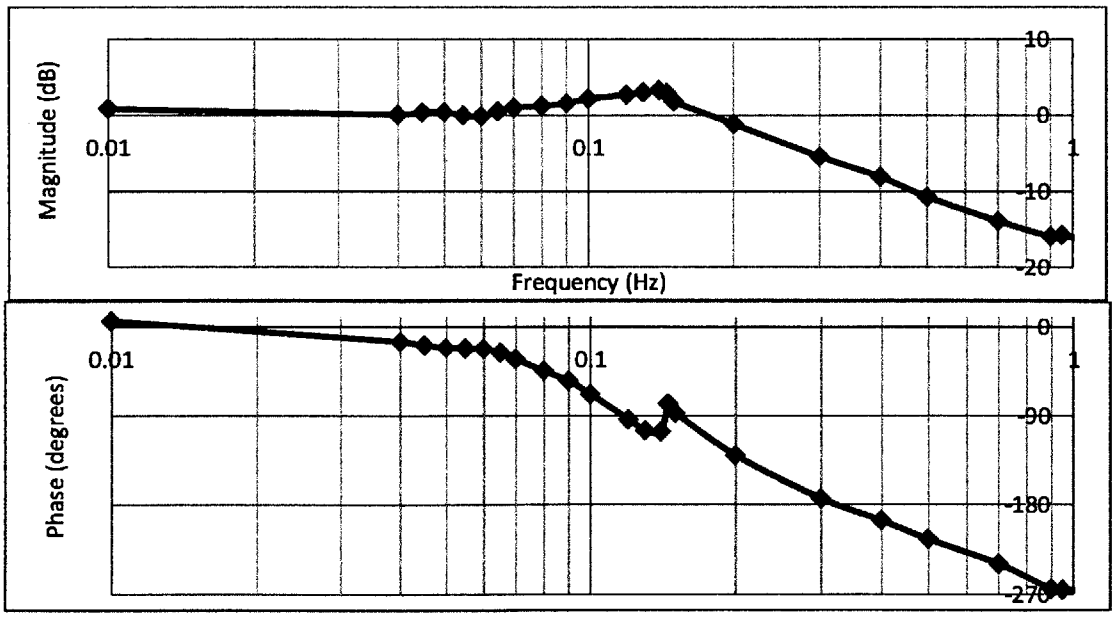

Figure 5.9: Magnitude and phase plots of plant transfer function.

As expected, the glass and shear force actuation is a slow system, and does not respond to high frequency inputs. The Bode plots appear to indicate two poles at about 0.15 Hz. It is unknown what the reason is for the spike at 0.15Hz in the frequency plot. It may be that there is a resonance at that frequency either from the glass and/or air flow. More/better data is needed to fit the system to a model.

5.6.2 Optimal controller

Because shear force applies acceleration to the glass, a traditional proportional controller is not the optimal controller. A proportional controller which takes the position of the glass will give a higher output when the glass is farther away from the set-point and a lower output when the glass is close to the set-point. However, when the glass is close to the set-point, it most likely has some momentum built up while, when the glass is far from the set-point, it is likely that it has used up its momentum.

A better controller would implement a momentum compensator, where an output proportional to the velocity is added to the regular position proportional controller. This is the same thing as the differential term of a complete PID controller, which was unusable due to signal noise. However, with enough signal smoothing, such as a low-pass filter or a moving average, an appropriate set of parameters (moving average sample size, loop rate, differential gain) can be chosen such that the differential term helps instead of adding more chaos. In chapter 6, such a controller is implemented via using a moving average to smooth the signal sufficiently.

Theoretically, the best controller would also use acceleration of the glass, given that the signal is clean enough. Since the acceleration is what is proportional to the bearing-to-bearing angle, the optimal controller would use acceleration of the glass for the proportional term and velocity (momentum) for the integral term to keep the glass still. Then a bit of non-PID based impulses would be applied to move the glass to the desired position. However, that would require taking a double derivative of the optical signal, which is already noisy enough to make adding a derivative term difficult.

As previously mentioned in chapter 4, there is also the parasitic error between the two axes. Although the sensors can approximate the position of the glass up to +/- 5 mm offset from each axis, there is sufficient error to force the glass to oscillate in a circular path.

Due to the non-optimal controller and the nonlinearities in the system, the glass was only controllable to +/- 3 mm from its set points. While ideally, the position of the glass should be controllable to within +/- 0.5 mm of its set point, it is not required for slumping. For the purposes of slumping, the position only needs to be controlled to the point where it will not hit any physical barriers, which will induce ripples in the glass. Additionally, it is posited that the dithering of the position will actually aid in shaping the glass by averaging the imperfections of the bearings. Therefore, the shear force actuation method was deemed adequate and the steps were taken to create a final device, which is described in chapter 6.

It should be noted that control should be significantly improved for curved glasses. The future cylindrical and hyperbolic glasses will be slumped with the curvature pointing downwards. This will add stability in one dimension and also will likely prevent rotation of the glass while slumping. In addition to only have to control the glass in a single direction, the reference edge will be straight instead of curved, significantly decreasing signal noise.

CHAPTER

6

DESIGNS 2.1 & 2.2

To clarify, Akilian's vertical slumping tool was the first generation non-contact slumping device (1.0). Then Husseini's design led into the second generation of tools, which use horizontal non-contact slumping. Thus his design is designated as 2.0. The next two devices, developed by the author, are designated as 2.1 and 2.2, since they are both horizontal tools.

6.1 Device 2.1

The following lists the general functional requirements of a high temperature slumping device.

1. The device must be operable in high temperature without failure since the oven is thermally cycled up to 600°C.
2. The device must be able to maintain a desired gap, or stay within a tolerable range. A non-steady gap will affect repeatability of the slumping process. Too small of a gap will cause the glass to contact the bearings, and too large of a gap will decrease the stiffness of the bearing/glass system.
3. The device must be able to sense the position of the glass sufficiently to enable position control.
4. The device must be able to position the glass. No control will result in the glass resting against a solid barrier, which will induce ripples, or waviness in the glass.

After developing the custom optical sensor and shear force position control, device version 2.1 was designed. Because the idea of using gravity as an actuation method was not thought of until after device version 2.1 failed, device version 2.1 was designed around using shear force as an actuation method. Figure 6.1 shows a rendering of device 2.1. A photo is unavailable because the device was dismantled for parts before a photo was taken.

Although device 2.1 was unsuccessful, it is still discussed in this thesis because most of the design concepts are still valid and may be utilized in future generation tools.

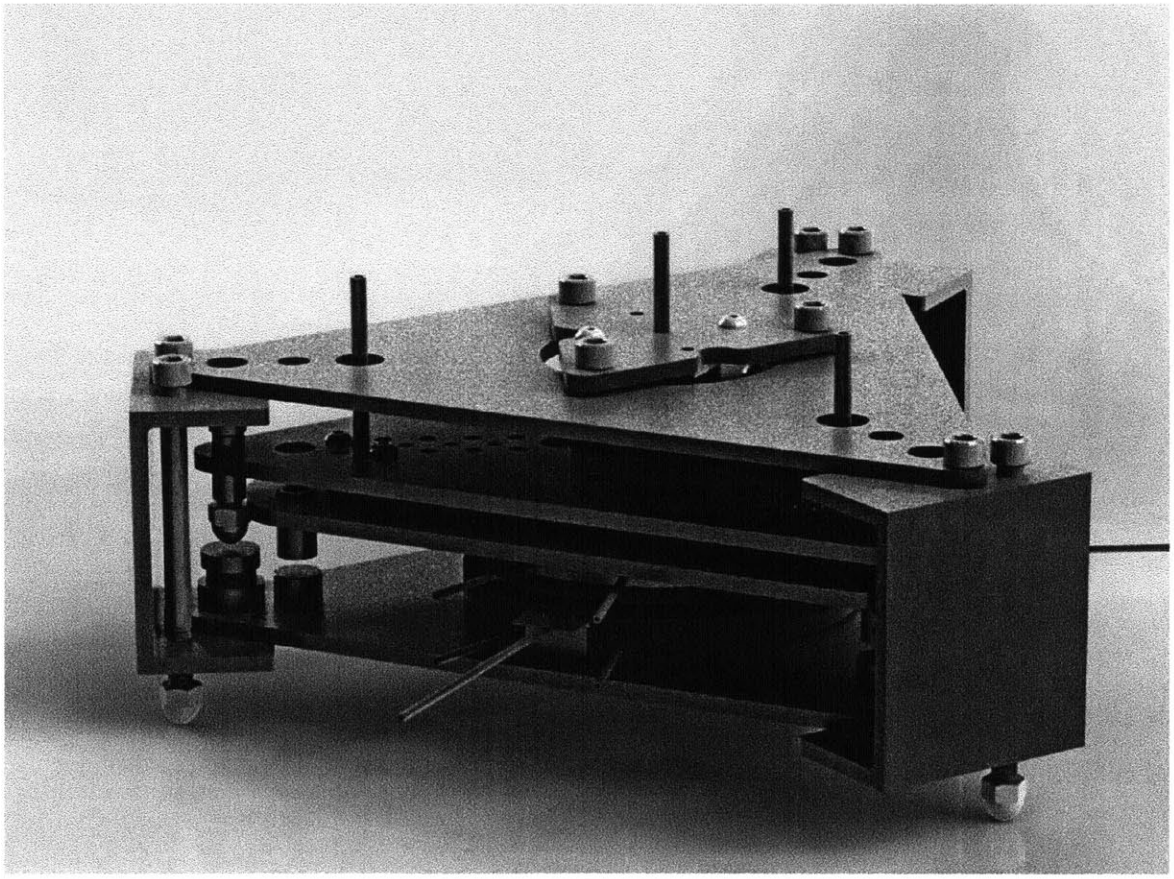

Figure 6.1: Rendering model of device 2.1

Like the 2D shear testing device, device 2.1 is also divided into top and bottom subassemblies that mate together with a three groove adjustable kinematic coupling. Figure 6.2 shows both Solidworks models of both assemblies with components labeled.

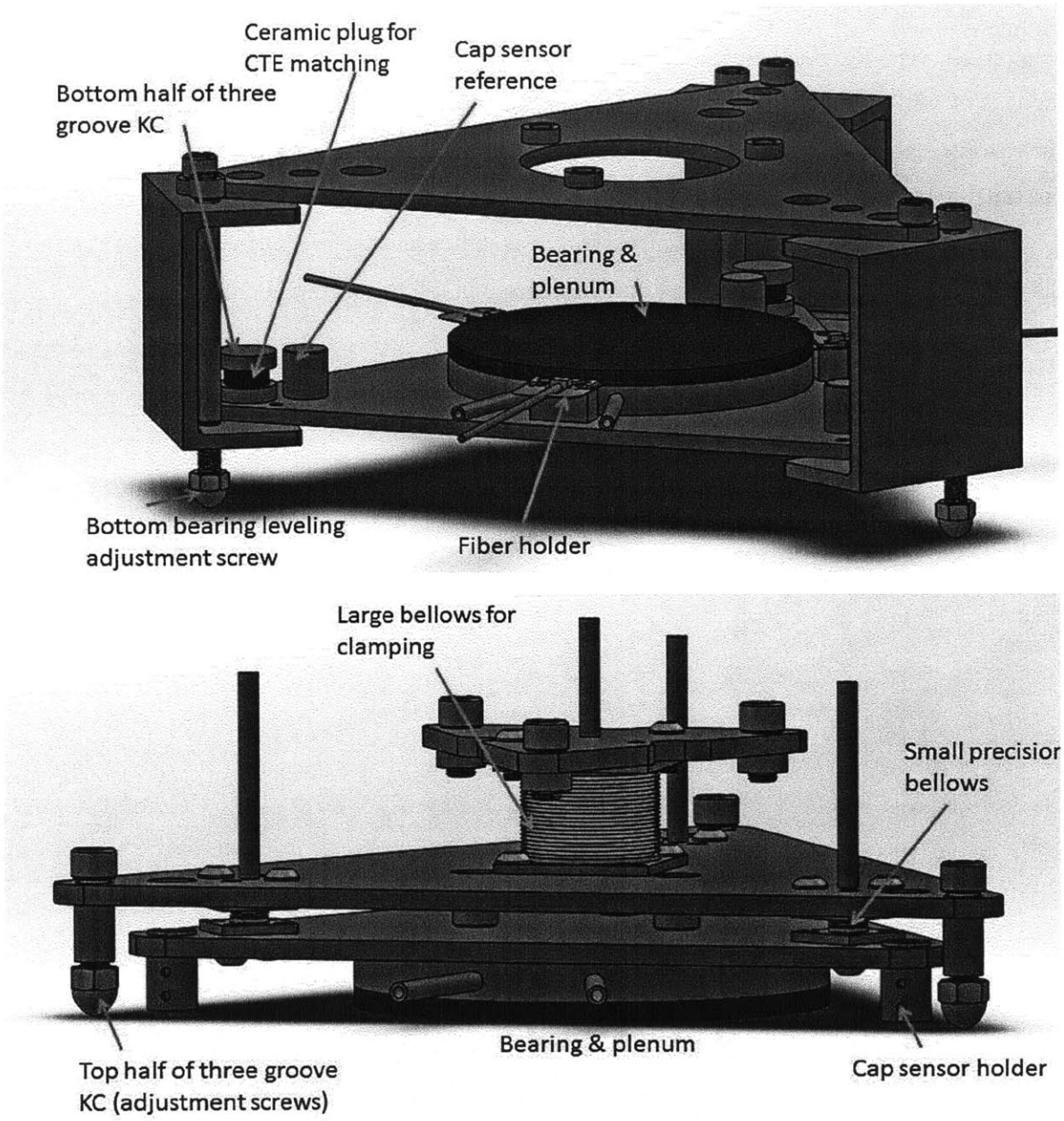

Figure 6.2: Bottom (down) and top (up) subassemblies

Device 2.1 is designed to cancel out any thermal expansions in the z-direction. This is done by matching the thicknesses of stainless steel and the bearing material in the bottom and top assemblies. Three small rods of the same material and thickness as the bearings are placed in the mechanical "circuit."

In order to improve the sensing capabilities and mitigate the parasitic error of the optical system, three optical sensors are used, instead of the minimum two required. The three sensors are placed in a circle, spaced 120° apart from each other. In addition to adding redundancy, this configuration has the advantage of being able to be matched one-to-one with the Inconel bellows used for actuation.

Three capacitance sensors measure the gap, which is actuated by Inconel bellows.

6.1.1 Inconel bellows

Push-pull rods that extend out of the oven expand about 10 mm at 600°C, which is difficult to compensate for. Therefore it was desired to create an actuation system that could operate within the oven. Inconel bellows provided a compact solution.

Two different sizes of bellows from BellowsTech are used. The first type is large and compliant, and is used as a high temperature clamp. The second type is small and stiff, and is used for actuation of the gap and tilt. Three of these smaller bellows are placed in an equilateral triangular configuration to actuate θ_x, θ_y, and Δz. The following table lists the functional requirements of the small bellows.

Table 6.1: Bellows functional requirements.

Bellows Property	*Requirement*	*Reason*
Material	Inconel	High temperature operation
Movement range	>100 μm	Need to be able to adjust for tolerances, thermal drifts, etc
Positioning resolution	<1 μm	Need to precisely actuate bearing-to-bearing gap
DOF	3	Two rotations, one axial translation
Cost	<$500	Lower costs are better for manufacturing

In order to achieve the required resolution, both the bellows stiffness and the air flow regulators have to be looked at. The highest accuracy pressure regulators from Omega are the IP710 series, which have an accuracy of ±0.1% of the operating pressure span. To get the maximum range of motion, the IP710-X100 was chosen, which operates from 2 to 100 psi. 0.1% of 98 psi is 0.098 psi (0.68 kPa).

The bellows can be modeled as springs, which follow Hooke's Law:

$$f_{spring} = k * x_{displacement} \tag{6.1}$$

Rearranging and substituting pressure for force, we get

$$\frac{k}{A_{bellows}} = \frac{P}{x_{displacement}} \tag{6.2}$$

To get a resolution of $\Delta x = 0.1\ \mu m$ ($3.94 * 10^{-6}$"), $\frac{k}{A_{bellows}}$ must be greater than or equal to $\frac{0.098}{3.94*10^{-6}} = 24900$. Estimating 0.05 in^2 for the effective area of the bellows, $24900 * 0.05 = 1245$ lb/in is calculated for the minimum spring constant of the bellows.

Bellows calibration was done using a custom tool, shown in Figure 6.3. Each bellows was mounted onto the tool with an IP710-X100 pressure regulator. The pressure was increased in increments, while a linear variable differential transformer (LVDT) was used to measure the expansion of the bellows. Figure 6.4 shows the calibration curves for all three bellows.

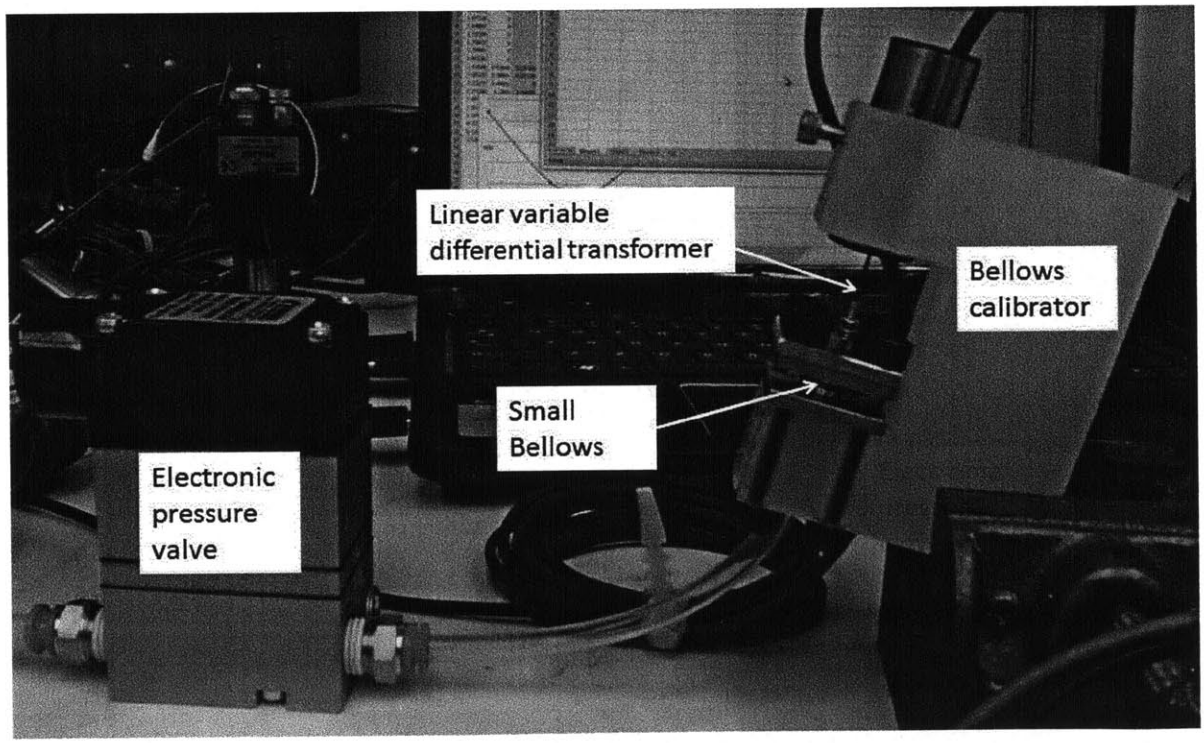

Figure 6.3: Bellows calibration tool.

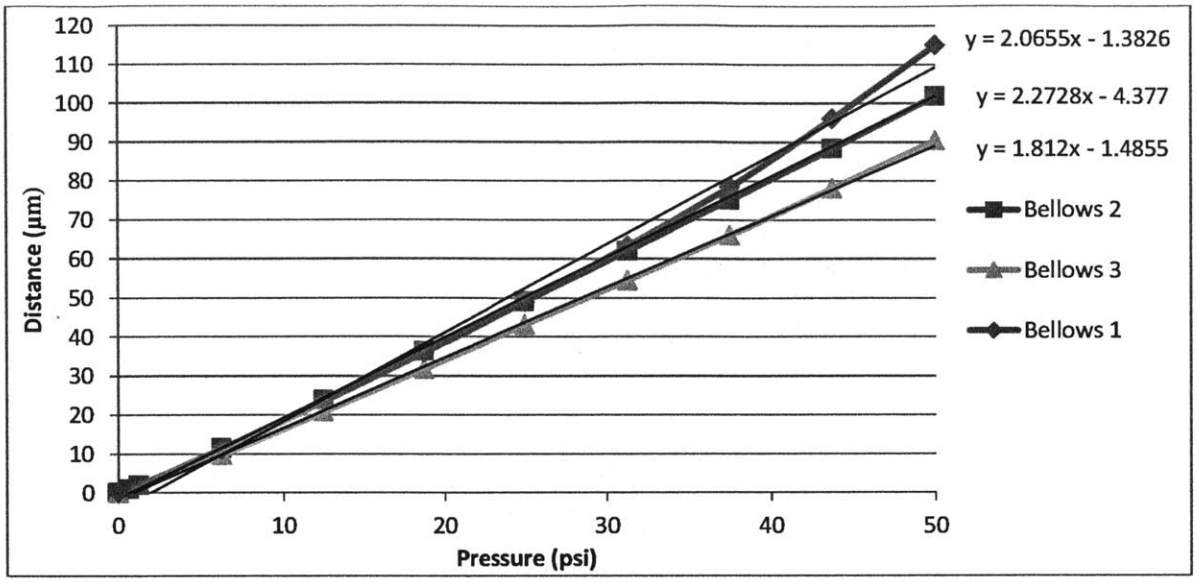

Figure 6.4: Bellows calibration curves.

6.1.2 Vacuum integrated plenums

Since the glass being shaped is round, the bearing shape was also chosen to be a simple flat round, which is the easiest shape to produce. To reduce costs further, the plenum piece was machined out of stainless steel instead of the same material as the bearing. This is possible due to the vacuum method developed in section 2.2.6. Normally, the plenum piece would be bonded to the bearing, and the disparity in material CTEs would cause large errors. However, a plenum piece with an integrated vacuum holder would be able to hold the bearing without having to be bonded to it. The vacuum holder works by suctioning parts of the bearing that have had ceramic adhesive rubbed into its pores to block air flow.

Such a plenum piece would be implemented by creating multiple plenum chambers in a single piece. One of the chambers would operate with nitrogen, and the others would operate using vacuum. Since the nitrogen and vacuum pressures oppose each other, the plenum piece has to be designed by the equation,

$$A_{nitrogen} * P_{nitrogen} + m_{bearing} * g \leq SF * A_{vacuum} * P_{vacuum} \qquad (6.3)$$

where SF denotes a safety factor to ensure that the bearing will not fall off the plenum piece during operation.

To minimize the footprint of bearing and plenum piece, the plenum piece was designed with two nested round chambers. The inner chamber uses nitrogen while the outer ring chamber uses vacuum. A Solidworks model of the plenum piece is shown in Figure 6.5.

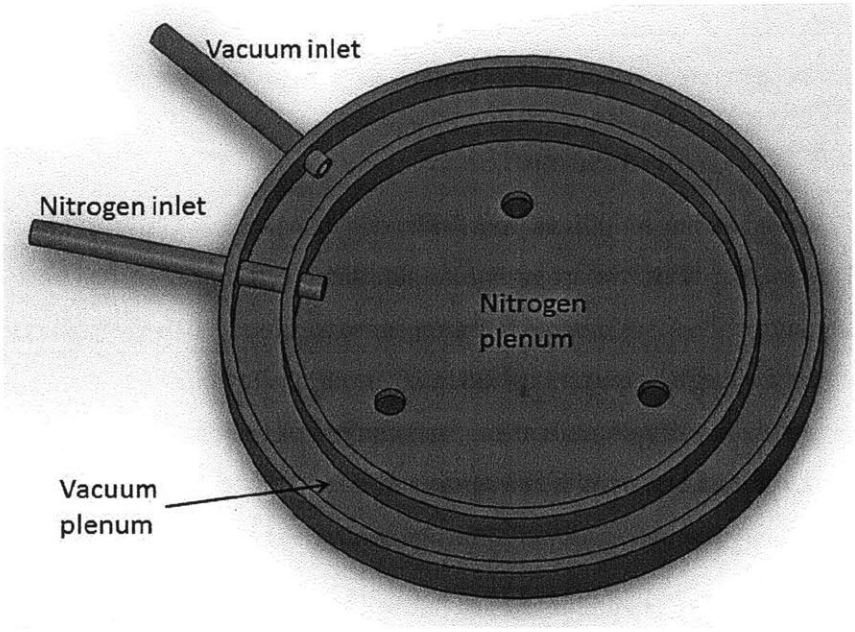

Figure 6.5: Solidworks model of double-sectioned plenum piece.

6.1.3 Bearing material

The following table lists the functional requirements of the porous air bearing.

Table 6.2: Bearing functional requirements.

Bearing Property	*Requirement*	*Reason*
Material	Porous ceramic	High temperature operation.
Flatness tolerance	<1 μm	Bearing flatness affects glass flatness. By investing in a high accuracy bearing, it will be easier to track down sources of error later.
Finish	Reflective	A reflective surface allows for easy measurement of the bearing surface flatness via optical methods.
Diameter	6"	The glass is 4" in diameter and the vacuum rim is 0.75" thick. An extra 0.5" is added to allow room for the glass to move around.
Stiffness	High	The plenum pressures will deform the bearing
Cost per set	<$2000	Lower costs are better for manufacturing.

Three materials were investigated for the bearing. The first material attempted was carbon. Although the highest temperature rated carbon oxidizes at about 450°C, NewWay Air Bearing thought that the use of nitrogen as the operating gas would be able to protect the bearing surface under high temperature operation. Carbon is easily shaped, so if carbon were viable, it would lower production costs considerably. To verify if nitrogen can protect carbon at 600°C, a small sample carbon bearing and carbon plenum were purchased from NewWay. The two pieces were bonded together using a carbon adhesive and thermally cycled multiple times while running nitrogen through the bearing. Figure 6.6 shows the results after each thermal cycle.

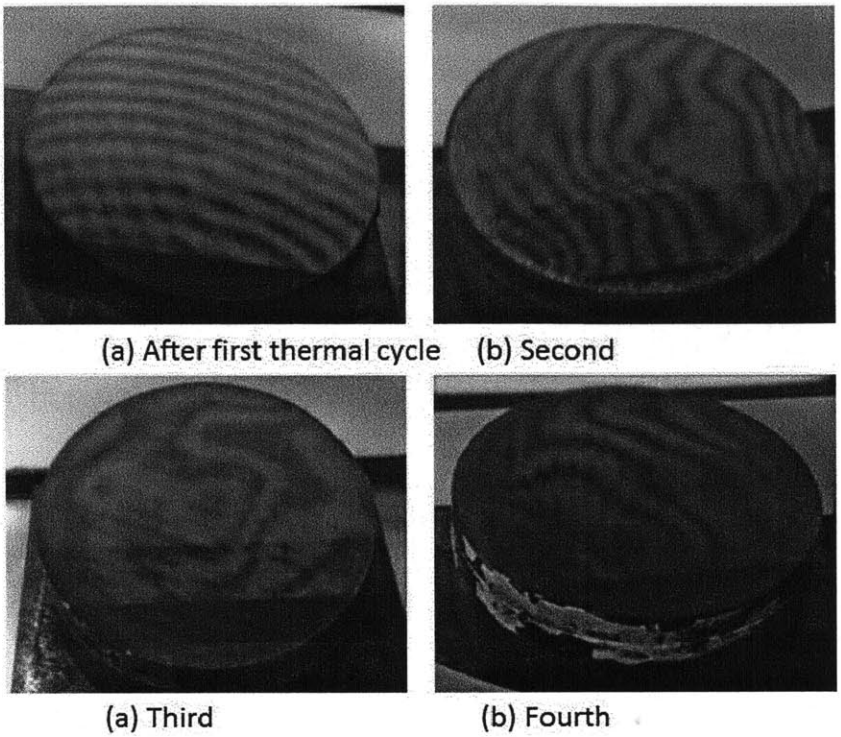

Figure 6.6: Optical fringes on thermally cycled carbon bearing surface

The fringes do not change by much after each thermal cycle. The overall flatness stays the same. However, small pock marks started to mar the bearing surface, as shown in Figure 6.7, indicating bearing damage. Before thermally cycling, the carbon had a highly reflective finish that did not survive.

Figure 6.7: Pock-marks on carbon bearing surface.

The next two materials suggested by NewWay were an A15 alumina oxide from Refractron and a silicon carbide called Invincer-Rx from Blasch Ceramics. Although silicon carbide is the superior material, bearing sets were ordered of both materials because the alumina oxide bearings could be procured more quickly than the silicon carbide bearings.

As expected, the alumina oxide bearings were rough and grainy. They were used only until the silicon carbide bearings arrived, which were smooth and reflective at an oblique angle.

6.1.4 Device failure

Device 2.1 was unable to control the position of the glass because the pneumatic actuation was too slow. The nitrogen flow lines were longer than 10 m, which adds much flow resistance. Additionally, pneumatics inherently require a relatively long time to transmit pressure. Testing the pneumatic actuation circuit revealed a response delay on the order of a second.

Another point of failure was that during thermal cycling, the stainless steel threads began to bind to each other. This is a large issue for the adjustable kinematic couplings, which have to be tuned every time the top subassembly is lifted up. A molybdenum bisulfide coating would have prevented the binding from happening, but had not been applied due to oversight.

Indirectly, the optical sensor configuration contributed to this oversight. The unfortunate consequence of the symmetrical configuration of the optical sensors was that there was no longer any room to slide the glass in between the bearings. Instead, the top subassembly had to be lifted while the glass was inserted.

After three thermal cycles, the threads were bound so tightly that the tip of an allen wrench broke off while trying to turn the screws.

The last point of failure was the capacitance sensors, which also had thermal cycling issues. The sensors themselves can withstand much higher temperatures. Unfortunately, the same could not be said for the metal sleeves for the wiring. Although initially flexible, the metal sleeves became rigid and inflexible after thermal cycling. This caused the boundary between sensor body and wire to develop stress concentrations, breaking and shorting the sensor wires.

6.2 Device 2.2

From device 2.0 to 2.1 (including all of the intermediate steps), bearing-to-bearing gap had always been a large issue. Additionally, the capacitance sensors were no longer usable, which removed the only method available at the time of sensing the gap. Therefore the only way to set the gap reliably was to go back to inserting shims between the bearings and clamping them together. The large bellows is reused as a high temperature clamp and the silicon carbide bearings and stainless plenum pieces are reused as well without the vacuum. Since the assembly is clamped together, there is no need for the vacuum to hold the bearings in place.

Since the gap between the bearings is set, shear force cannot be actuated. Instead, the bearing assembly as a whole is tilted to use gravity as an actuation force on the glass. The bearing assembly is connected to the three small bellows, which are used as high temperature joints. One small bellows is aligned with the center of the bearings and remains stationary as a pivot. The other two small bellows, which are connected to push-pull rods that extend through the bottom of the oven, are bolted on at a distance from the center and are 90° apart from each other. The reason for this placement is so that the small bellows are aligned with the optical sensors, which are also placed 90° apart from each other. The push-pull rods are actuated by

SilverPak 17D-4118S stepper motors from Lin Engineering. Figure 6.9 shows a labeled Solidworks model of the device while Figure 6.9 shows a schematic of the sensors and actuators.

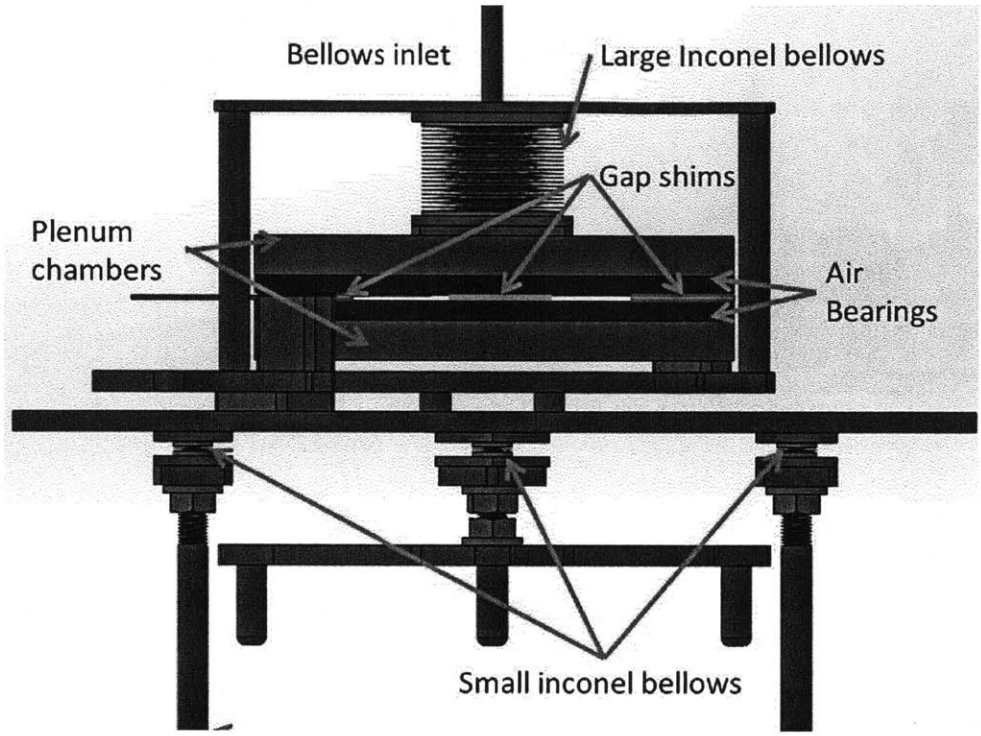

Figure 6.8: Solidworks model of device 2.2.

Initially, only two optical sensors were installed. The reasoning was that, because it worked for the 2D shear testing device, it should work for device 2.2 as well. However, two optical sensors turned out to be inadequate, and the glass would keep on getting stuck in a wrong position due to the position uncertainty error from the parasitic axes error. It is hypothesized that this is because gravity is a slower mechanism than shear force at the actuation speed of the stepper motors used. To improve the sensing a third optical sensor was installed opposite one of the original sensors, offset by 10°. The offset is because if the two sensors are collinear with each other, then the light passes through the glass and interferes with the photodiode reading of the opposite sensor. A 10° offset fixed this issue.

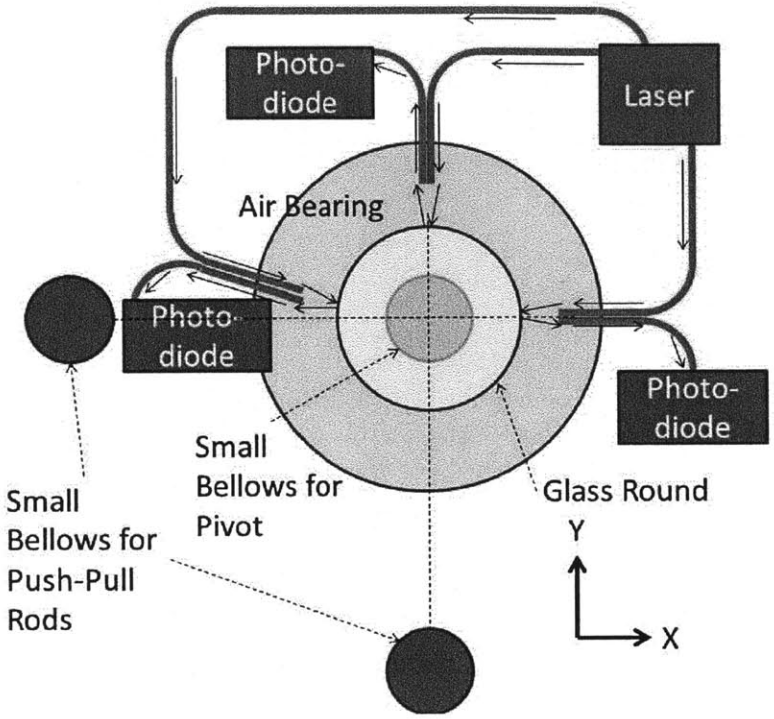

Figure 6.9: Device 2.2 sensors & actuators schematic.

For the controls, the readings from the two opposite sensors were averaged for the x-axis position. Thus even when the glass moved significantly off-axis from those two sensors, the averaging removes much of the error, since both sensors will read the same erroneous large distance, dependent on their calibrations. In addition, the difference of the two opposite sensors, multiplied by a constant, is added to the reading of the y-axis sensor to improve accuracy over a larger range.

Very low plenum pressures of around 0.05 psi were used. FMA3108 mass flow controllers and PX309-001GV pressure transducers from Omega were used as an economical solution for pressure sensing and actuation. At the pressure 0.05 psi, the flow rate measured was around 500 sccm.

Figure **6.10**Figure **6.11** shows the entire device while Figure 6.11 shows a close-up of the upper assembly. The results of slumping are discussed in Chapter 7.

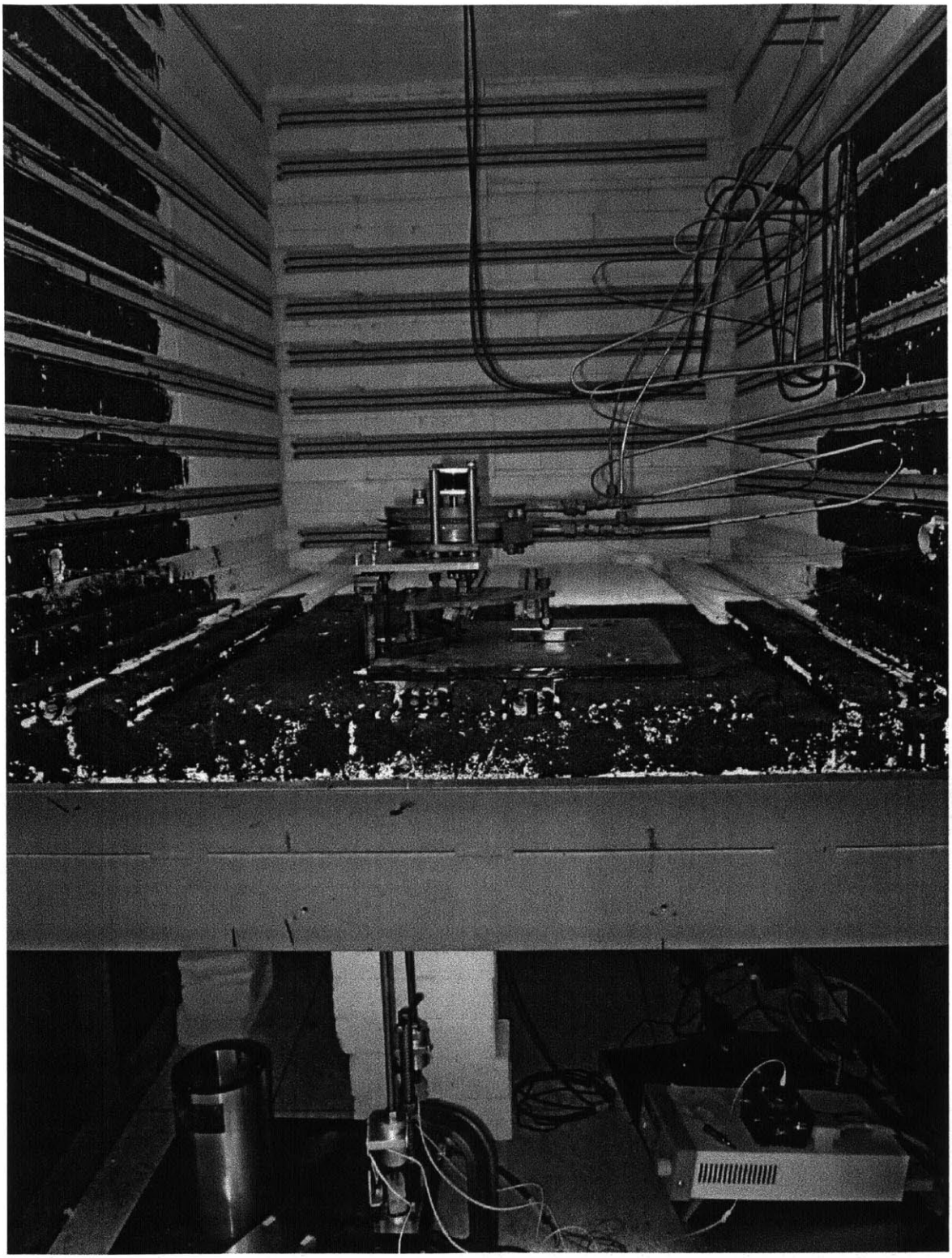

Figure 6.10: Photo of Device 2.2.

Figure 6.11: Close-up of Device 2.2.

CHAPTER

7

CONTROLLED SLUMPING

7.1 Results

Using Device 2.2, 23 samples were slumped. Of those 23 samples, the first 10 were unsuccessful due to an error in the ceramic bearings. The error was that one of the bearings purchased from NewWay had the incorrect thickness of 0.22" (the other was 0.25"). Because of the difference in thicknesses, the thicker bearing had a much higher flow resistance. At the start of each slumping cycle, the air flows in both bearings were set manually until the glass was seen to float freely. However, as the temperature increases, the gas becomes more viscous, and flow conditions change. Therefore one bearing ends up with a much higher flow rate, pushing the glass up against the other bearing with the weaker flow rate. After slumping, all 10 samples had dimples from particles and ripples from trapped flows.

A new bearing with the correct thickness was expedited from the vendor, and the subsequent 13 samples were slumped, with varying degrees of success. The samples were measured with a Shack-Hartmann tool, which was operated by Brandon Chalifoux of MIT SNL. The Shack-Hartmann tool is accurate to ± 0.5 μm. Table 7.1 lists the slumping parameters and the results of those 13 samples.

Table 7.1: slumped glass parameters

	Sample	*Gap (μm)*	*Max temp (°C)*	*Slump time at max temp (min)*	*Result P-V (μm) front or front/back*
1	G8	>50	600	6	12.3±0.5
2	Unlabeled	>50	600	60	>30 (unmeasurable)
3	G18	>50	600	6	5.9/5.2±0.5
4	G19	>50	600	6	14.0/12.6±0.5
5	Unlabeled	>50	600	60	>30 (unmeasurable)
6	G8	>50	600	6	4.8/5.1±0.5
7	Unlabeled	>50	600	60	>30 (unmeasurable)
8	Unlabeled	>50	550	60	>30 (unmeasurable)
9	G38	>50	550	6	6.4±0.5
10	G40	>50	550	6	11.3±0.5
11	G37	36±2.5	550	6	6.7/3.6±0.5
12	G38	36±2.5	550	12	10.1±0.5
13	G19	30.5±2.5	550	6	19.5±0.5

Figure 7.1 shows a rough approximation of the surface of a sample before slumping. The sample was too warped to be measured correctly. The Shack-Hartmann tool used has the limitation that it cannot correctly measure samples with greater than 30 μm of distortion. However, the general shape can be ascertained. All of the samples had similar cylindrically curved shapes, and thus only one sample is shown.

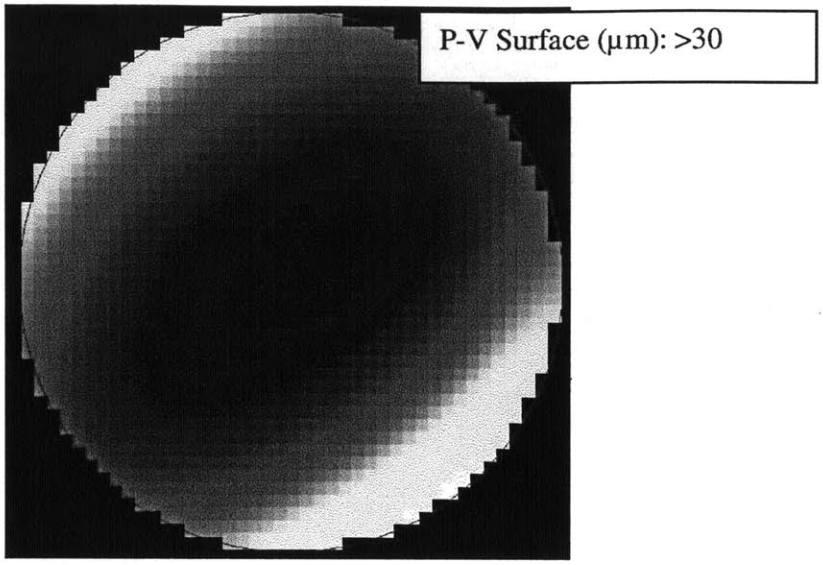

Figure 7.1: Shack-Hartmann topography of sample before slumping

Figure 7.2 shows the wavefronts of the samples used in trials 1 and 3. Trial 2 is omitted since the slump was unsuccessful.

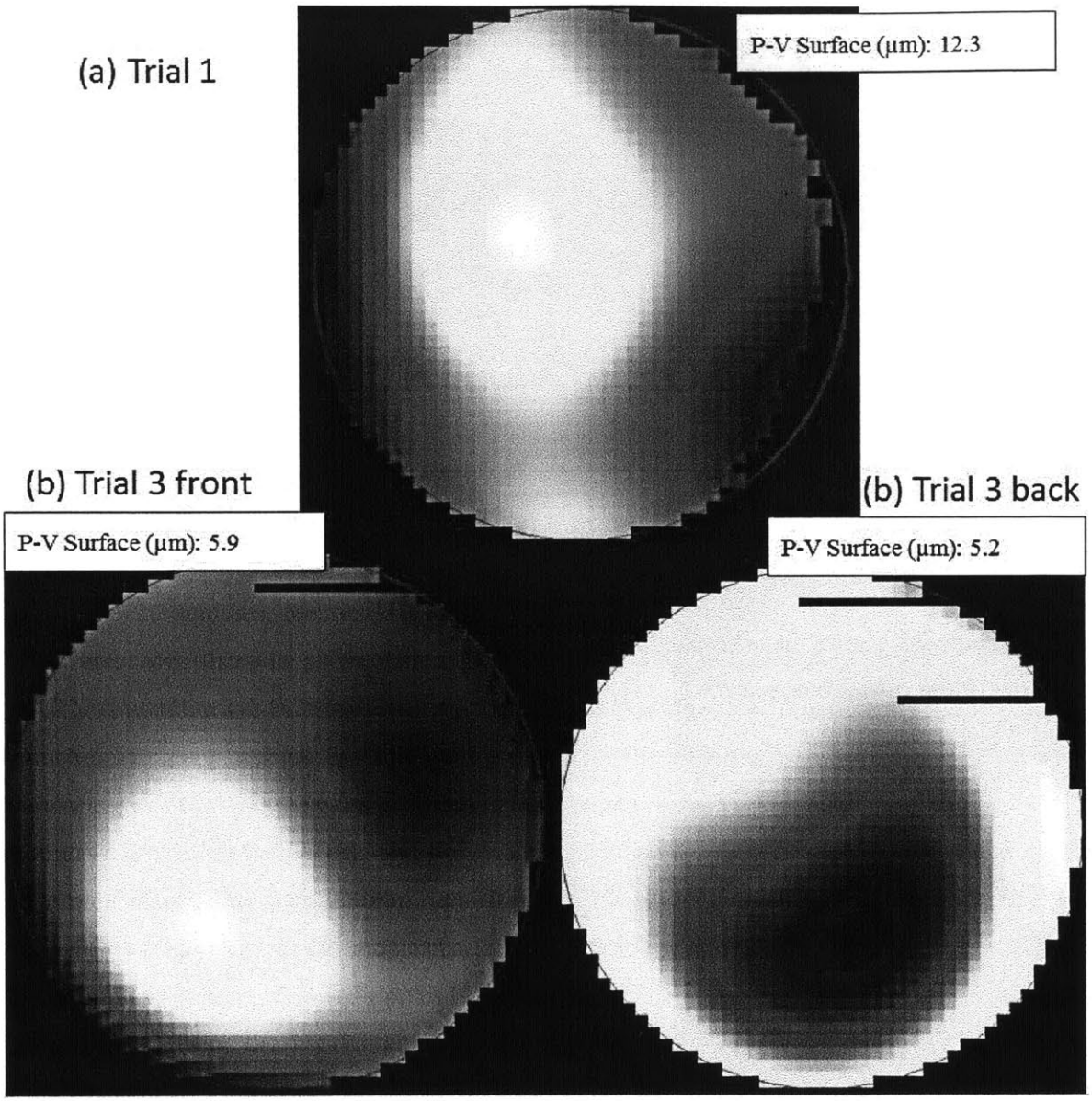

Figure 7.2: Wavefronts of samples used in trials 1 and 3.

Figure 7.3 shows the wavefronts of the samples used in trials 4 and 6. Trial 5 is omitted since the slump was unsuccessful.

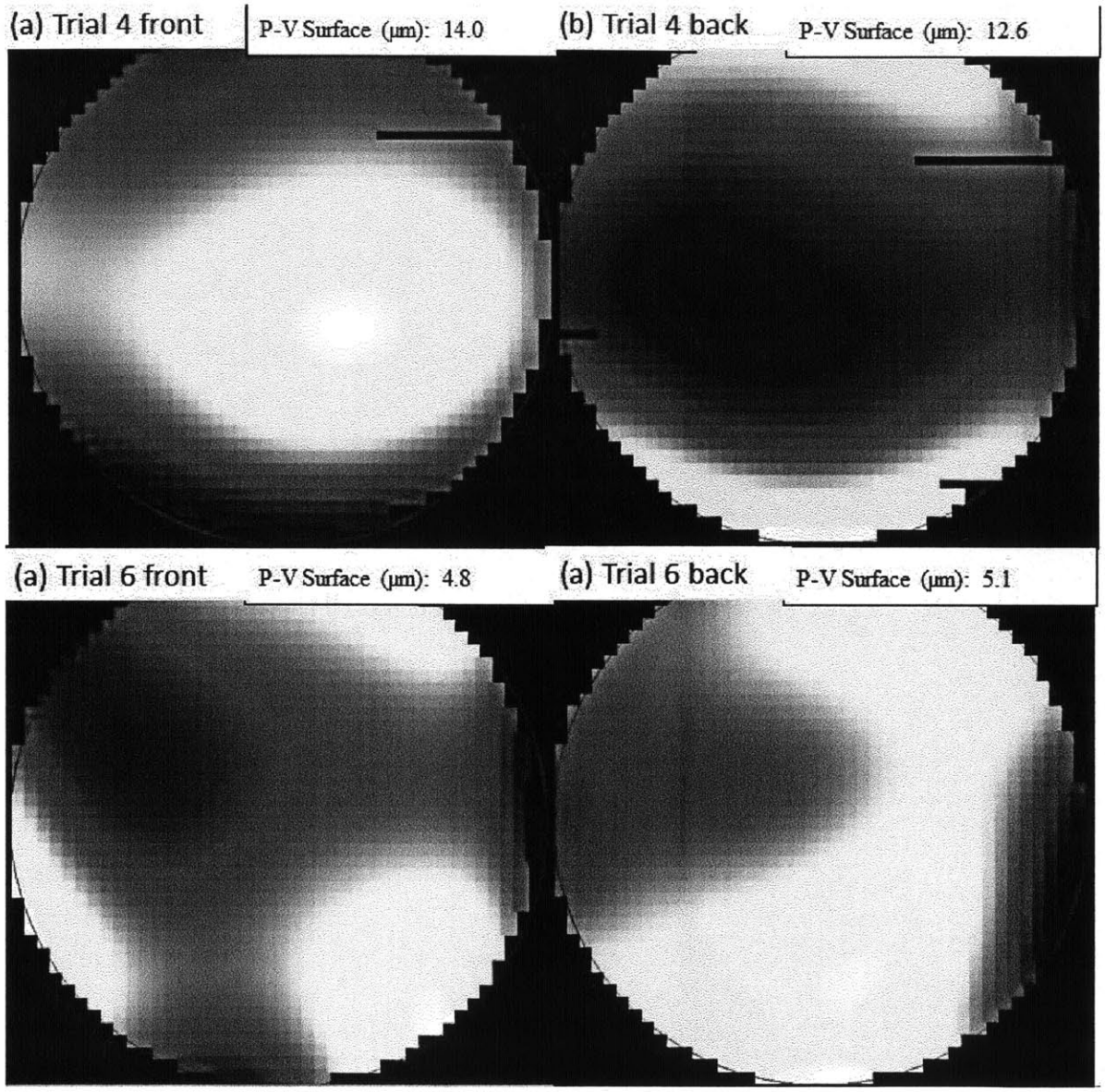

Figure 7.3: Wavefronts of samples used in trials 4 and 6.

Figure 7.4 shows the wavefronts of the samples used in trials 9 and 10. Trials 7 and 8 are omitted since the slumps were unsuccessful.

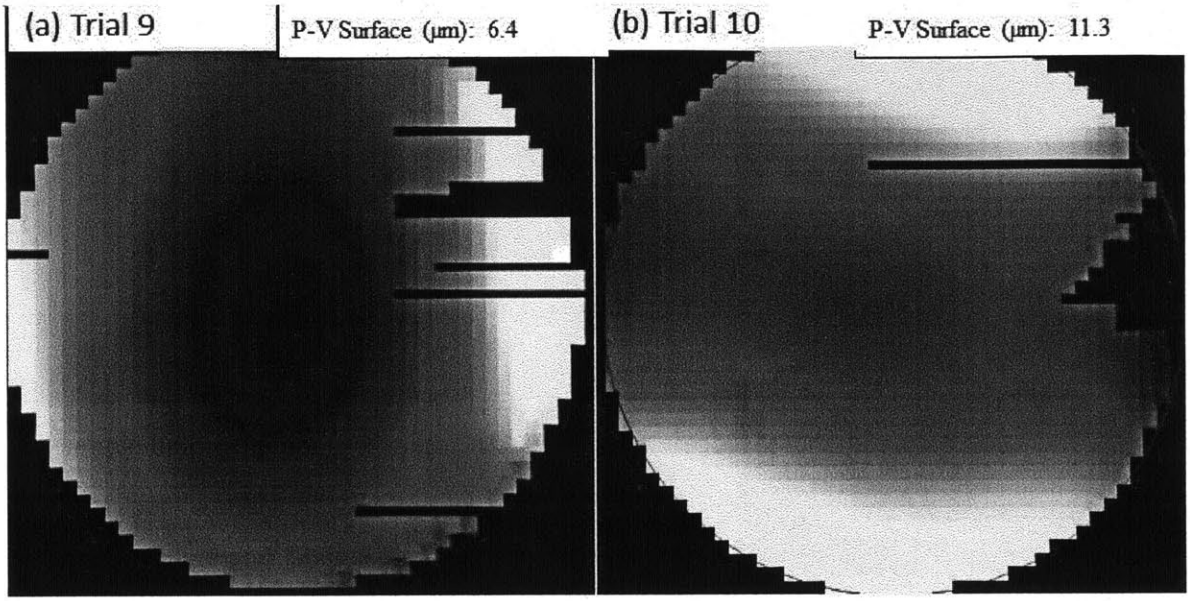

Figure 7.4: Wavefronts of samples used in trials 9 and 10.

Figure 7.5 shows the wavefronts of the samples used in trials 11 and 12.

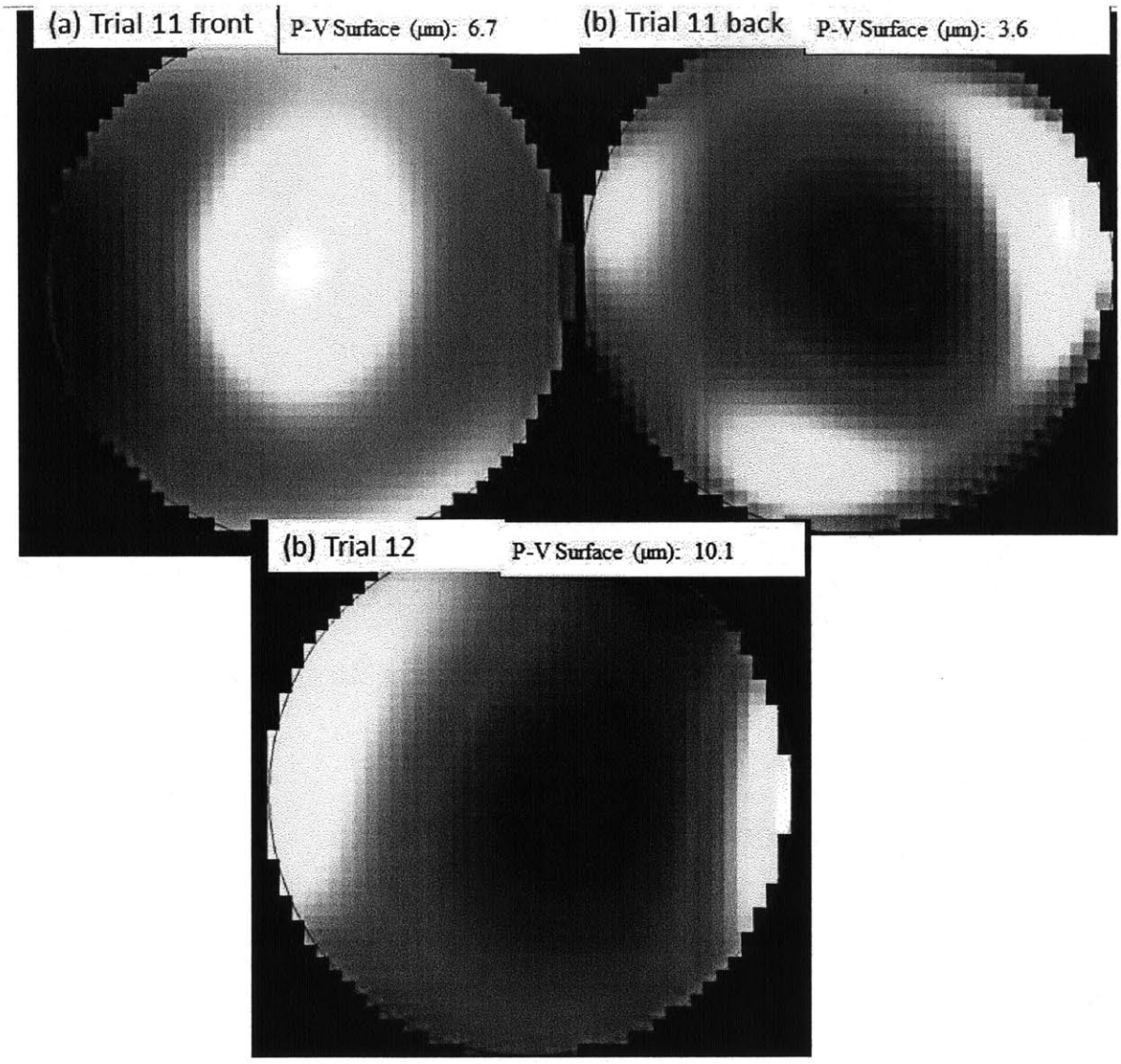

Figure 7.5: Wavefronts of samples used in trials 11 and 12.

Figure 7.6 shows the wavefront of the sample used in trial 13.

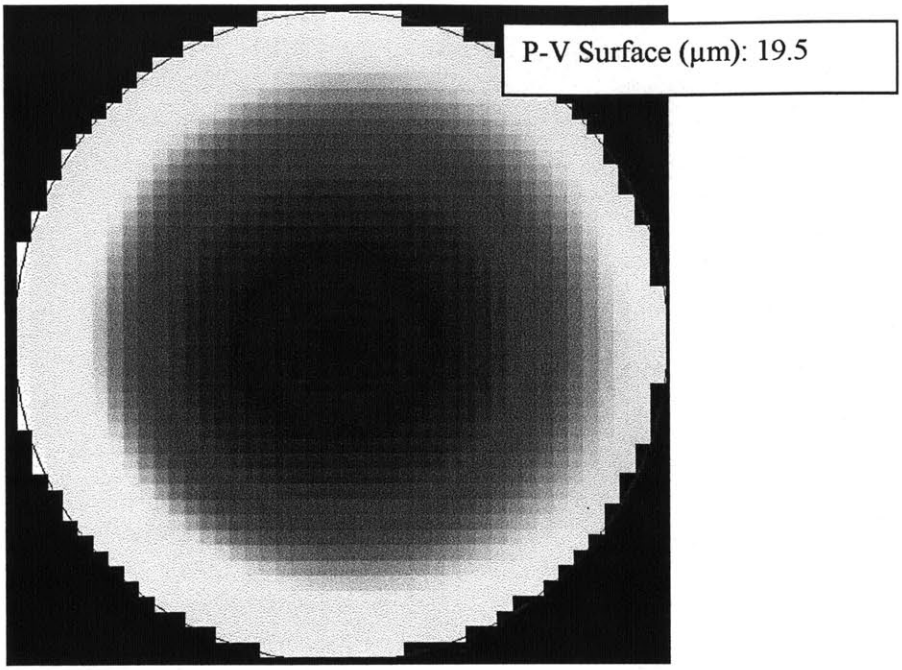

Figure 7.6: Wavefronts of sample used in trial 13.

7.2 Notes and conclusions drawn

The actual gap for trials 1-10 is unknown. This is because, while the gap was set at 50 μm, there was interference from some sheet metal parts that caused the gap to be much larger than 50 μm. The sheet metal was intended to bend elastically and not interfere with the gap, but was stiffer than anticipated due to repeated thermal cycling. To correct this, simply more compressive force was added to clamp the two bearings together with shims in between. The shims were measured with a digital micrometer with resolution of $\pm$2.5 μm.

Trials 1-7 were run at 600°C. All of the attempts with short dwell times (6 minutes) at 600°C were successful, while the attempts with long dwell times (60 minutes) failed. It was speculated that this happened because the glass is too soft at 600°C. If the glass is too soft, it may not maintain a flat shape and will instead deform to the confines of the air bearings. During the

shorter dwell times, the glass might not have had time to actually reach 600°C, thus resulting in a better surface P-V.

To confirm that 600°C is too hot, trials 8-13 were run at 550°C. All samples changed shape significantly, confirming that a lower process temperature is sufficient. In addition, trial 8 was run for 60 minutes dwell time, and also failed, similar to what happened with 60 minute dwell times at 600°C. This suggests that the process temperature can be lowered even further.

Interestingly, trials 11-13 did not result in significantly better surface P-V, even though the gap was smaller. Trial 13, especially, has the worst P-V of 19.5 μm, but also somehow resulted in a nearly perfectly symmetrical shape, which proves that the glass was floating the entire time instead of getting pinned or stuck on an edge. In addition, the symmetrical shape suggests that the worsened P-V might be the natural mode or result instead of being an exception. This seemingly contradicts the simulation done by Husseini [2], shown in Figure 7.7. However, more trials will have to be run before any conclusions can be drawn.

Specifically, the next trials would involve trying to find the optimal gap and temperature for horizontal air bearing slumping.

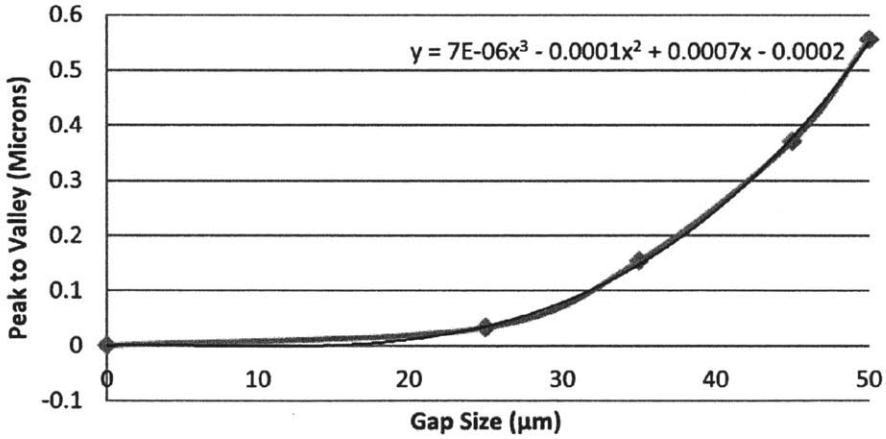

Figure 7.7: Simulation of effect of varying gap size on surface [2].

At this point, the research deadline for the 2013 NASA proposal cycle had been reached. Although the results were less than ideal (< 1 μm), they were deemed sufficient because a complementary technology for post-processing had been developed, also by MIT SNL. This post-processing technology is boron ion implantation technology, and acts on the glass in the

same way that a thermal load would. Ions are implanted into the surface of the glass, increasing the local density and causing damage-induced expansions, which can correct for low spatial frequency bows. Therefore it was decided to take the next step to improve the slumping process instead of running more trials.

Each slumping cycle requires a day to complete because of the size of the oven used. The oven has an internal space of about 3 m^3, which requires on the order of 10 hours to cool down. To eliminate the long cycle time, a new device concept was conceived, which operates without the use of an oven. Instead, a heater element is placed directly in the plenum chamber, which is heavily insulated. The new device, designated version 2.3, is explained in the next chapter.

CHAPTER

8

DEVICE 2.3 – OVENLESS WITH 30 MIN CYCLES

8.1 Process improvement

The results in chapter 7 were produced over a long period of 1.5 months after the completion of device 2.2. This is because each slumping cycle takes a long time due to the large size of the oven. The larger the oven, the longer it takes for it to cool down. The oven in question requires more than 12 hours to reach room temperature from 600°C. This limits the experimentation rate to 1 trial per day. In addition, every time the process ran into an error, which would usually happen at close to the maximum process temperature, the whole experiment would have to wait another day just for the oven to cool.

Although significant results were obtained with device 2.2, only about 10 successful slumps took place over a period of a month. To find the optimal parameters (temperature and gap) for slumping, it is foreseeable that the number of successful slumps required would be on the order of 100. This cannot be done with device 2.2.

Therefore there is much motivation to develop a device that does not require an oven and has very short heat up and cool down times. With such a device, the process time would be reduced to about 30 minutes (10 minutes heat up, 10 minutes dwell, 10 minutes cool down), and much more data could be taken quickly and efficiently.

Two strategies were attempted to achieve an ovenless design. The first strategy, which is discussed in section 8.4, used in-line pipe heaters to provide heated air to the plenums, which are thermally insulated to reduce heat loss. A photo of the initial build of device 2.3, which was based on the first strategy, is shown in Figure 8.1. Section 8.5 discusses the second strategy, which was to insert the heating element directly into the plenum chamber.

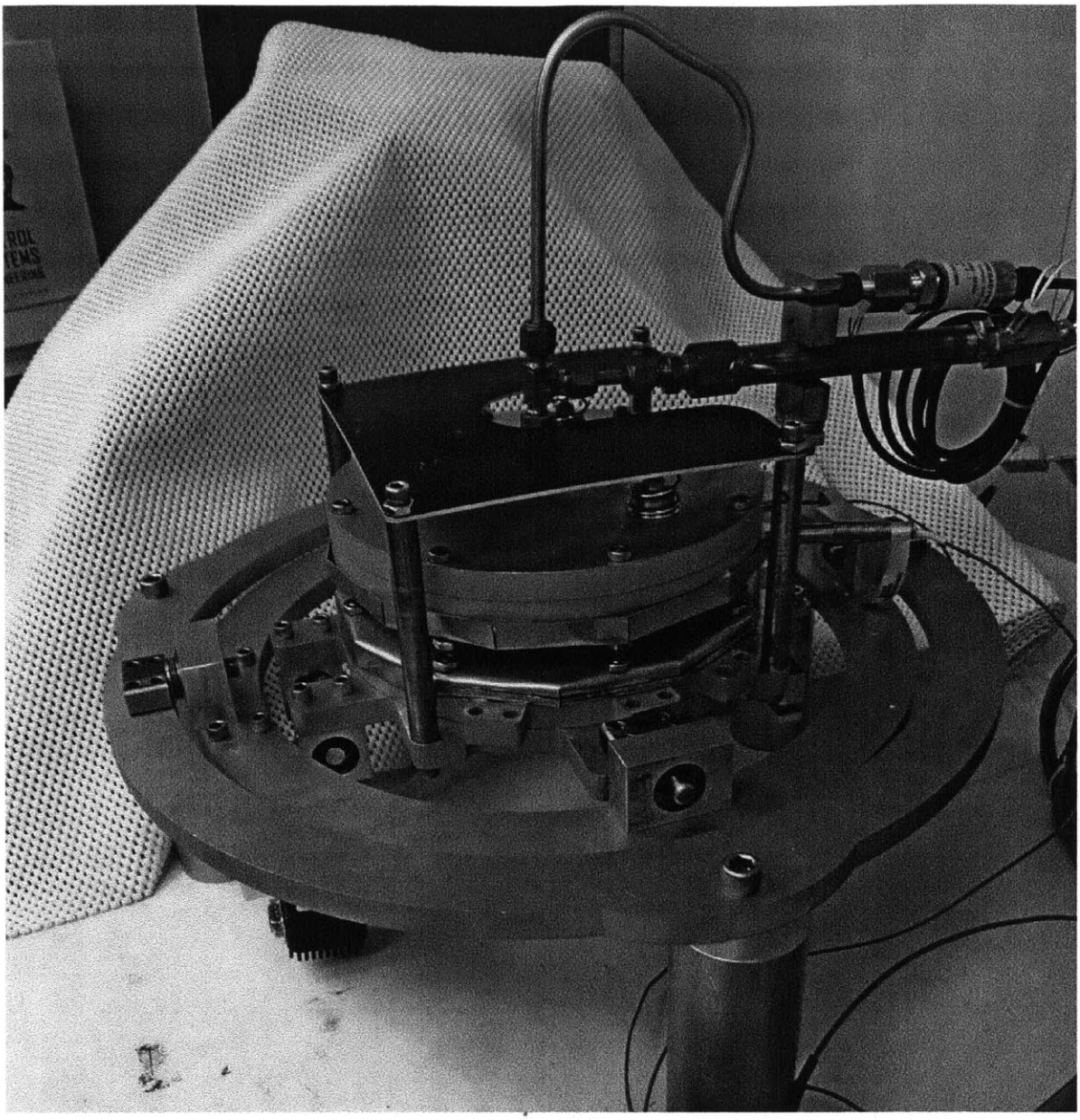

Figure 8.1: Photo of device 2.3

8.2 Mechanical Design

Device 2.3 also uses gravity to actuate the position of the glass. Similar to the 2D shear testing device, the tilting assembly consists of nested rings that rotate in the two horizontal axes,

like a set of two gimbals. The bearing assemblies are clamped together in the center of the assembly with shims in between. Each axis is preloaded with spring washers and thrust bearings.

The rotations of the rings are actuated with SilverPak 17D-4118L stepper motors, which have twice the torque of the ones used in device 2.2.

Most of the parts are made out of aluminum. The plenums and flow tubes are made out of stainless steel. Any other parts that come into contact with hot air or heated parts are made out of brass, which has a higher melting point than aluminum.

Figure 8.2 shows a labeled Solidworks model of device 2.3.

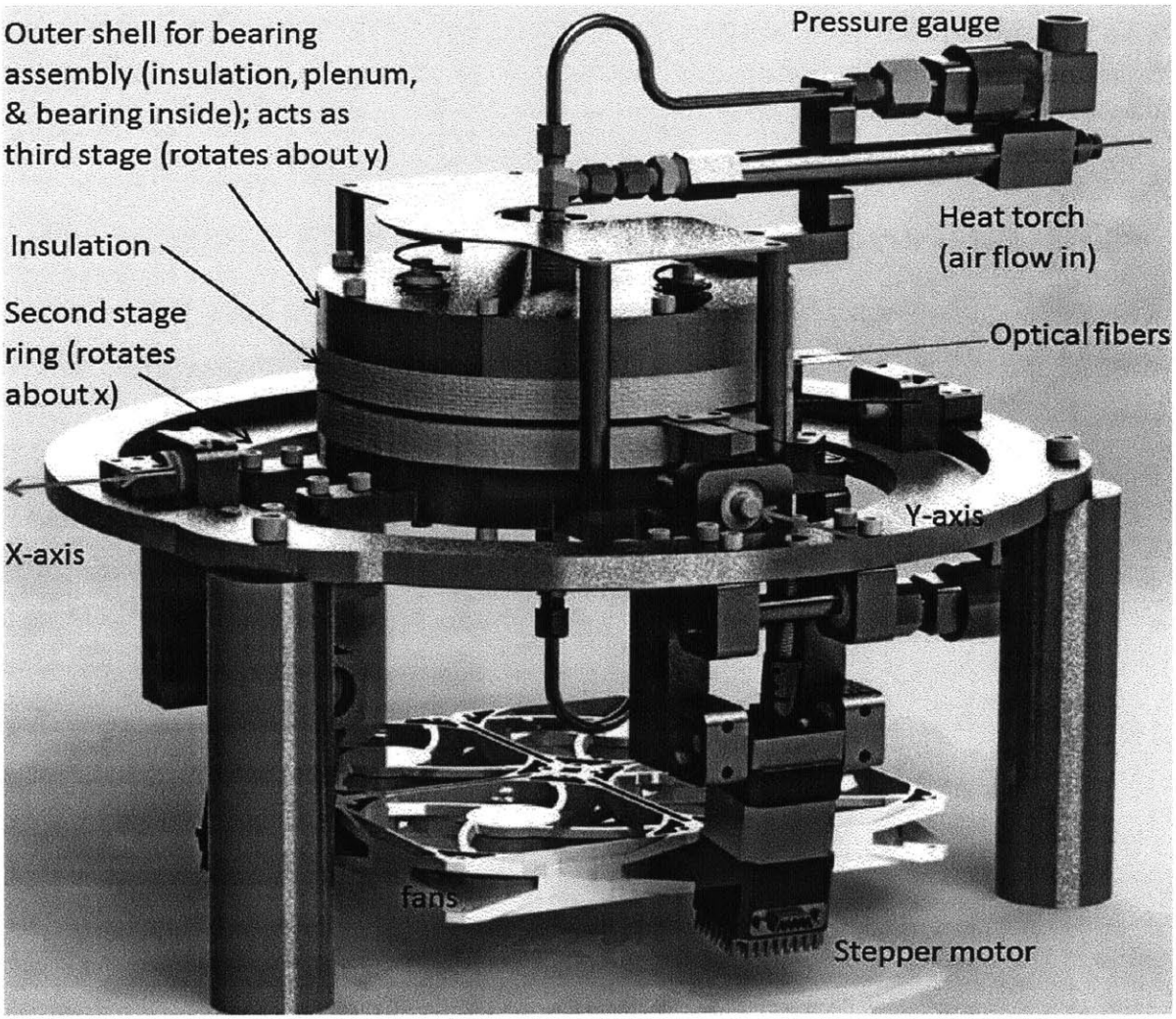

Figure 8.2: Solidworks model of device 2.3.

8.3 Optical Design

For the initial setup, the same optical setup used in device 2.2 is used. Three fiber sensors are placed at 0°, 85°, and -85°. The sensors at 85° and -85° are averaged to mitigate the parasitic axes error. The difference between the two opposite sensors, multiplied by a constant, is added to the sensor reading at 0°.

Although this setup has been proven to be sufficient, a better sensing system, which uses black/white cameras, will later be installed. A diffuse backlight illuminates the edges of the glass and the bearings. The data from the cameras is received in matrix form, and can easily be analyzed to give the position of the glass.

The cameras will not suffer from any of the limitations of the fiber sensors, and will be able to sense the glass position accurately to the resolution of the camera pixel size. This capability is now enabled because the sensors do not have to be immersed in a 600°C environment. Figure 8.3 shows the schematic of said camera sensors.

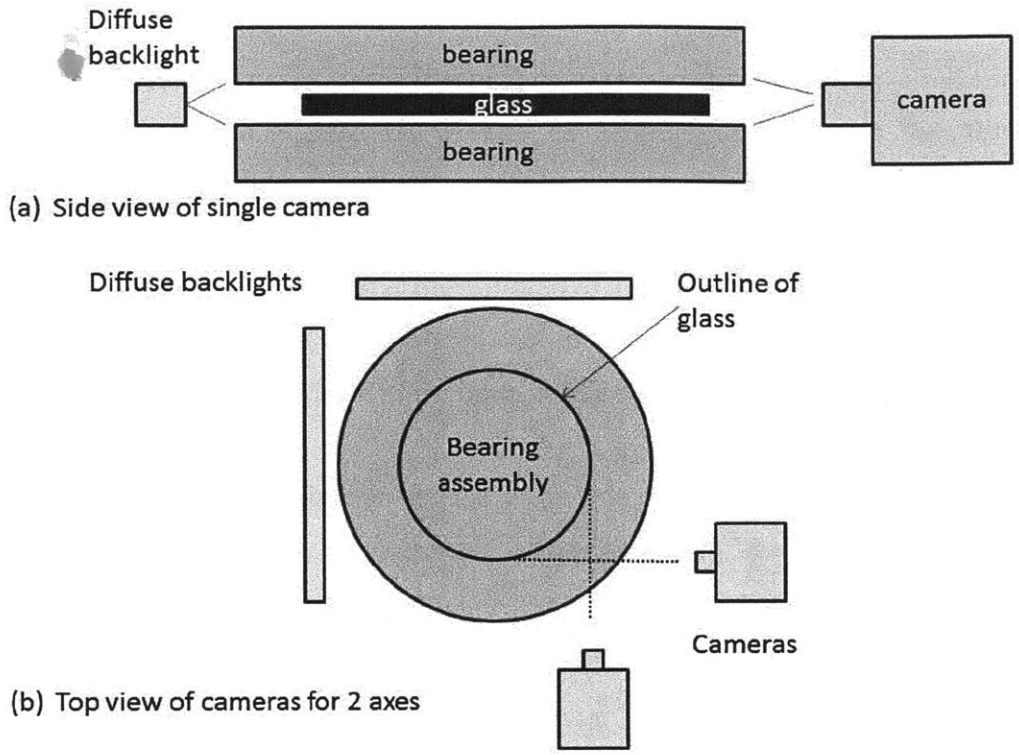

Figure 8.3: Schematic of camera setup.

8.4 Thermal Design: Inline Heaters

The flow rates used are about 500 sccm. It was quickly found that manufacturers do not sell in-line pipe heaters that can heat air to 600°C at that low of a flow rate. Industrial applications use much higher flow rates, and thus in-line pipe heaters that can be bought will overheat. To solve this, a custom in-line heater was designed and built, shown in Figure 8.4.

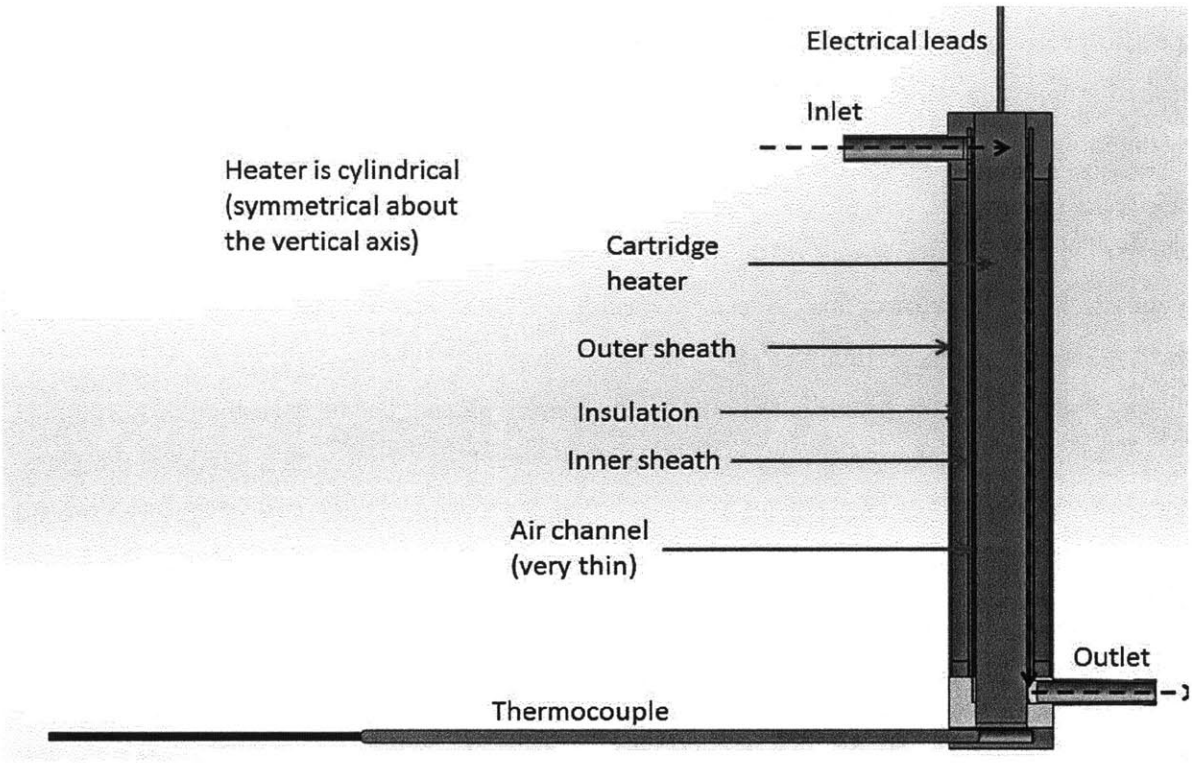

Figure 8.4: Cross-sectional view of custom in-line heater.

A cartridge heater, which can withstand up to 870°C, is at the center of the heater and aligned with the direction of the air flow. A thermocouple is in direct contact with the cartridge heater to ensure that the heater does not overheat. The inner sheath has a diameter that is less than 0.5 mm larger than the diameter of the cartridge heater. This small air passageway ensures that there is not much of a thermal gradient across the passageway. The inner sheath is covered with insulation to mitigate heat loss, and then finally an outer sheath covers the insulation.

To quickly calculate the required dimensions of the cartridge heater, the heat transfer equation can be used with the equation for heat capacity.

$$Q = h * A * \Delta T \tag{8.1}$$

$$U = c_p * \rho * V * \Delta T_2 \tag{8.2}$$

In equation (8.1), Q is the rate of heat transfer, h is the convection coefficient, A is the surface area of contact between heater and fluid, and ΔT is the temperature difference between the air and the heater. In equation (8.2), U is the energy required to heat up a given mass, c_p is the

specific heat capacity, ρ is the density of fluid, V is the volume of the fluid, and ΔT_2 is the desired increase in temperature. For a continuous supply of fluid, equation (8.2) can be divided by time to get,

$$Q = c_p * \dot{m} * \Delta T_2 \tag{8.3}$$

where $\dot{m}$ is the mass flow rate of the fluid. Substituting equation (8.3) into equation (8.1), the required surface area of contact A can be calculated, from which a suitable geometry for the cartridge heater can be chosen.

The air from the heater is fed into the air bearing plenum chambers, which is surrounded by a layer of insulation. Since there will always be some heat loss from the heater to the glass, the nitrogen will have to be pre-heated to higher than the required temperature. There is a second thermocouple located in the plenum to approximate the temperature of the nitrogen contacting the glass. An aluminum shell covers the insulation in order to help dissipate the heat that conducts through the insulation. Figure 8.5 shows the thermal schematic.

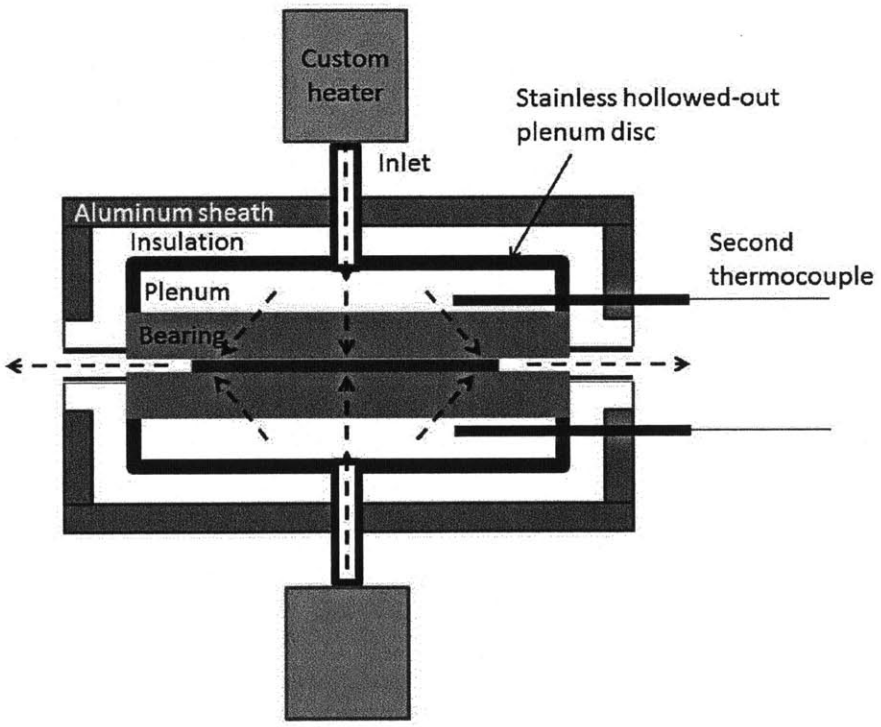

Figure 8.5: Thermal schematic of first strategy (inline heater).

8.4.1 Failure of and solution for in-line heaters

What was failed to be accounted for was that the heat loss during the path from the heater to the bearing was very large relative to the thermal energy contained in the nitrogen. Even if the whole thermal insulation system only allows a loss of 5 W, that is half the thermal energy of the nitrogen.

In addition, another problem was in the controlling of the heater. At 500 sccm, the power required to heat the nitrogen is only about 10 W. However, 10 W is also insufficient to raise the temperature of the heating element to 600°C. Thus since the initial current and voltage fed into the heating element greatly exceeds 10 W, the temperature will overshoot the set point by a large amount and oscillate.

Due to these factors, the custom inline heater was unable to perform to expectations. With the best continuous performance attained from the heater, the plenum temperature was about 200°C when the nitrogen at the heater outlet was set to 500°C. Raising the set point to 600°C resulted in burnout of the heating element.

A commercially available inline heater from Tutco-Farnam, the 075 Heat Torch, had a better result. When the nitrogen at the heater outlet was set to 500°C, the plenum temperature was able to reach about 300°C. However, raising the set point to 600°C resulted in burnout of the heating element again.

One solution would be to significantly increase the nitrogen flow, and then bleed off the excess flow into the ambient air. This would solve the overheating problem and also would raise the plenum temperature much more quickly. The main disadvantage would be the need for additional electronics in flow control. Since much of the nitrogen would have to be bled off, the only way to know the air flow through the bearing is to add an extra flow sensor to monitor the bleed flow. This solution will be further investigated in the future.

8.5 Thermal Design: Embedded Plenum Heaters

The second strategy was to place the heating element inside the plenum. Figure 8.6 illustrates this concept.

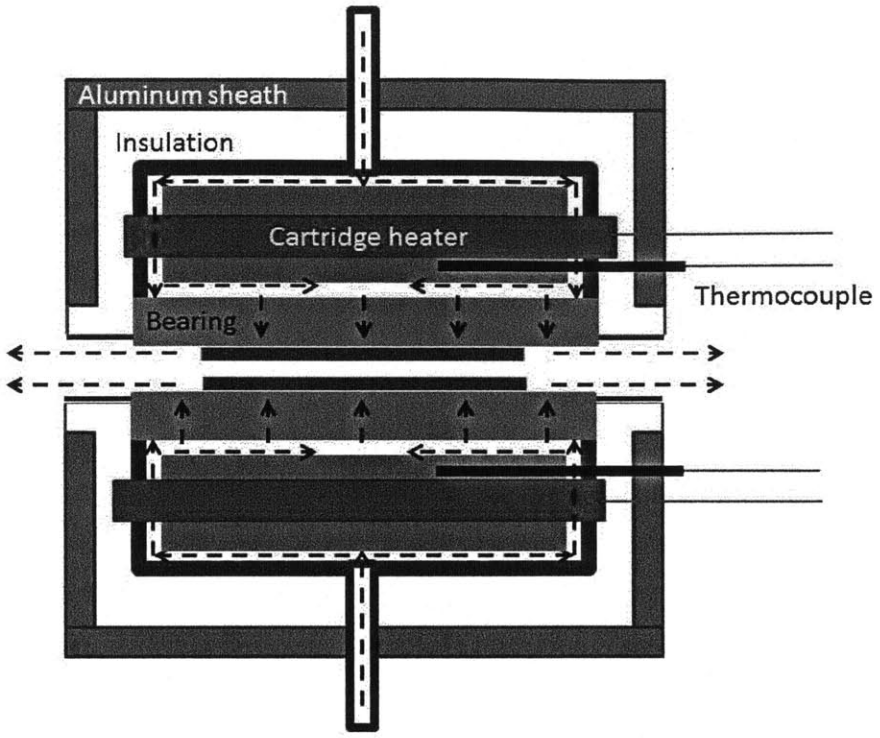

Figure 8.6: Thermal schematic of second strategy (embedded heater in plenum).

The cartridge heater is press fit into a steel disc that stays suspended inside the plenum chamber. A thermocouple measures the temperature of the disc.

This strategy has the advantages of minimizing heat loss, making use of radiation, and providing a heat sink (the steel disc) for the cartridge heater. For testing purposes, a half-scale miniaturized version of a single plenum/bearing/insulation assembly was built. An infrared sensor was used to measure the temperature of the bearing while a second thermocouple measured the air outside of the bearing.

At a set point of 730°C for the cartridge heater, the bearing temperature reached 600°C while the nitrogen flowing through the bearing reached only 450°C. The heating process took about 30 minutes, but since only one assembly was used, it is inferred that, with two assemblies, the heating process should not take more than half the time (15 minutes).

Although the nitrogen temperature did not reach the desired temperature with the half-scale model, this had been expected because the diameter of the heater disc with the embedded cartridge heater only had a diameter of 75 mm. This means that the length of the path of the

nitrogen through the plenum is on average only about 50 mm. Using equations (8.1) and (8.3), the required path length (neglecting heat losses) is calculated to be about 100 mm. A full-scale version of the assembly would have a longer path length, allowing the nitrogen to reach higher temperatures.

In addition, the fact that the bearing itself reached the required temperature (>550°C) already implies a success. The bearing was able to reach that high of a temperature due to radiation from the heater disc. Since the bearing-to-disc distance is 1.5 mm, and since, under slumping conditions, the bearing-to-glass gap is less than 50 μm, the glass will be able to become as hot as the bearing due to radiation. The emissivity coefficients of both silicon carbide and glass are around 0.9.

CHAPTER

9

CONCLUSIONS & FUTURE WORK

9.1 Conclusions

It has been shown that glass can be slumped horizontally, without contact, and using air bearings, to micron-level precision. The lowest peak to valley achieved in the scope of this thesis was 3.8±0.5 μm. However, this was with a relatively large gap of 36±2.5 μm between bearing and glass. With a smaller gap, the stiffness of the air layer rises exponentially, and may result in a much lower P-V for the slumped glass.

Additionally, the slumped glass only exhibited low frequency spatial errors, since dust particles are not an issue as they are with traditional methods and the bearing errors are averaged out by constantly moving the glass within the bearings. The low frequency spatial errors can be removed or corrected via ion implantation, which is a technique that has been researched by Brandon Chalifoux of the MIT Space Nanotechnology Lab group.

It has been shown that 600°C is not necessary to slump glass using the air bearing method and may in fact be too high of a temperature to produce good results with repeatability. 550°C was shown to be hot enough to successfully slump glass, although results indicate that an even lower temperature may be used.

A full-scale version of either one of the two heating strategies discussed in chapter 8 has yet to be installed in device 2.3. Once a full-scale version is installed, device 2.3 will mark a large step as it is the first device to use thermal isolation of the bearings instead of being operated within a large oven. A large disadvantage with using an oven is that, since the entire device will reach slumping temperature, the design and build of the device is made unnecessarily difficult.

Additionally, large ovens require long ramp-up and ramp-down times, needlessly increasing the thermal cycle time. Preliminary testing shows that the slumping cycle time can be reduced to about 30 minutes (15 minutes heating, 5 minutes slumping, 10 minutes cooling), as opposed to several days for traditional methods [5].

Non-contact slumping technology offers drastically reduced processing and manufacturing times for optics. The elimination of the oven also cuts costs by a great deal, as each oven must undergo its own preparation such as painting all the insulation surfaces with a high temperature paint to reduce dust. Although the actual shift from flat to curved glass shapes still has to be implemented, non-contact slumping has the potential to quickly produce cylindrical and hyperbolic x-ray optics.

9.2 Future work

A full-scale version of the bearing/plenum/insulation assembly as described in section 8.5 must be built and tested. In addition, optimal slumping parameters still need to be determined. Specifically, the optimal gap and temperature must be determined through trial and error and modeling. 550°C can be used as the upper bound when attempting to determine the lowest possible temperature.

Before the shift to cylindrical and hyperbolic shapes can be made, one last technology still remains to be developed. Somehow, the bearing-to-glass gap must be sensed, allowing for automatic pressure adjustment to float the glass. While this gap sensing was not required for the flat optics, it will be much more crucial for the curved optics. Because the optics are curved, the top and bottom bearings will have different flow resistances, meaning that equalizing the plenum pressures will not result in the glass floating. Both plenum pressures will have to be actuated separately with feedback from the bearing-to-glass gap. It is easier to develop this sensing technology using existing devices, rather than concurrently with trying to achieve cylindrical shapes.

A second technology to be developed before moving on, though optional, is to transition from the shims to bearing-to-bearing gap actuation, as was designed in device 2.1. Bearing-to-bearing gap actuation was difficult previously because the capacitance sensors kept failing after

multiple thermal cycles and expansions of materials made gap control difficult. However, post device 2.3, none of these problems exist since the device operates in ambient air.

One reason that bearing-to-bearing gap actuation may be desirable is that precise and accurate shims are difficult to procure. Another reason is that shear force may be used in combination with gravity to do more complicated controls. For example, gravity might be used to control the overall position of the glass while shear force is used to rotate the same glass.

After these two technologies are developed, the shift to cylindrical shapes is projected to take place in 2015. Some of the challenges that were present in slumping flat glass will not exist for curved shapes. For example, control of a curved glass will be much easier due to the stability that occurs when the glass is placed convex downwards. The glass will only have to be controlled in the axial direction. High accuracy air bearings may be easier to produce, since cylindrical bearings can be cut on a flywheel, instead of a flat grinding process.

On the other hand, there will be new challenges due to the same curved shape, most notably getting a flat sheet of glass to a curved shape that can fit in between two cylindrical bearings in the first place.

One idea is to go from 0.5 mm thick glass sheets to 0.1 mm thick sheets, which can bend a large amount without shattering. Then the glass can simply be forced in between the two air bearings while the temperature is increased to the slumping temperature, at which the glass will adopt the proper shape and start floating. This is probably the ideal solution, as thin glass is desired at any rate due to low weight, which is advantageous for installment in a telescope.

REFERENCES

[1] M. Akilian, "Methods of Improving the Surface Flatness of Thin Glass Sheets and Silicon Wafers," Phd Thesis, Massachusetts Institute of Technology, Sep. 2008

[2] A. Husseini, "Design and Modeling of a Third Generation Slumping Tool for X-ray Telescopes Mirrors," MS Thesis, Massachusetts Institute of Technology, Jun. 2011

[3] Goddard Space Flight Center, "Electroformed Nickel Replication Mirror," accessed Mar. 2013, <http://constellation.gsfc.nasa.gov/technology/hxiNIckelOptics.html>

[4] W. Zhang, "Next generation x-ray optics: high-resolution, light-weight, and low-cost," Proc. SPIE 8443, (2012).

[5] W. Zhang, et al., "Lightweight and high angular resolution x-ray optics for astronomical missions," Proc. SPIE 8147, (2011)

[6] R. Heilmann, G. Monnelly, O. Mongrard, et.al, "Novel methods for shaping thin-foil optics for x-ray astronomy," Proc. of SPIE, X-Ray Optics for Astronomy, 4496:0277-786X/02,2002.

[7] Robert Petre et al. Recent progress on the constellation-x spectroscopy x-ray telescope (sxt). Proc. of SPIE, Optics for EUV, X-Ray, and Gamma-Ray Astronomy, 5168:196–206, 2004.

[8] Morgan Technical Ceramics, "Incusil ABA Data Sheet," accessed Feb. 2013, <http://www.morgantechnicalceramics.com/download.php?35336c684c7630545968377a494c56566c55485447482f35467541716e48536b2f38786b34765543534a566237513d3d>

[9] G. Qiao, C. Zhang, Z. Jin, "Thermal cyclic test of alumina/kovar joint brazed by Ni-Ti active filler," Ceramics International Vol. 29 Issue 1, pp. 7-11.

[10] Ed Fagan Inc., "Kovar Alloy Properties," accessed Feb. 2013, <http://www.kovaralloy.com/kovar-properties.php>

[11] Carpenter Tech. Corp., "Kovar Data Sheet," accessed Feb. 2013, <http://cartech.ides.com/datasheet.aspx?i=101&E=173&FMT=PRINT>

APPENDIX

A

MATLAB CODE

A.1 Flow in Porous Media with Flat Surfaces [2]

```
%Mireille Akilian
%Pressure distribution of air bearing for slumping with no grooves
%Last updated Tue 9 Feb 07
clc;
clear;
% number of nodes N x N x N
N=13;
%all dimensions in mm, but not a problem since this is a dimensionless
%solution, just make sure that the permeability is in the proper units of
%mm2 rather than the regular m2 (Darcy)
% permeability ratio Kx = kx/kz and Ky = ky/kz
Kx=1;
Ky=1;
kz=6*10−9; %kx=ky=kz=10−14m2 at room temperature. note these are absolute
permeabilities and not ratios. But this 6x10−9 is the value at 600C
% ceramic dimensions
255
X=100; %100mm
Y=100; %100mm
H=12.7; %12.7mm
% ceramic width to length ratio XY
XY=X/Y;
XH=X/H;
% air gap thickness h
h=50/1000; %50 um
% constant A used in first equation
```

```
A=2*(Kx+Ky*XY2+XH2);
% supply pressure to atm pressure ratio psa
psa=(14.5+0.3)/14.5; %this parameter is a ratio of absolute pressure used to
absolute atm pressure;
pa=14.5; %absolute atm pressure
% feeding parameter lmda=12kzX^2/(h^3H)
lmda=12*kz*X2/h3/H;
% coefficients used in second equation
a=1./lmda+1/2*Kx*H*h/X2;
b=1./lmda+1/2*Ky*H*h/X2;
del=1/(N-3); % normalized del so that delx = dely = delz normalized, otherwise
they are not equal
% pressure matrix NxNxN elements
P=zeros(N,N,N);
% BOUNDARY CONDITIONS
% bottom ceramic surface at plenum supply pressure
(:,:,1:2)=psa;
% ambient condition on ceramic top surface edges where p=patm
P(1:2,:,N-1:N)=1;
P(:,1:2,N-1:N)=1;
P(:,N-1:N,N-1:N)=1;
256
P(N-1:N,:,N-1:N)=1;
% FINITE DIFFERENCE ITERATION METHOD
for f=1:1:3000
for i=3:1:N-2
for j=3:1:N-2
for k=3:1:N-2
P(2,j,k)=(Kx*P(3,j,k)+Ky*XY2*(P(2,j+1,k)+P(2,j-1,k))+XH2*(P(2,j,k+1)+P(2,j,k-
1)))/(Kx+2*(Ky*XY2+XH2)); %these four lines are for the nodes on the sides of the
bearing along the y axis
P(1,j,k)=P(2,j,k);
P(N-1,j,k)=(Kx*P(N-2,j,k)+Ky*XY2*(P(N-1,j+1,k)+P(N-1,j-1,k))+XH2*(P(N-1,j,k+1)+P(i,j,k-
1)))/(Kx+2*(Ky*XY2+XH2));
P(N,j,k)=P(N-1,j,k);
P(i,2,k)=(Kx*(P(i+1,2,k)+P(i-1,2,k))+Ky*XY2*P(i,3,k)+XH2*(P(i,2,k+1)+P(i,2,k-
1)))/(2*(Kx+XH2)+Ky*XY2); %these four lines are for the nodes on the sides of the
bearing along the x axis
P(i,1,k)=P(i,2,k);
P(i,N-1,k)=(Kx*(P(i+1,N-1,k)+P(i-1,N-1,k))+Ky*XY2*P(i,N-2,k)+XH2*(P(i,N-
```

```
1,k+1)+P(i,N-1,k-1)))/(2*(Kx+XH2)+Ky*XY2);
P(i,N,k)=P(i,N-1,k);
P(i,j,k)=(Kx*(P(i+1,j,k)+P(i-1,j,k))+Ky*XY2*(P(i,j+1,k)+P(i,j-1,k))+XH2*(P(i,j,k+1)+P(i,j,k-
1)))/A;
%corners
P(2,2,k)=(Kx*P(3,2,k)+Ky*XY2*(P(2,3,k)+P(2,1,k))+XH2*(P(2,2,k+1)+P(2,2,k-
1)))/(Kx+2*(Ky*XY2+XH2));
P(1,2,k)=P(2,2,k);
P(2,1,k)=P(2,2,k);
P(1,1,k)=P(2,2,k);
P(2,N-1,k)=(Kx*P(3,N-1,k)+Ky*XY2*(P(2,N,k)+P(2,N-2,k))+XH2*(P(2,N-1,k+1)+P(2,N-
1,k-1)))/(Kx+2*(Ky*XY2+XH2));
257
P(1,N-1,k)=P(2,N-1,k);
P(2,N,k)=P(2,N-1,k);
P(1,N,k)=P(2,N-1,k);
P(N-1,2,k)=(Kx*P(N,2,k)+Ky*XY2*(P(N-1,3,k)+P(N-1,1,k))+XH2*(P(N-1,2,k+1)+P(N-
1,2,k-1)))/(Kx+2*(Ky*XY2+XH2));
P(N,2,k)=P(N-1,2,k);
P(N-1,1,k)=P(N-1,2,k);
P(N,1,k)=P(N-1,2,k);
P(N-1,N-1,k)=(Kx*P(N,N-1,k)+Ky*XY2*(P(N-1,N,k)+P(N-1,N-2,k))+XH2*(P(N-
1,N-1,k+1)+P(N-1,N-1,k-1)))/(Kx+2*(Ky*XY2+XH2));
P(N,N-1,k)=P(N-1,N-1,k);
P(N-1,N,k)=P(N-1,N-1,k);
P(N,N,k)=P(N-1,N-1,k);
end
P(i,j,N-1)=(a*(P(i+1,j,N-1)+P(i-1,j,N-1))+b*XY2*(P(i,j+1,N-1)+P(i,j-1,N-1))+del/2*P(i,j,N-
2))/(2*a+2*b*XY2+del/2); %note that in this equation there is no N for k only N-1
because we are assuming there is no pressure drop along the z axis in the air gap.
This is the Modified Reynold's equation boundary condition
P(i,j,N)=P(i,j,N-1);
end
end
end
for m=1:1:N-2
for s=1:1:N-2
S(m,s)=P(m+1,s+1,N-1);
Pbearing(m,s)=S(m,s)*pa-pa;
Load(m,s)=Pbearing(m,s)/0.145*103*X/1000/(N-3)*Y/1000/(N-3);
```

```
Q(m,s)=P(m+1,s+1,2);
R(m,s)=P(m+1,s+1,3);
end
258
end
%Plotting issues
figure;
x(1)=-X/2;
y(1)=-Y/2;
for i=2:1:N-2
x(i)=x(i-1)+X/(N-3);
y(i)=y(i-1)+Y/(N-3);
end
surf (x,y,Pbearing)
xlabel('x (mm)')
ylabel('y (mm)')
zlabel('Pressure distribution (psig) at Psupply=0.00347 psig')
%title('Pressure distribution along rectangular bearing area at supply pressure of
5 psig and a gap of 10 um')
%Load Capacity calculation
%W=double integral (p-pa)dxdy x and y from 0 to X,Y, this integral is the sum
of the
%pressures multiplied by the areas with the area limit going to zero or in other
words as small as possible, or in other words increase N so that deltaA is very small
deltaA=X/(N-2-1)*Y/(N-2-1)/1000000;
sum=0;
for i=1:1:N-2
for j=1:1:N-2
inc=(Pbearing(i,j)/0.145*1000)*deltaA;
sum=sum+inc;
end
end
W=sum;
259
fprintf('The load capacity of this bearing for a supply pressure of %g psig is %g N',psa*pa-
pa,W)
```

APPENDIX

B

LABVIEW PROGRAMS

B.1 1D shear testing device controller

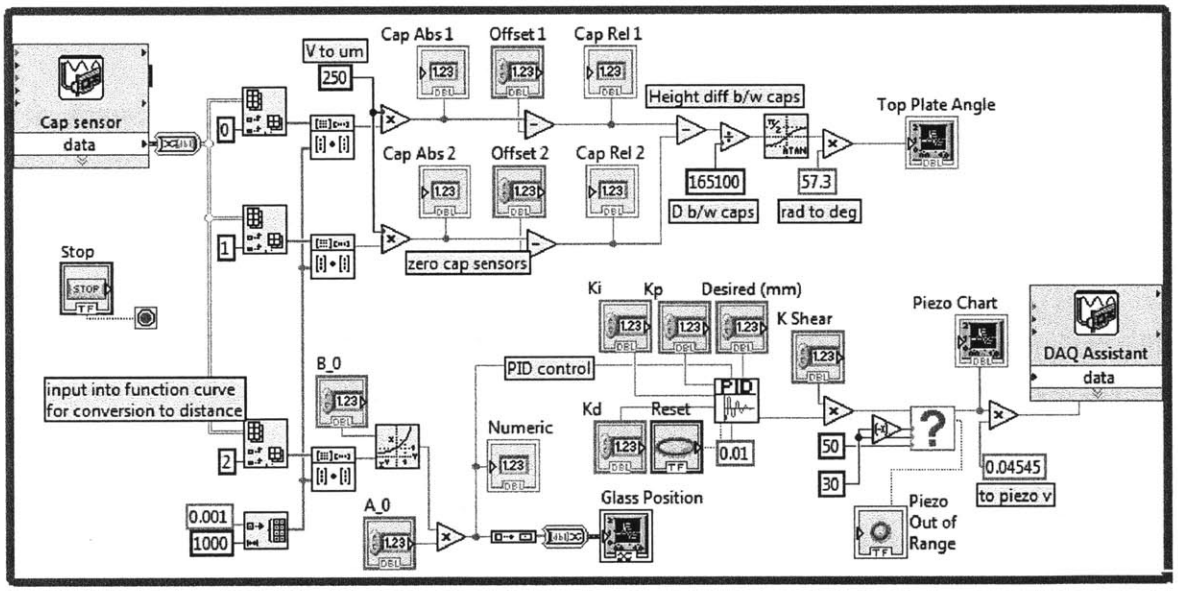

Figure B.1: Labview controller for 1D shear testing device

B.1.1 PID subvi

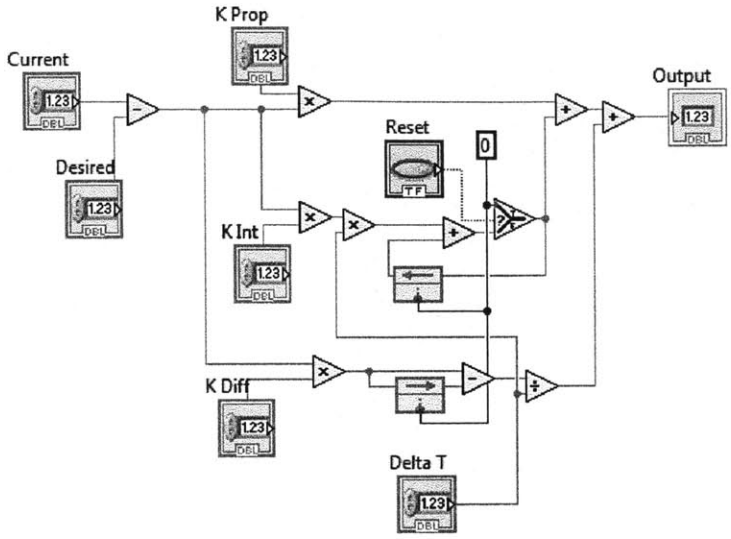

Figure B.2: PID subvi

B.2 2D shear testing device controller

(next page)

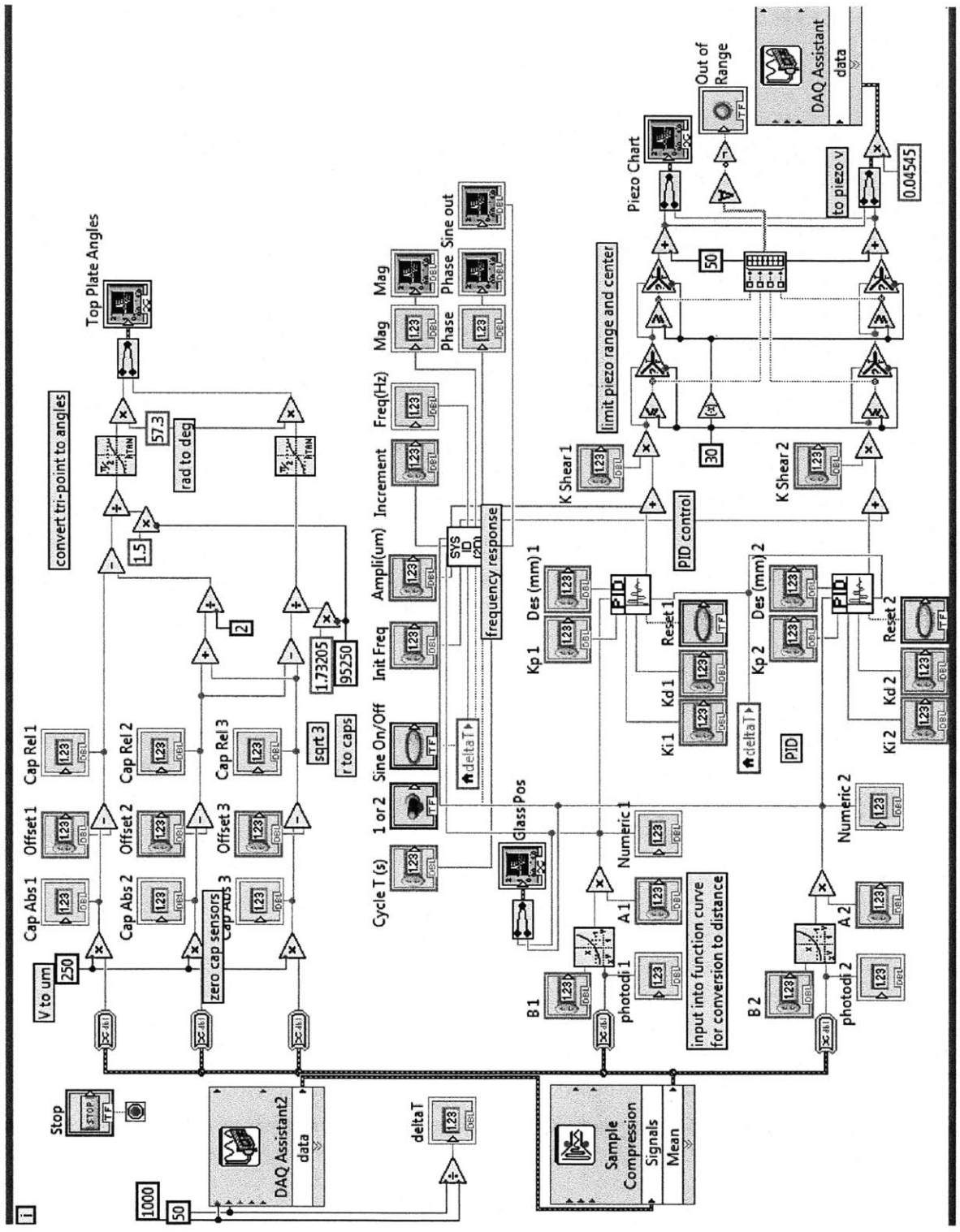

Figure B.3: Labview controller for 2D shear testing device

B.2.1 SYSID subvi

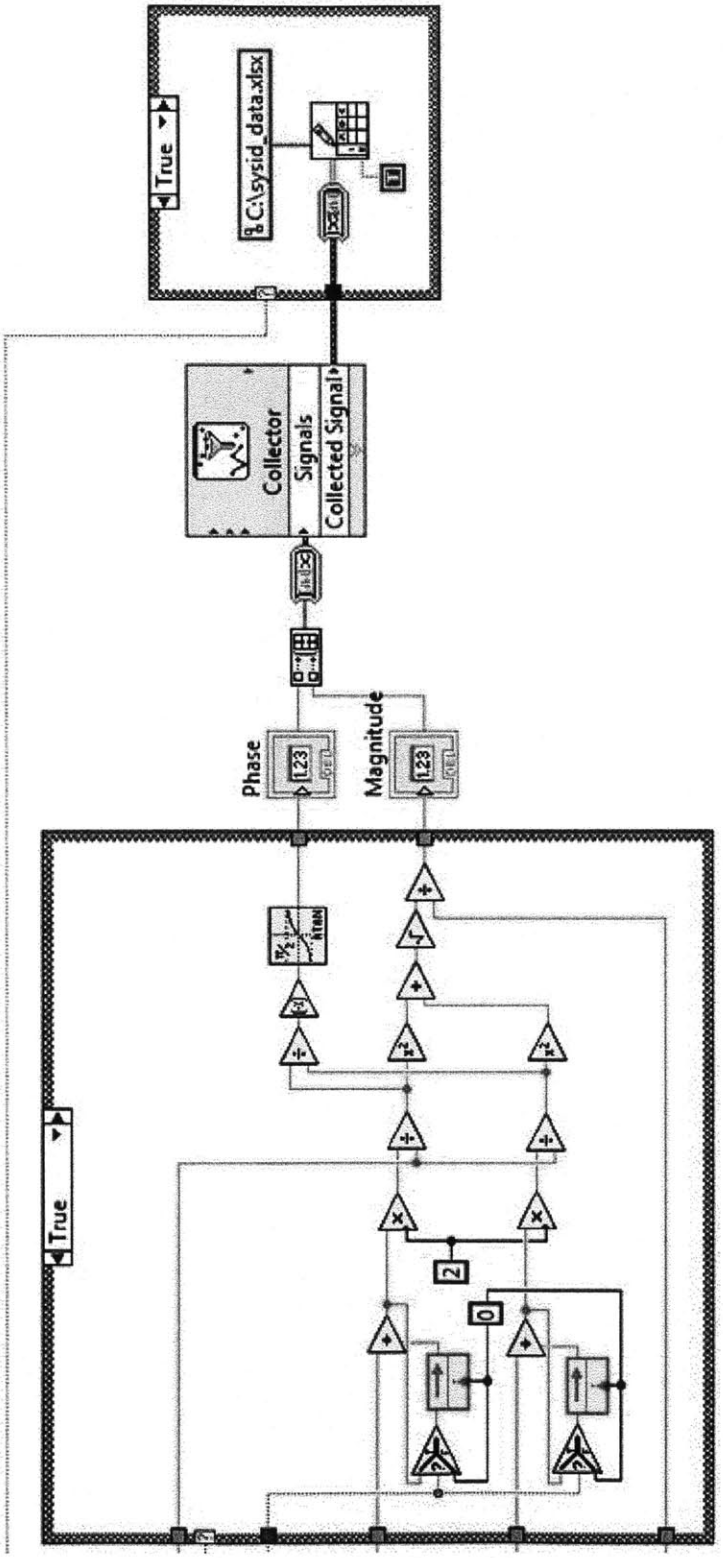

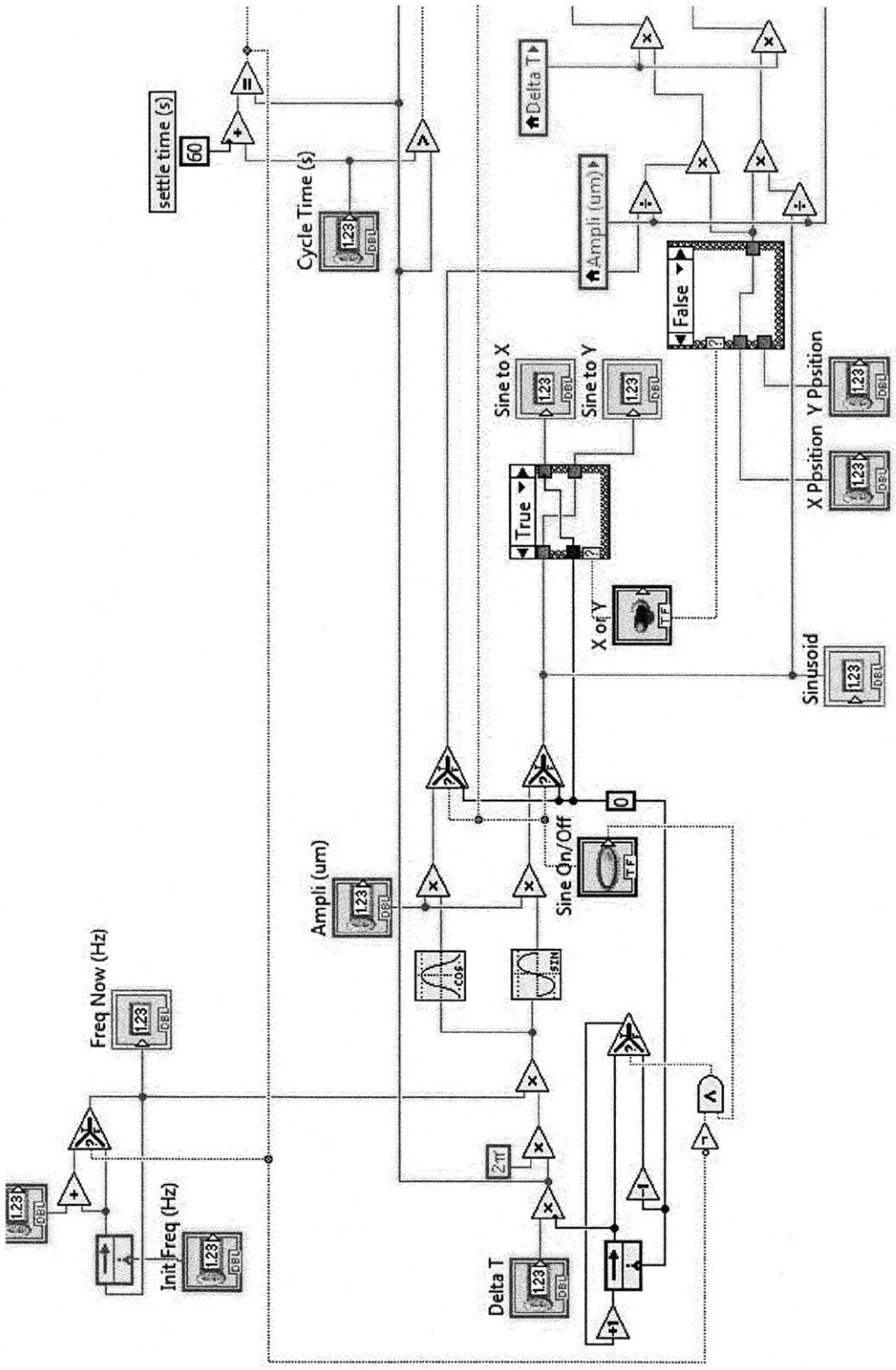

Figure B.4: SYSID subvi

B.3 Device 2.2 controller

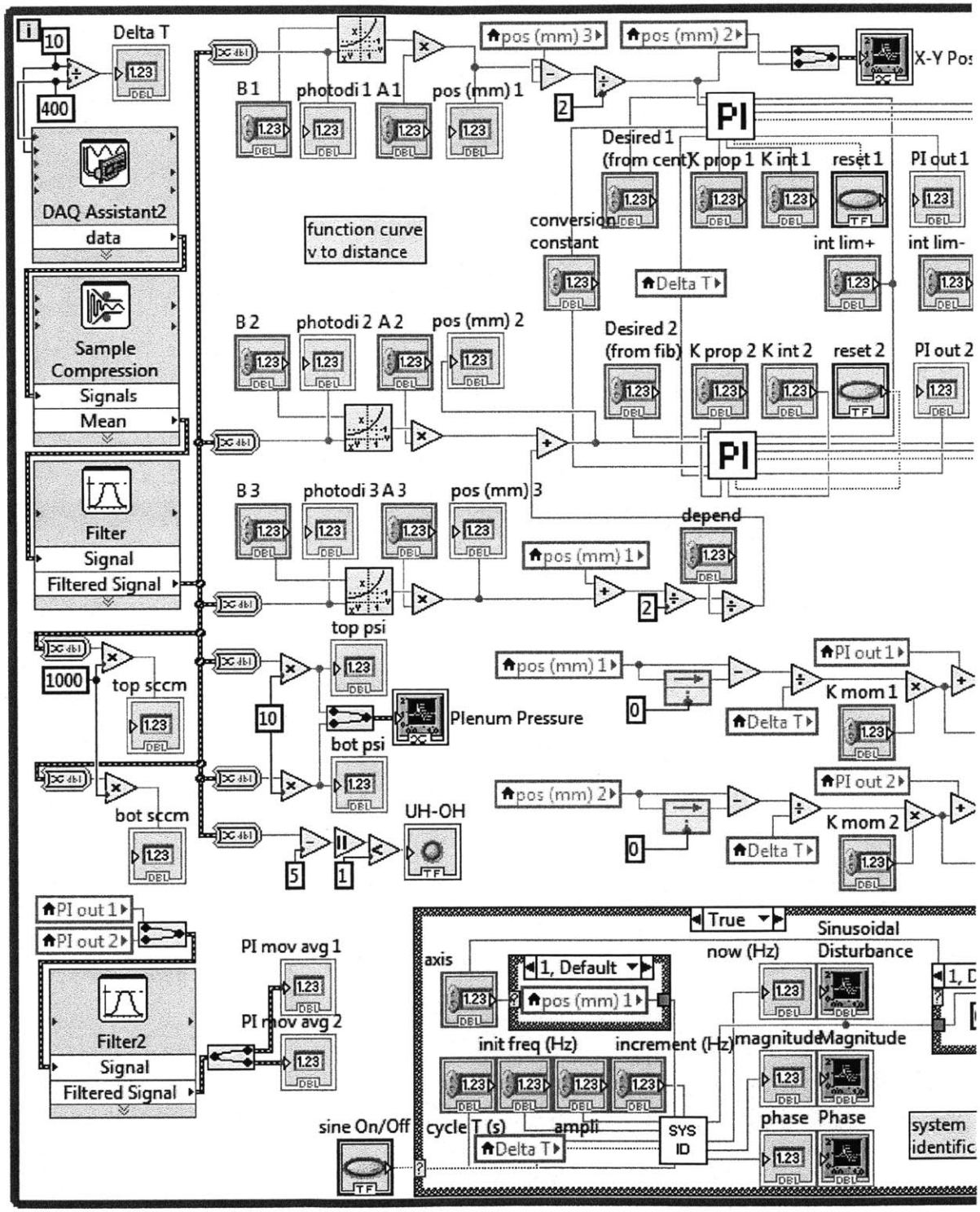

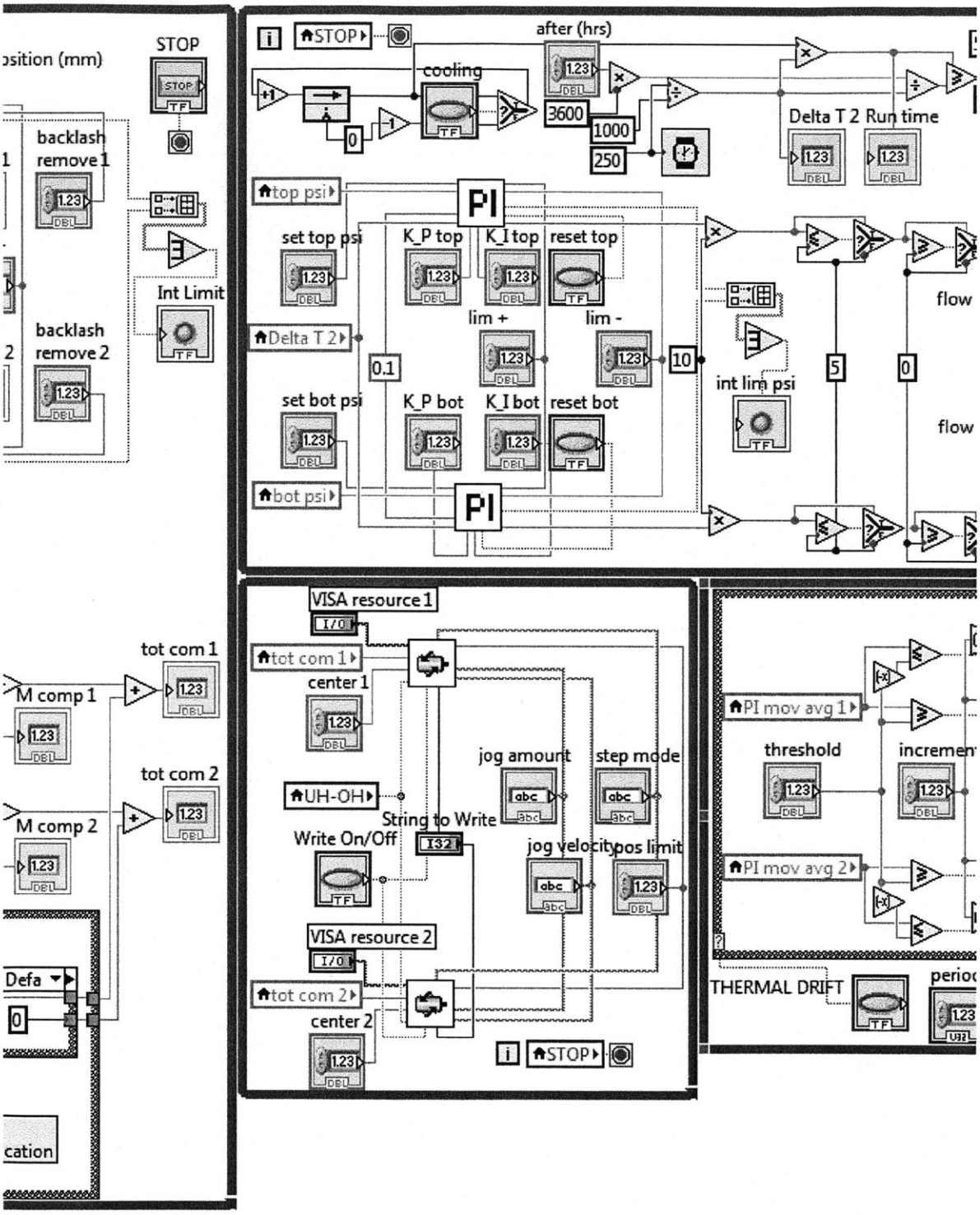
STOP
backlash remove 1
Int Limit
backlash remove 2
tot com 1
M comp 1
tot com 2
M comp 2
Defa
cation
after (hrs)
cooling
3600
1000
250
Delta T 2 Run time
top psi
PI
set top psi
K_P top
K_I top
reset top
lim +
lim -
Delta T 2
0.1
10
int lim psi
5
0
flow
set bot psi
K_P bot
K_I bot
reset bot
bot psi
PI
flow
VISA resource 1
I/O
tot com 1
center 1
jog amount
step mode
UH-OH
String to Write
I32
Write On/Off
jog velocity
pos limit
VISA resource 2
tot com 2
center 2
STOP
PI mov avg 1
threshold
PI mov avg 2
THERMAL DRIFT

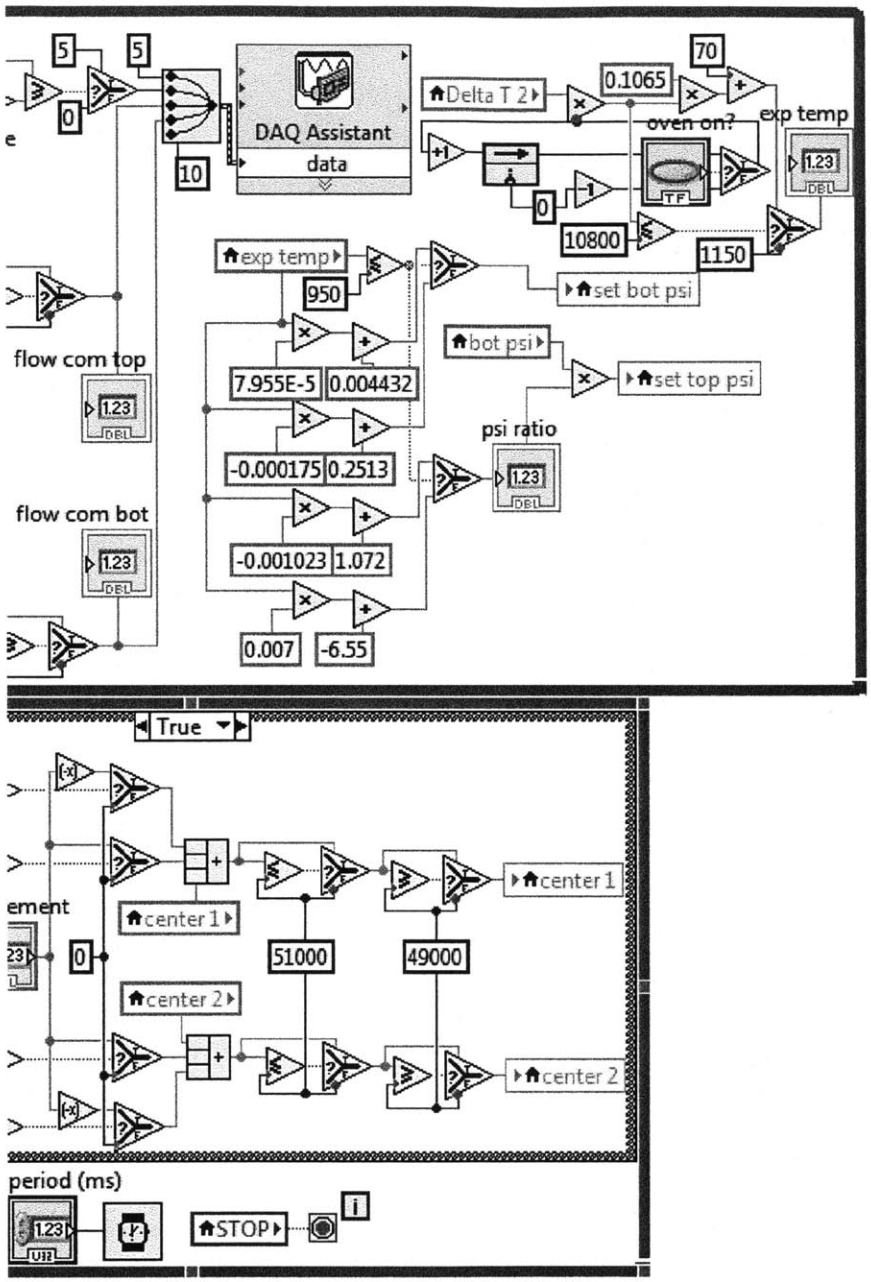

Figure B.5: Labview controller for device 2.2

B.3.1 PI subvi with anti-windup and anti-backlash

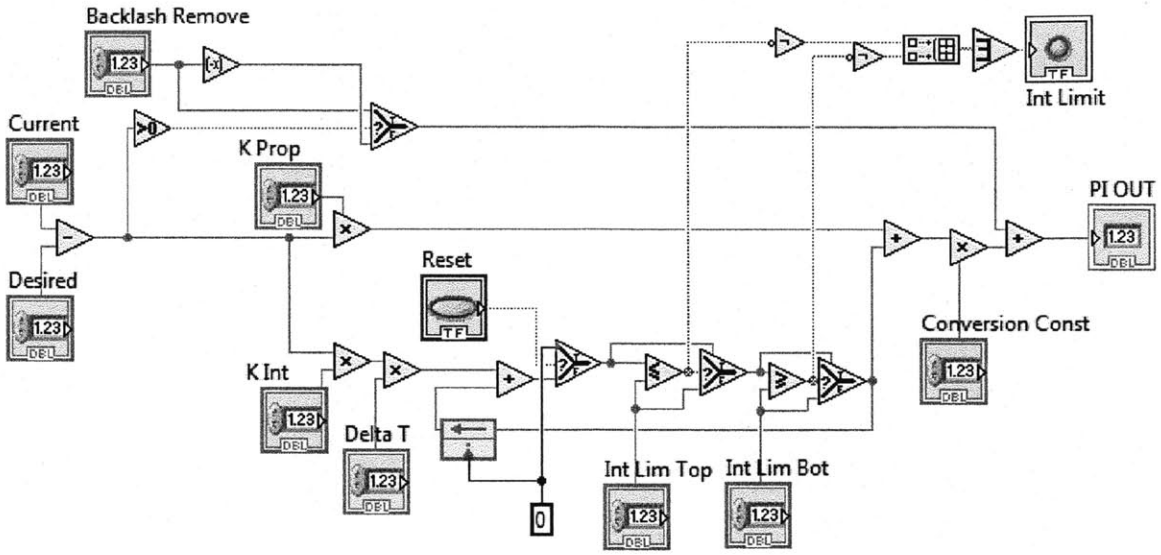

Figure B.6: PI subvi with anti-windup and anti-backlash

B.3.2 Serial command out to stepper motors subvi

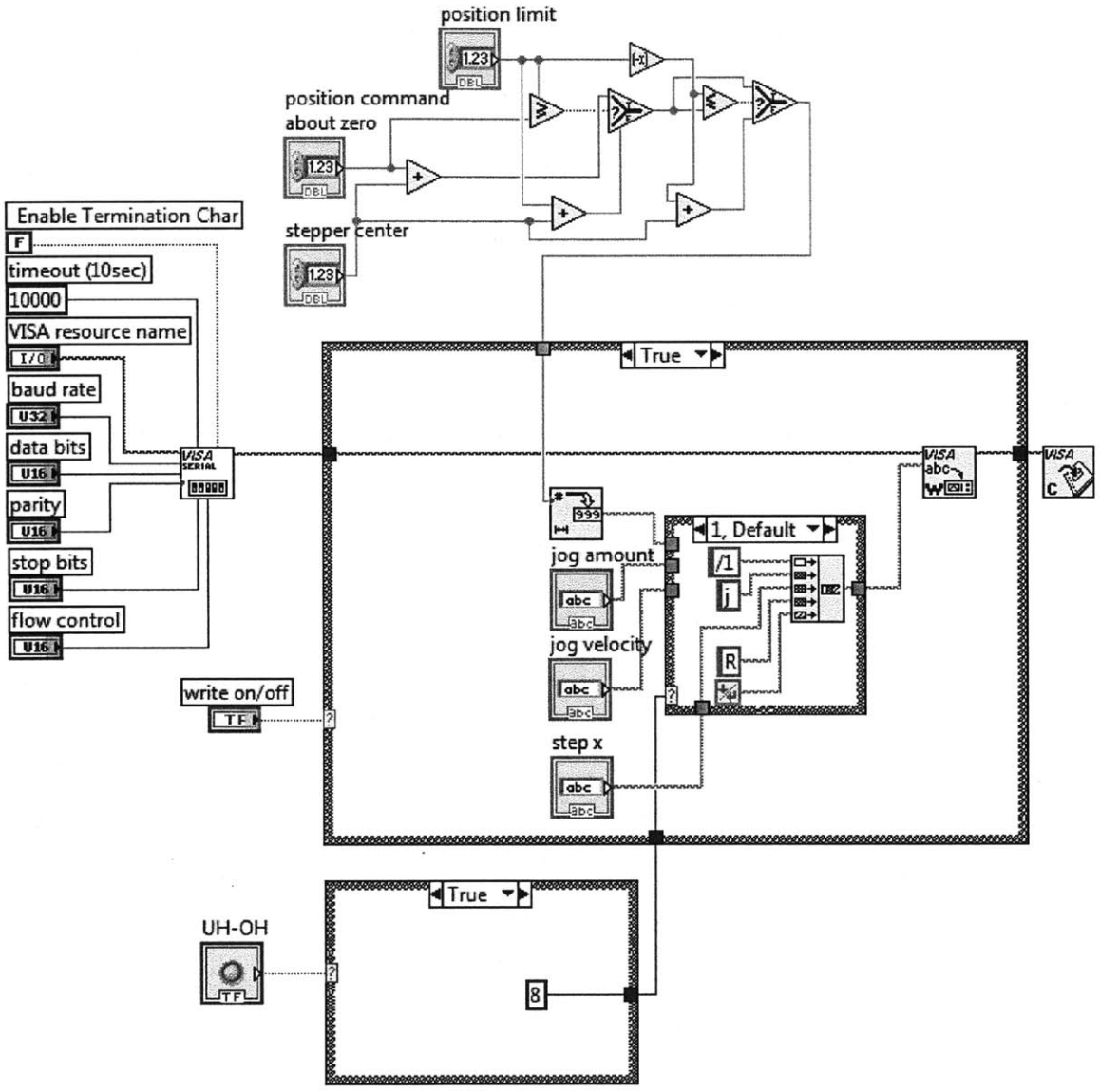

Figure B.7: Serial command out to stepper motors subvi